Cal Poly

Caltech

SCEC
AN NSF+USGS CENTER

UC Irvine

UCLA

UC Santa Barbara

USC

Reverse Fault PFDHA

Robb Moss, Ph.D. P.E. F.ASCE
California Polytechnic State University

Stephen Thompson, Ph.D.
Lettis Consultants International

Chun-Hsiang Kuo, Ph.D.
National Central University
National Center for Research on Earthquake Engineering

Kourosh Younesi
Science and Research Branch of Azad University

David Baumont
Seister SAS, CEO and co-Founder

Report GIRS-2022-05

DOI: 10.34948/N3F595

University of California, Los Angeles (headquarters)

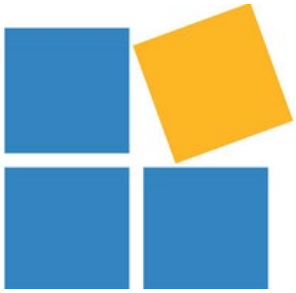

Natural Hazards Risk & Resiliency Research Center

B. John Garrick Institute for the Risk Sciences

Reverse Fault PFDHA

Robb Moss, Ph.D. P.E. F.ASCE
California Polytechnic State University

Stephen Thompson, Ph.D.
Lettis Consultants International

Chun-Hsiang Kuo, Ph.D.
National Central University
National Center for Research on Earthquake Engineering

Kourosh Younesi
Science and Research Branch of Azad University

David Baumont
Seister SAS, CEO and co-Founder

Report GIRS-2022-05
DOI: 10.34948/N3F595

Natural Hazards Risk and Resiliency Research Center
B. John Garrick Institute for the Risk Sciences
University of California, Los Angeles (Headquarters)

May 2022

ABSTRACT

This report covers research on a probabilistic fault displacement hazard analysis (PFDHA) model for reverse faulting events. The goal was to provide the tools needed to estimate surface fault rupture displacements for reverse faults within a hazard forecasting framework. This model supersedes previous models and includes: revised relationships between magnitude and maximum/average displacement, revised distributions of principal displacement along fault strike, improved distributions of principal displacement exceedance. the addition of distributed displacement models, and improved coding of the PFDHA methodology for hazard calculation. This work has been in conjunction with the UCLA-led Fault Displacement Hazard Initiative (FDHI), and specifically the FDHI database (Sarmiento et al., 2021) and the FDHI working group monthly discussions. Additional insights have been gained through participation in the PFDHA benchmarking project led by the International Atomic Energy Agency (IAEA). Contained in this report are the statistical/analytical analyses and resulting mathematical functions that comprise the PFDHA calculation. The code developed for performing these calculations are included in the appendix. The results are a comprehensive set of options that allow users to forecast reverse fault displacements for both on-fault and off-fault locations.

REVISIONS

This report has been revised since its initial publication date. The revisions address changes and corrections in the distributed displacement model and its coding. The changes and corrections came about through the validation process initiated by the IAEA for vetting PFDHA codes. The changes include:

- Completely revised section on probability of nonzero distributed displacement, P(d>0), shown in pgs. 50-62.
- Error correction in the coefficients reported for the frequency distributions of distributed displacements in shown in pgs. 63-75.
- Revised d/MD and d/AD plots and the inclusion of tabulated percentiles shown in pgs. 76-85.
- Revised hazard curves for distributed displacement to reflect the changes in the model shown in pgs. 88.
- Revised coding to reflect these changes and corrections, Appendix C.

ACKNOWLEDGMENTS

There was no external funding for this research. The home institutions of each of the co-authors are gratefully acknowledged for their tacit support. These institutions provided the time and space to work on this research.

The opinions, findings, conclusions, or recommendations expressed in this publication are those of the authors and do not necessarily reflect the views of the study sponsors, the B. John Garrick Institute for the Risk Sciences, or the Regents of the University of California.

CONTENTS

LIST OF FIGURES

LIST OF TABLES

1 Introduction

This report covers research endeavors on updating a probabilistic fault displacement hazard analysis (PFDHA) model for reverse faulting events. The original model by Moss and Ross (2011) is superseded by the work presented herein. Updates on all components of the model are provided with justification for the revisions. Included in this updated PFDHA model are:

- Revised relationships between magnitude and maximum/average displacement.
- Revised distributions of principal displacement along fault strike.
- Improved distributions of principal displacement exceedance.
- The addition of distributed displacement modeling.
- Improved coding of the PFDHA methodology for hazard calculation.

The research team consists of individuals from diverse backgrounds with an interest in improving reverse fault displacement hazard calculations. A shared goal was to provide as useful a model as possible for engineering applications that wish to quantify fault displacement hazard where structures and facilities are located near or across reverse faults and avoiding these displacements may not be feasible. This work has been aided significantly by the UCLA-led Fault Displacement Hazard Initiative (FDHI), and specifically the FDHI database (Sarmiento et al., 2021) and the FDHI working group monthly discussions. Additional insights have been gained through participation in the PFDHA benchmarking project led by the International Atomic Energy Agency (IAEA) (Valentini et al., 2021).

The geometric relationships for the reverse faulting PFDHA model are shown in Figure 1.1. Reverse events result in contraction (shortening) and thickening of the crust, with the hanging wall (HW) block uplifted with respect to the footwall (FW) block. Surface rupture of the primary fault results in ground offset with a vertical principal surface-fault displacement (D). A particular point along the surface rupture is described by the ratio of its distance from the closest end point of the rupture (x) to the total surface rupture length (L). Surface-fault ruptures that occur on secondary faults or shears may be observed at distances (r) measured perpendicular to the principal rupture. These ruptures produce distributed vertical surface displacements (d). The use of vertical displacements as the intensity measure in our model (as opposed to, for example, 3-D

net displacement) is based on the types of measurements available in the empirical database and is discussed later in the report.

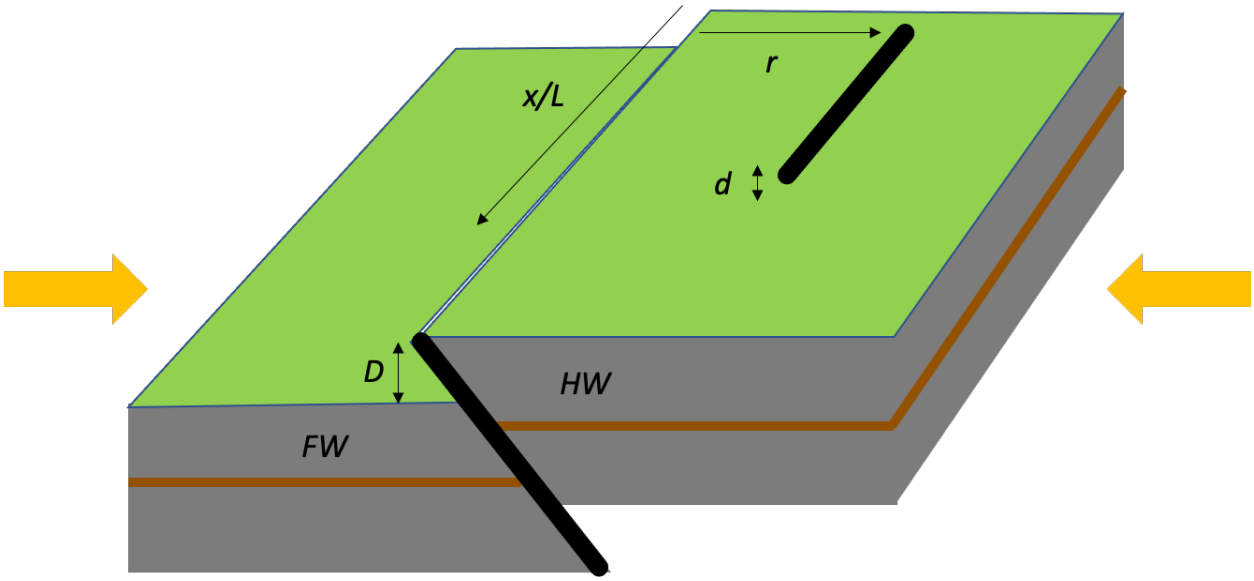

Figure 1.1. Geometry and symbols used in this study to describe surface-fault rupture of reverse earthquakes.

2 Probabilistic Framework

The hazard curve for principal surface-fault displacement can be calculated in the following manner (Youngs et al., 2003; Moss and Ross, 2011):

$$\upsilon(D_0) = \alpha \int_{m_{min}}^{m_{max}} f(m)\, P^*\left(D > D_0 \middle| m, \frac{x}{L}\right)\, dm \tag{2.1}$$

where $\upsilon(D_0)$ is the mean annual rate of exceeding a specified principal surface displacement, α is the mean annual rate of earthquakes of minimum magnitude m_{min} and greater from a specific source, and $f(m)$ is the probability distribution of earthquake magnitude on the source that ranges from m_{min} to a maximum magnitude m_{max}. The term $P^*(D > D_0|m, x/L)$defines the probability that a principal displacement D exceeds a specified level D_0. As the term suggests, this probability is magnitude- and location-dependent. Commonly, this relationship is developed for a specified style of faulting (i.e., normal, reverse, strike-slip) (Youngs et al., 2003; Petersen et al., 2011; Moss and Ross, 2011), or for a specific tectonic region of mixed styles of faulting (e.g., Takao et al., 2013; 2018).

The conditional probability of displacement term is a product of two terms:

$$P^*(D > D_0|m, x/L) = P(SurfRup|m, Slip)\, P\left(D > D_0 \middle| m, \frac{x}{L}, SurfRup\right) \tag{2.2}$$

The first term, $P(SlipSurfRup|m)$, defines the probability that an earthquake of magnitude m will produce surface-fault rupture. The second term, $P(D > D_o|m, x/L, SurfRup))$, is the displacement exceedance term, with the exceedance conditioned on an earthquake of magnitude m that ruptures the surface and evaluated at a normalized location x/L along the principal surface rupture. Solving equation (2.1) with the displacement exceedance term in equation (2.2) expressed as a complementary cumulative distribution function produces an annualized hazard curve that is the primary result of a PFDHA for principal faulting. Note that the equations for principal faulting implicitly assume that the evaluation site crosses the location of future principal fault rupture. In other words, there is no conditional probability that a principal earthquake rupture, given that it ruptures the ground surface, will miss the evaluation site either

as a gap in the surface rupture or as an epistemic uncertainty or aleatory variability in surface rupture location relative to the mapped location of the fault. Petersen et al. (2011) and Takao et al. (2013, 2014) provide examples of this additional term.

The equation for distributed displacement PFDHA is similar to that of principal displacement but with the perpendicular distance from the principal surface rupture to the evaluation site (r) and HW or FW location as variables instead of x/L, as follows:

$$\upsilon(d_0) = \alpha \int_{m_{min}}^{m_{max}} f(m) f(r|m) P^* \left(d > d_0 \middle| m, r, HW or\ FW, \frac{x}{L} \right)\ dm \tag{2.3}$$

where the distributed displacement probability term can be separated into parts as follows:

$$P^*(d > d_0|m, r, HW/FW) = P(SurfRup|m, Slip) P(Rup\ at\ Site|m, r, HW\ or\ FW, x/L)$$
$$P(d > d_0|m, r, HW\ or\ FW, SurfRup, Rup\ at\ Site) \tag{2.4}$$

For reverse (as well as normal) styles of faulting, the conditional probability of distributed rupture with distance and the distributed displacement exceedance distribution depend on whether the evaluation site is located on the hanging wall or footwall side of the fault.

3 Probability of Surface Rupture

The probability of surface rupture, $P(SurfSlipRup|m)$ is the likelihood that a fault producing an earthquake of magnitude m ruptures the ground surface. For purposes of PFDHA, surface-fault rupture can be interpreted to also include near-surface fold scarp development (e.g., Streig et al., 2007) or other forms of localized ground surface deformation related directly to slip at depth on the primary seismogenic fault plane. Although factors such as local seismogenic thickness, nucleation depth, fault dip, and geologic setting likely impact this probability, current empirical models mostly focus on earthquake magnitude as the main explanatory variable (e.g., Youngs et al., 2003; Petersen et al., 2011; Moss and Ross, 2011). Empirical models based on style of faulting and/or local tectonic setting have also been developed (Youngs et al., 2003; Moss and Ross, 2011; Takao et al., 2013, 2014), as well as models that look at both style of faulting and the local geomorphic setting as quantified by the topographic V_{S30} proxy method of Wald and Allen (2007) and Allen and Wald (2009)(Moss et al., 2013; 2018).

Probability of surface rupture models have been based on the logistic regression that fits dichotomous outcomes of empirical datasets (dataset of compiled earthquakes of magnitude m that did or did not produce surface-fault rupture):

$$P(SurfRup|m) = \frac{1}{1 + e^{a+bm}} \tag{3.1}$$

where a and b are constants fit to the data. Moss and Ross (2011) developed a database of global reverse-faulting events for a moment magnitude (Mw) range of 5.5 to 8.0 that did and did not rupture the surface by expanding the prior dataset of Lettis et al. (1997), and found values of $a = 7.30$ and $b = -1.03$ fit the data well. Compared to regression parameters fit to data from all styles of faulting and normal styles of faulting only (Youngs et al., 2003), the global reverse data suggest that the likelihood of surface rupture for reverse events is significantly lower than for normal events (Figure 3.1). One physical reason that may partially explain this difference is that rock and soil materials can sustain much higher compressive forces than tensile forces. See analytical solutions for reverse and normal faulting in section 5.1 of this report.

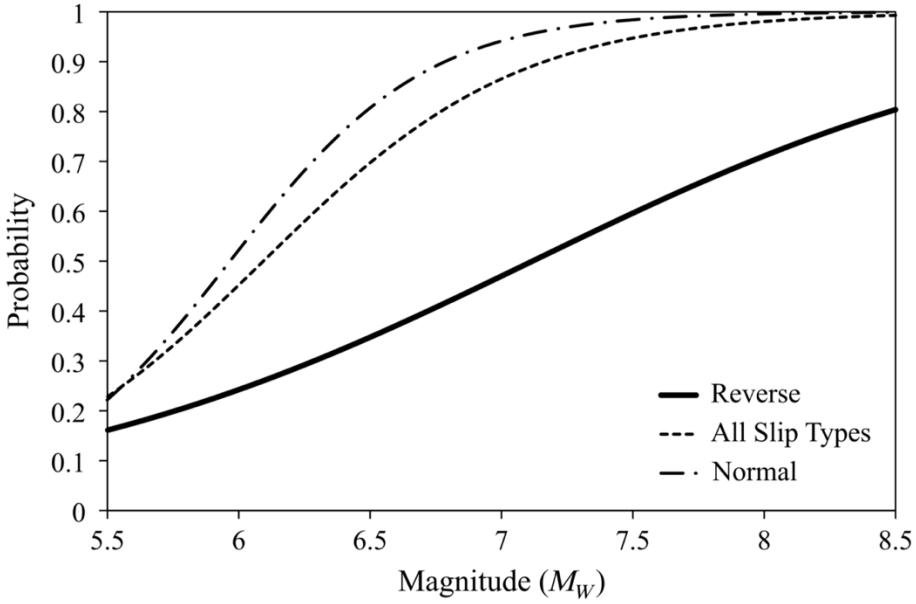

Figure 3.1. Probability of surface rupture for reverse, normal, and all slip types (after Moss and Ross, 2011).

Moss and Ross (2011) used Figure for their conditional probability of surface rupture given magnitude term, and found in a sensitivity analysis that this probability had highest impact on the resulting hazard curves compared to all other inputs. Subsequent work by Moss et al. (2013) investigated more reverse mechanism data to provide a revised logistic regression for forecasting surface rupture. Many predictor variables were tested (e.g., depth to top of seismogenic fault plane, width of seismogenic fault plane) but the topographic-slope proxy values of V_{S30} provided the most predictive power, and Moss et al. (2013) interpreted this to reflect differences in near-surface soil stiffness. Figure .2 shows the results of this statistical study for reverse and strike slip mechanisms. In the logistic regression a p-value less than 0.05 was achieved for all curves.

The logistic function used in fitting the dichotomous data was the same as before, but the function accounted for more input variables:

$$P(SurfRup|m, V_{S30}) = \frac{1}{(1 + e^{-z})} \tag{3.2}$$

The input function is defined as a linear combination of regression coefficients β and independent variables x.

$$z = \beta + \beta_1 x_1 + \beta_2 x_2 \tag{3.3}$$

The moment magnitude range for the data evaluated in Moss et al. (2013) was 4.2 to 8.7. The resulting distributions for reverse faulting, with a proxy V_{S30} value of 600 m/s as the boundary between stiff and soft, were defined as:

$$z_{stiff} = -13.9745 + 2.1395(M_w) \quad (3.4)$$

$$z_{soft} = -6.2548 + 0.8308(M_w) \quad (3.5)$$

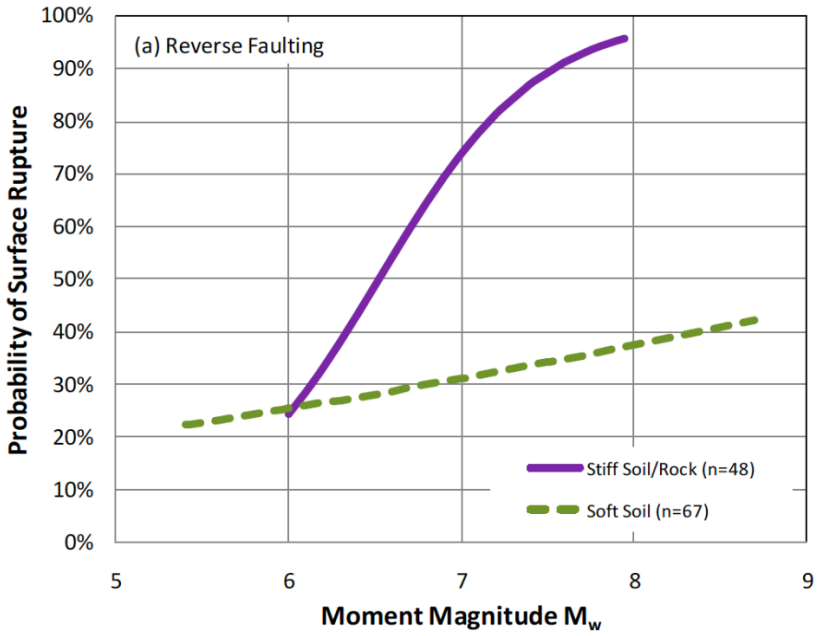

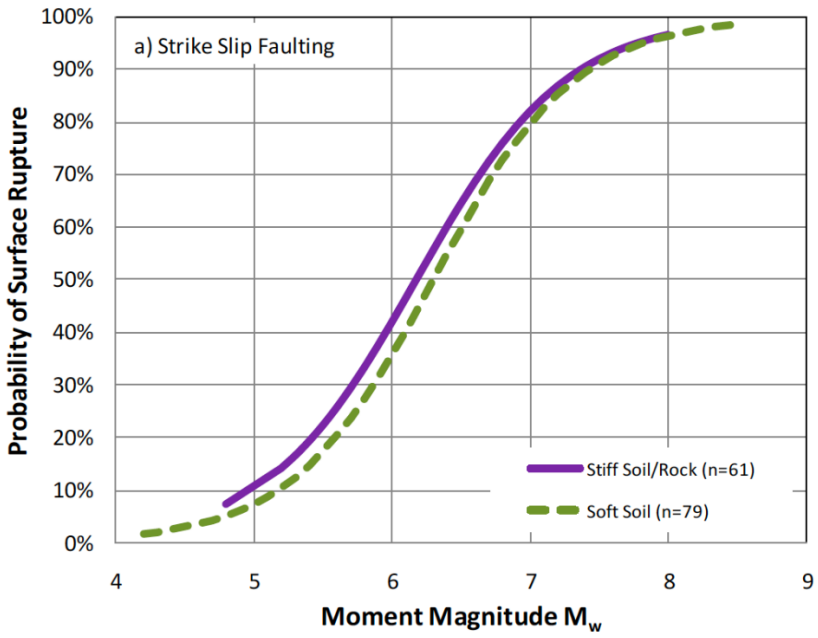

Figure 3.2. Probability of surface rupture for reverse and strike slip mechanisms (after Moss et al., 2013). The topographic-slope-derived thirty meter shear wave velocity value of 600 m/s was used as the boundary between stiff and soft.

Follow up research by Moss et al. (2018) used physical fault box studies, analytical models, and numerical simulations to further develop the understanding behind the likelihood of displacement at depth propagating to the ground surface. It was found that the stiffness of near-surface soils influenced the thickness of the shear band (Figure 3.3). Strain-hardening soils (i.e., soft) tend to have wide shear bands that absorb and diffuse deformations as they propagate upwards thereby requiring more basal deformation to rupture the ground surface. Strain-softening soils (i.e., stiff) have narrow shear bands that aid in propagating basal deformations to the ground surface. It was also found that, compared to initial rupture of undisturbed soil, repeat ruptures on the same plane required less basal deformation to rupture the ground.

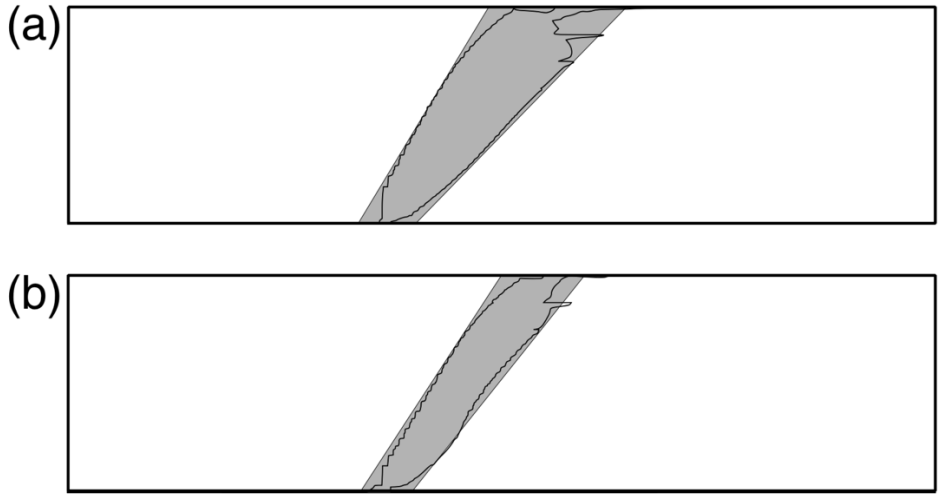

Figure 3.3. The influence of soil stiffness on propagation of deformations to the surface through 40 m of particulate material. Figure (a) is a simplified cross-sectional view of a shear band developed in a strain hardening or contractive material with a thirty meter shear wave velocity less than 600 m/s, whereas Figure (b) shows a shear band developed in a strain softening or dilatant material with a thirty meter shear wave velocity of more than 600 m/s. The narrower shear band in the stiffer soil ruptured to the surface with less basal displacement compared to the softer soil (after Moss et al., 2018).

As cautioned by Moss et al. (2018), the correlation of a topographic slope-derived proxy for V_{S30} with the probability of surface rupture for reverse faults may be related to factors other than near-surface soil stiffness. For example, the topographic roughness and average slope in active reverse faulting environments may correlate with areas more likely to be crossed by emergent faults (i.e., faults intersecting the surface that can be traced by geologic mapping) versus areas more likely to be underlain by blind faults (with tops of the faults located kilometers below the surface). An example would be the San Fernando basin area of southern California, where the active, reverse Santa Susana fault has been mapped across the rugged slopes of the Transverse Ranges directly north of the basin, and the Northridge blind thrust fault has been identified beneath the gentle slopes of the basin. In this example, the topographic slope—and by extension, any topographic slope proxy—has an association with the type of reverse fault likely to be encountered. Steeper

slopes are crossed by emergent fault strands of the Santa Susana fault zone (capable of surface-fault rupture), whereas the gentle, relatively smooth slopes of the basin are underlain by blind faults that are incapable of surface-fault rupture given their geometry. The potential for surface-fault rupture in this case is controlled by the types of tectonic structures that have developed in each environment and has no direct relationship with near-surface soil properties. Given such concerns, application of V_{S30} data to inform the applicable conditional probability of surface rupture model should be done with some caution and on a project-specific basis.

As an alternative to empirical models of the conditional probability of surface rupture, which rely on an underlying assumption of completeness of data for both surface rupturing and non-rupturing earthquakes, one may develop a numerical approach to solve for the conditional probability of surface rupture. Youngs et al. (2003) note that this alternative may be implemented directly within a hazard code, which can place earthquake ruptures on a gridded, modeled fault plane according to magnitude-area scaling relations and aspect ratio scaling rules. Such approaches may then explicitly account for fault scaling relationships and local factors such as fault source width. We note that these numerical approaches may be performed within or outside the hazard code, and may use available magnitude-area and aspect ratio scaling models (e.g., Wells and Coppersmith, 1994; Leonard, 2010; 2014; Thingbaijam et al., 2017; Chiou and Youngs, 2008; Hanks and Bakun, 2008; 2014; Shaw, 2009; 2013) as well as models for earthquake hypocenter depth distributions and depth ratios (Chiou and Youngs, 2008; Goulet et al., 2018).

4 Probability of Principal Displacement

4.1 SPATIAL DISPLACEMENT VARIABILITY

The probability term $P(D > D_0|m, x/L, SurfRup)$ describes the probability of exceedance of a specified level of displacement given that surface rupture has occurred. This probability may be expressed as a complementary cumulative distribution function that is based on empirical data. It can be determined from two probability distributions: a distribution for the variability of displacement along the strike of the fault, and a distribution of the average or maximum displacement.

Moss and Ross (2011) developed the distribution of variability along strike using 9 reverse events from Wesnousky (2008) and Kaneda et al. (2008). The earthquake ruptures that were analyzed include the following: 1896 Rikuu, 1945 Mikawa, 1971 San Fernando, 1979 Cadeaux, 1980 El Asnam, 1986 Marryat, 1988 Tennant Creek, 1999 Chi Chi, and 2005 Kashmir. The displacement measurement locations were normalized by the total rupture length and were treated as symmetric by folding at the midpoint of the fault rupture, or at x/L=0.5 (Figure 4.1). An assumption underlying the normalization is that patterns of primary surface faulting are scale independent, which we consider to be reasonable given studies of earthquake scaling (e.g., Savage and Brodsky, 2011). The folding approach is supported by Wesnousky (2008) and Biasi and Weldon (2006), and although we note that asymmetric surface ruptures are common (Manighetti et al., 2005), such asymmetric ruptures can be reasonably represented in the folding approach as there is no prior information currently available to anticipate the asymmetry direction. After normalization and folding, the ends of the rupture are at $x/L = 0$ and the midpoint of the rupture is at $x/L = 0.5$. The displacement amplitudes are plotted as normalized by either the average or the maximum displacement (Figure 4.1).

For statistical analysis, Moss and Ross (2011) grouped the data by 5% bin widths or 0.05 normalized units. A variety of statistical distributions (including normal, lognormal, beta, gamma, and Weibull) were fit to the binned data, and the fits were scored using Anderson-Darling goodness-of-fit tests (D'Agostino and Stephens, 1986). A confidence level of 99% was used to judge which distributions fit best. It was found that gamma, Weibull, and beta were roughly equivalent in fitting the binned data; normal and lognormal distributions did not fit the data as well. The fitting did not require normalized displacements to be zero at the ends of the ruptures, in part because by using binned data there are nonzero displacements near the ends.

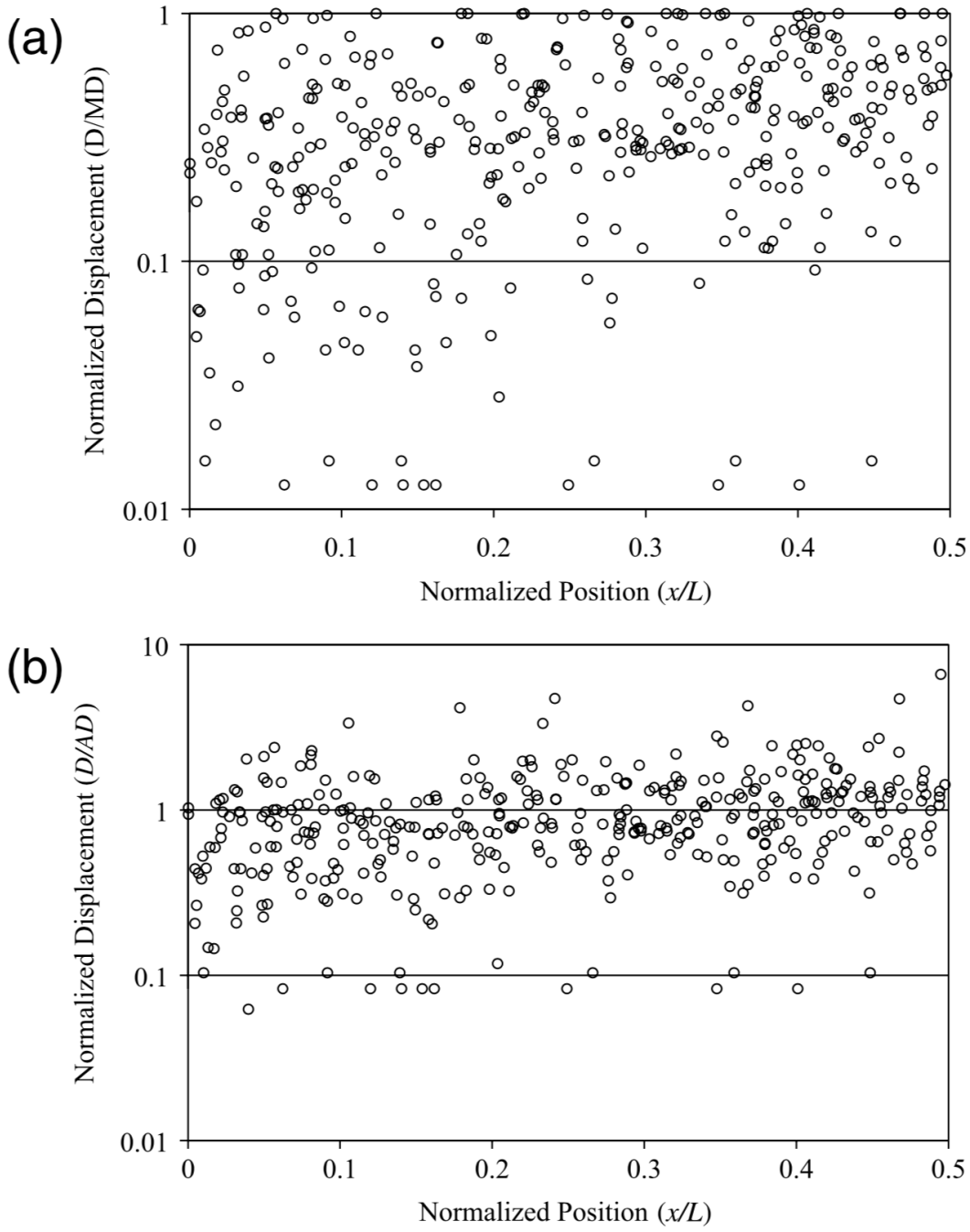

Figure 4.1. Normalized displacement measurements from Moss and Ross (2011) using data from Wesnousky (2008) and Kaneda et al. (2008). A normalized position along strike of $x/L = 0$ is the end of the fault and $x/L = 0.5$ is the midpoint of the fault. Plot (a) shows the vertical displacement normalized by the maximum, D/MD, and plot (b) shows it normalized by the average, D/AD.

The FDHI project has provided new reverse-faulting displacement events and new interpretations of existing events since Moss and Ross (2011) that lends to a replacement of the Moss and Ross (2011) probability distributions. Information from 25 reverse and reverse-oblique events (Table 4.1) in the FDHI database (Sarmiento et al., 2021) was parsed and the vertical displacements were folded and binned in a similar manner as described above. Similar to Moss and Ross (2011), the displacement distributions of binned *x/L* data had best fits to the gamma and Weibull distributions. The gamma distribution (Equation 4.1) results for D/AD and D/MD are presented below. Here the gamma distribution is using fitting parameters *a* (shape) and *b* (rate) with an example of the fit shown in Figure 4.2.

$$f(z) = \frac{b^a}{\Gamma(a)} z^{a-1} e^{-bz} \tag{4.1}$$

Gamma distribution parameters for D/AD for all FDHI reverse and reverse-oblique data are as follows (showing preferred values and 5% and 95% confidence level values in square brackets):

a = 2.54199 [2.34415, 2.75653] (4.2)
b = 0.393391 [0.359691, 0.430249]

Gamma distribution parameters for D/MD for all FDHI reverse and reverse-oblique data are as follows (preferred and 90% confidence interval values as above):

a = 2.11095 [1.94833, 2.28715] (4.3)
b = 0.180981 [0.165331, 0.198112]

When using the gamma distribution, the first and second moments can be calculated from the distribution parameters as:

Mean=a*b (4.4)
Stdev=sqrt(a*b^2)

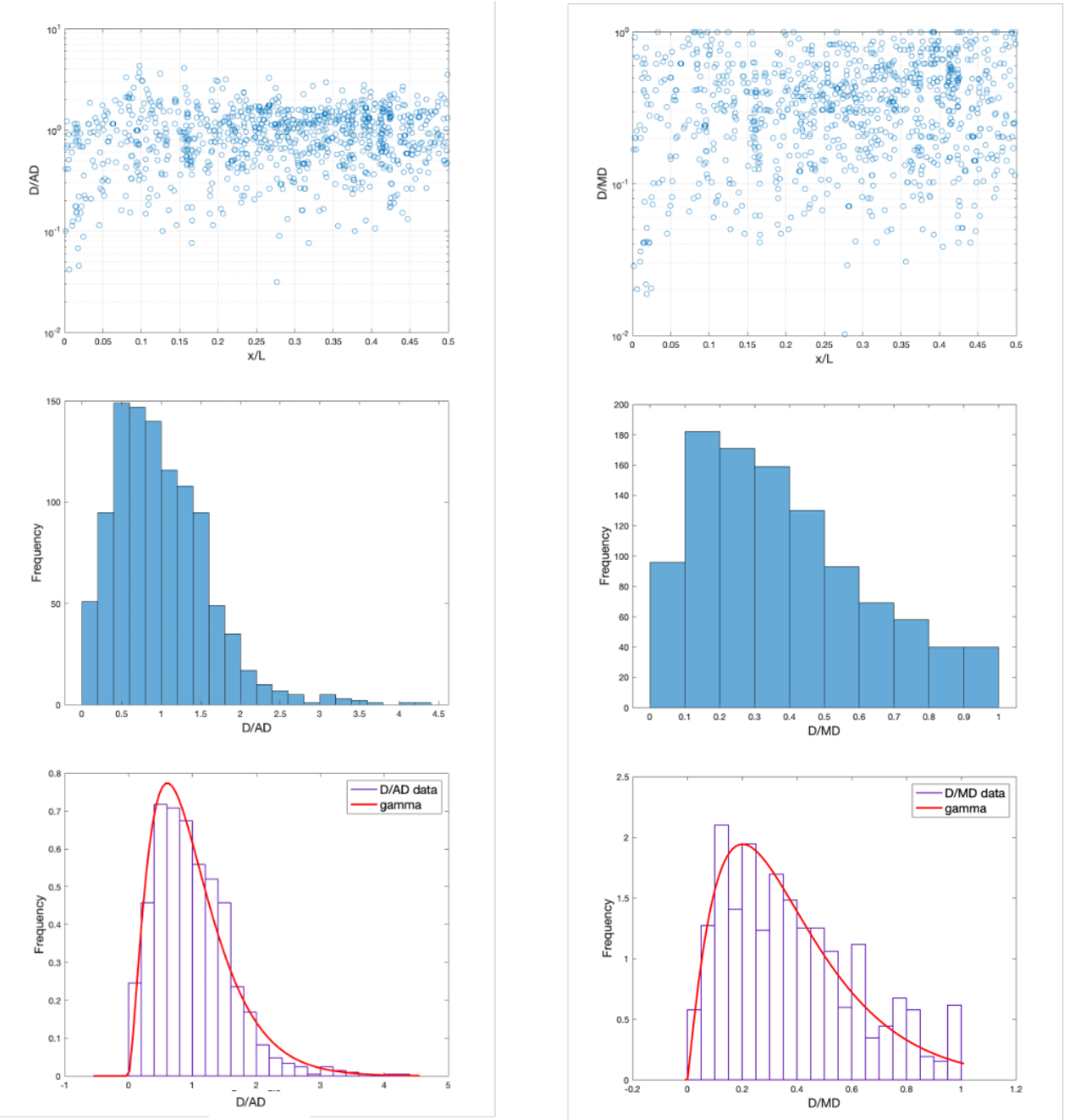

Figure 4.2. D/AD (left) and D/MD (right) versus x/L scatter plot, frequency plot, and distribution fit for all FDHI events analyzed in this study.

Gamma distribution parameters as a function of x/L bins were treated as linear and are shown in Figures 4.3 and 4.4. The linear interpretation was used for lack of justification for a higher order fit (e.g., polynomial).

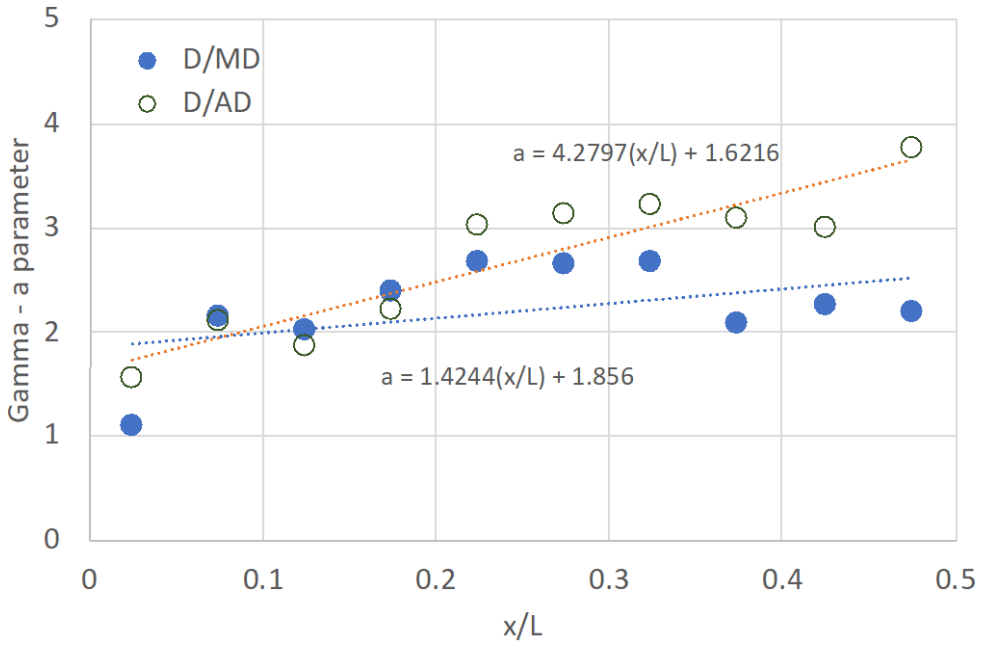

Figure 4.3. Gamma distribution parameter- a - for D/MD and D/AD.

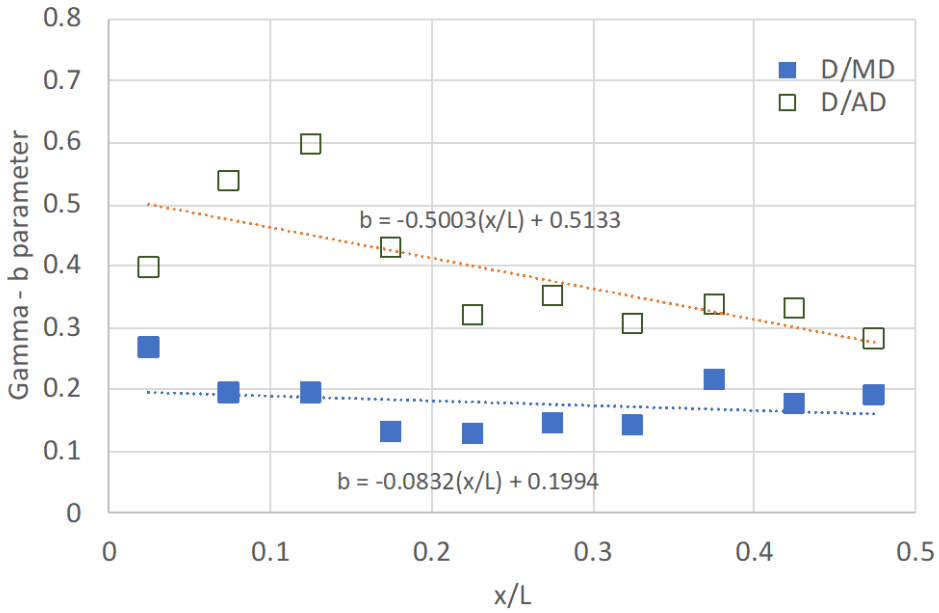

Figure 4.4. Gamma distribution parameter- b - for D/MD and D/AD.

4.2 AVERAGE AND MAXIMUM VERTICAL DISPLACEMENT VS MAGNITUDE

Our approach of using normalized displacements as a function of along-strike location (e.g., $D/MD(x/L)$) to model displacement hazard requires compatible relationships for scaling the normalized values. Our approach is to follow established methodologies and use log-linear relationships between AD and M_W and MD and M_W (e.g., Wells and Coppersmith, 1994; Moss and Ross, 2011). In order to develop candidate AD and MD scaling models applicable to reverse and reverse-oblique styles of faulting, we updated earlier empirical databases (e.g., Moss and Ross, 2011) by reviewing rupture information in the FDHI database (Sarmiento et al., 2021) and recent literature. In addition to using empirical data, we examine a simple theoretical displacement-magnitude scaling relation as a check on the empirical results. Using this information, we develop criteria for distinguishing different classes of reverse surface-fault ruptures, and construct log-linear AD-M_W and MD-M_W models for these different classes.

4.2.1 EMPIRICAL DATABASE AND SELECTION OF INTENSITY MEASURE

Our empirical database contains 60 historical, global earthquakes with reverse or reverse-oblique styles of faulting that produced surface-fault rupture with reported AD and/or MD information (Table 4.1). All events have estimates of M_W and MD, and 32 have estimates of AD. The primary sources of information for magnitudes and AD values are the FDHI database (25 events; Sarmiento et al., 2021) and Wells and Coppersmith (1994) (4 events). Most MD values are from the Lettis et al. (1997) compilation utilized by Moss and Ross (2011) (30 events) and the FDHI database (25 events). In all cases the AD or MD values from the FDHI database superseded the values used previously by Moss and Ross (2011). In addition, all 15 reverse earthquakes in the SURE 1.0 database (Baize et al., 2020) were reviewed and found to be also represented in the FDHI database. For these earthquakes in common, the MD and AD values in Table 4.1 are based on analysis of the FDHI database (instead of the SURE 1.0 database) because it is the more recent of the two and has more extensive documentation.

For earthquake magnitudes, FDHI-reported values of M_W are adopted for 24 or the 25 FDHI events in the database. The one exception is the magnitude estimated for the 31 August, 1896 Rikuu, Japan earthquake. In our database, this event is assigned M_W 7.2 based on the M_{JMA} 7.2 reported in current earthquake catalogs of Japan and an assumed ~1:1 conversion at this magnitude level (Utsu, 2002). This value is substantially higher than the M_W 6.7 in the FDHI database but lower than the M_W 7.4 listed for the earthquake by Moss and Ross (2011). The FDHI value is based on the Takao et al. (2013) reported moment magnitude value that is derived based on a linear magnitude conversion of $M_W = 0.78M_{JMA} + 1.08$. We infer this magnitude conversion equation to be applicable to a lower magnitude range than the Rikuu earthquake. For earthquake magnitudes of other (non-FDHI) events, the M_W values from Moss and Ross (2011) are adopted. Moss and Ross (2011) used the magnitude conversion equations from Heaton et al. (1986) to estimate M_W from other reported magnitudes compiled by Wells and Coppersmith (1994), Lettis et al. (1997), and others.

Table 4.1. Database of Historical Reverse and Reverse-Oblique Earthquakes with Documented Surface-Fault Displacement

Number	Date	Event	Location	M_W	AD[1] (m)	MD[1] (m)	Sources
1	05/08/1847	Zenkoji	Japan	7.4		**2.4**	Lettis et al. (1997)
2	08/31/1896	Rikuu	Japan	7.2	**2.1**	**3.6**	FDHI
3	12/23/1906	Manas	China	7.95		*5*	Lettis et al. (1997)
4	1/23/1909	Silakhar	Iran	7.23		*2.5*	Lettis et al. (1997)
5	1/3/1911	Chon Kemin	Kyrgyzstan	8.02	**3.5**	**9.0**	FDHI
6	4/18/1911	Raver	Iran	6.29		*0.5*	Lettis et al. (1997)
7	5/1/1929	Baghan	Iran	7.51		*2.1*	Lettis et al. (1997)
8	6/17/1929	White Creek	New Zealand	7.89		*5.2*	Lettis et al. (1997)
9	5/6/1930	Salmas	Iran	7.6		**5**	Lettis et al. (1997)
10	2/2/1931	Hawkes Bay	New Zealand	7.89		*4.6*	Lettis et al. (1997)
11	12/25/1932	Changma	China	7.82	*2.0*	**4.0**	Wells & Coppersmith (1994); Lettis et al. (1997)
12	11/28/1933	Behabad	Iran	6.29		*1.0*	Lettis et al. (1997)
13	4/21/1935	Tuntzhuchio	Taiwan	7.23		**3.0**	Lettis et al. (1997)
14	1/15/1944	San Juan	Argentina	7.6		**0.6**	Lettis et al. (1997)
15	1/13/1945	Mikawa-Fukozu	Japan	6.7	**1.2**	**2.4**	FDHI
16	3/17/1947	Dari	China	7.89		*5.0*	Lettis et al. (1997)
17	7/21/1952	Kern County	California, USA	7.36	**0.42**	**1.2**	FDHI
18	2/12/1953	Torud	Iran	6.6		*1.4*	Lettis et al. (1997)
19	12/13/1957	Farsinaj	Iran	6.91		*1.0*	Lettis et al. (1997)
20	9/1/1962	Ipak	Iran	7.42		*0.8*	Lettis et al. (1997)
21	5/24/1968	Inangahua	New Zealand	7.1		0.52	Lettis et al. (1997)

Number	Date	Event	Location	M_W	AD[1] (m)	MD[1] (m)	Sources
22	10/14/1968	Meckering	Australia	6.59	**0.96**	**2.0**	FDHI
23	7/24/1969	Pariahuanca	Peru	6.1		**0.4**	Lettis et al. (1997)
24	10/1/1969	Pariahuanca	Peru	6.6		**1.2**	Lettis et al. (1997)
25	3/10/1970	Calingiri	Australia	5.03	**0.18**	**0.33**	FDHI
26	2/9/1971	San Fernando	California, USA	6.61	**0.47**	**1.0**	FDHI
27	4/10/1972	Qir	Iran	6.8		*0.1*	Lettis et al. (1997)
28	9/6/1975	Lice	Turkey	6.6	*0.5*	**0.6**	Wells & Coppersmith (1994); Lettis et al. (1997)
29	1/1/1977	Mangya	China	6.1		*0.3*	Lettis et al. (1997)
30	9/16/1978	Tabas	Iran	7.4	*1.5*	*3.0*	Wells & Coppersmith (1994); Lettis et al. (1997)
31	6/2/1979	Cadoux	Australia	6.1	**0.4**	**1.4**	FDHI
32	10/10/1980	El Asnam	Algeria	7.3	**1.8**	**5.0**	FDHI
33	6/11/1981	Golbaf	Iran	6.6		*0.11*	Lettis et al. (1997)
34	7/27/1981	Sirch	Iran	7.1		*0.50*	Lettis et al. (1997)
35	6/11/1983	Coalinga Nuñez aftershock	California, USA	5.4		*0.64*	Lettis et al. (1997)
36	8/23/1985	Wuqai	China	6.89		*1.6*	Wells & Coppersmith (1994)
37	3/30/1986	Marryat Creek	Australia	5.7	**0.34**	**1.1**	FDHI
38	1/22/1988	Tennant Creek (Kunayungku)	Australia	6.27	**0.39**	**0.9**	FDHI
39	1/22/1988	Tennant Creek (LSW)	Australia	6.44	**0.58**	**1.1**	FDHI
40	1/22/1988	Tennant Creek (LSE)	Australia	6.58	**0.61**	**1.8**	FDHI
41	12/7/1988	Spitak	Armenia	6.77	**0.90**	**1.6**	FDHI
42	10/29/1989	Chenoua	Algeria	6.0		**0.12**	Lettis et al. (1997)

Number	Date	Event	Location	M_W	AD[1] (m)	MD[1] (m)	Sources
43	12/25/1989	Ungava	Canada	6.0	*0.80*	**1.8**	Wells & Coppersmith (1994); Lettis et al. (1997)
44	6/20/1990	Rudbar-Tarom	Iran	7.4		**1.0**	Lettis et al. (1997)
45	8/19/1992	Suusamyr	Kyrgyzstan	7.2		*4.2*	Lettis et al. (1997)
46	9/29/1993	Killari-Latur	India	6.2	**0.49**	**0.80**	FDHI
47	9/3/1998	Iwate (Inland)	Japan	5.8	**0.22**	**0.38**	FDHI
48	9/21/1999	Chi-Chi	Taiwan	7.62	**2.6**	**9.8**	FDHI
49	6/22/2002	Avaj	Iran	6.5	*0.7*	*0.8*	Walker et al. (2005)
50	2/22/2005	Zarand	Iran	6.4		*1.0*	Talebian et al. (2006)
51	10/8/2005	Kashmir	Pakistan	7.6	**1.5**	**7.1**	FDHI
52	10/10/2007	Katanning	Australia	4.7	*0.17*	*0.3*	King et al. (2019); Yang et al. (2021)
53	5/12/2008	Wenchuan	China	7.9	**2.2**	**6.0**	FDHI
54	3/23/2012	Pukatja	Australia	5.18	**0.15**	**0.48**	FDHI
55	10/15/2013	Bohol	Philippines	7.1	**1.4**	**5.2**	FDHI
56	11/22/2014	Nagano	Japan	6.2	**0.48**	**1.2**	FDHI
57	5/20/2016	Petermann	Australia	6.0	**0.25**	**0.90**	FDHI
58	11/13/2016	Kaikoura	New Zealand	7.8	**2.2**	**10.3**	FDHI
59	11/8/2018	Lake Muir	Australia	5.3	*0.28*	*0.75*	King et al. (2019); Yang et al. (2021)
60	11/11/2019	Le Teil	France	4.9	**0.05**	**0.11**	FDHI

Notes:

1. AD and MD values in bold are measures of vertical offset (vertical separation and/or scarp height). Values in italics are cases where the vertical offset value was not specifically provided, and these values may represent vertical offsets, some combination of vertical and horizontal displacement, or net displacements.

All earthquakes in the database occurred in continental settings in both active deforming crust and stable continental crust. The earthquakes span the period 1847 to 2019 and range in estimated moment magnitude from M_W 4.7 to 8.02 (Figure 4.5). Although the distribution is global, a full quarter of the events (15) are from Iran, and 11 are from Australia. The MD values for the earthquakes from Iran and Australia are indicated by circle and square symbols, respectively. Adding three earthquakes in Canada, France, and India to the 11 Australia

earthquakes, 14 events (23%) represent stable continental and/or low seismicity settings. A slight majority (31 of 60) are from active crustal settings other than Iran, with most of these from China (6), Japan (5), New Zealand (4), and USA (3; all California).

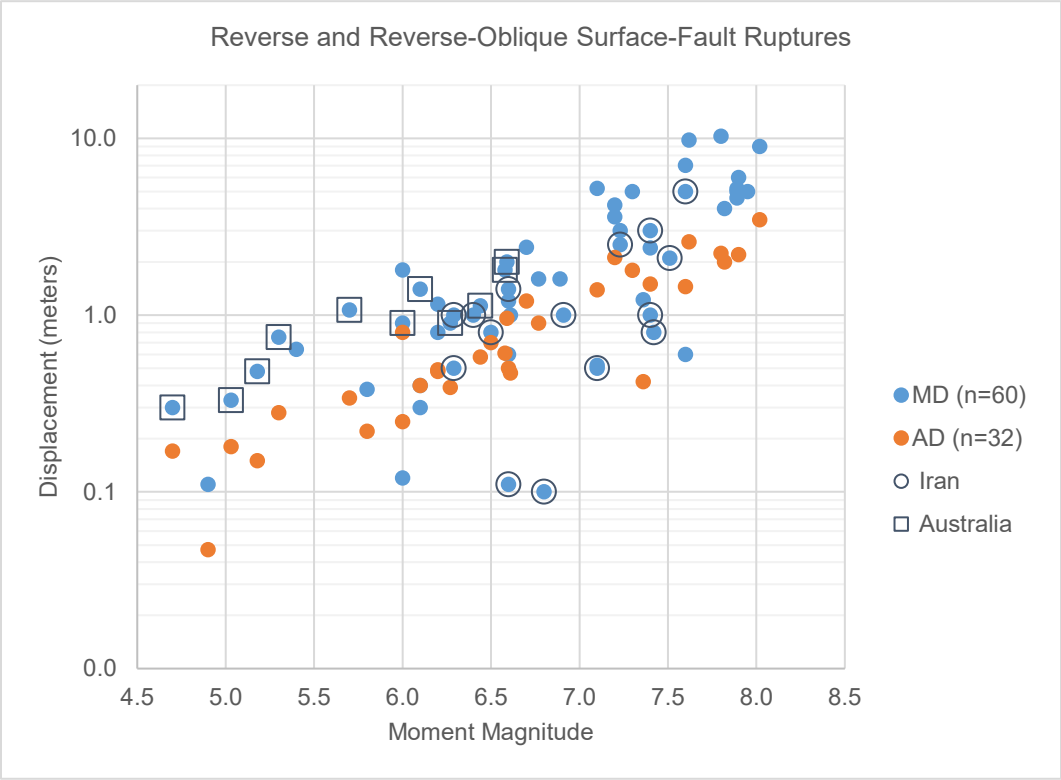

Figure 4.5. MD and AD data vs moment magnitude in the reverse and reverse-oblique fault rupture database. MD values for earthquakes in Iran and Australia are indicated by an open circle and square, respectively.

As discussed earlier in the report, our model approach is to use vertical displacement as the fault displacement intensity measure rather than net displacement. The decision to base our model on vertical displacement as the fault displacement intensity measure is based on our evaluation of available data, and in particular the meticulously documented data in the FDHI and SURE 1.0 databases. For clarity, the values of vertical displacement being discussed here are more specifically field-based measurements of either vertical separation or fault scarp height, and either can differ from the vertical component of displacement based on the offset feature being measured (e.g., Caskey, 1995; Yang et al., 2015). The values of AD and MD in Table 4.1 that are in bold type represent the vertical displacement component, either as documented in the FDHI database or as specified in the literature (e.g., Lettis et al., 1997). Values in italics are displacement measures for which a vertical component was not specified or could not be verified. These values may represent vertical displacement or some combination of vertical and horizontal displacement components. We assume these unspecified values are a reasonable estimate of the vertical component and include them in our analyses.

The detailed compilation of field measurements provided in the FDHI database suggests that there are few reliable measurements of net surface fault displacement for reverse and reverse-oblique earthquakes, in contrast to abundant measurements of vertical displacement (Table 4.2). Net displacement, of course, is a 3D vector consisting of orthogonal components of vertical displacement, fault-parallel horizontal displacement (right-lateral or left-lateral), and fault-normal horizontal displacement (shortening or extension). For reverse faulting earthquakes, the fault-normal shortening in a surface-fault rupture is related to the near-surface fault dip, and for faults with an intermediate or gentle dip this component represents a substantial portion of the net displacement. For reverse-oblique earthquakes and some reverse earthquakes, the amount of fault-parallel lateral displacement may represent a non-trivial fraction of the total as well. Despite this recognition that the two horizontal components of displacement are important for understanding net displacement of reverse-faulting earthquakes, the majority of displacement observations in the FDHI database include a record of a vertical displacement component but no record of a lateral or shortening component. In these instances, it is unclear whether these horizontal displacement values were indeterminate (due to lack of offset markers) or observed to be minor but left undocumented.

Table 4.2. Summary of number of principal displacement measures, displacement components, and ratios of vertical to net displacement where available.

FDHI Event	N, principal disp. measures[1]	Vert. disp.[2]	Fault-parallel disp.[3]	Fault-normal disp.[4]	3D (net) disp.[5]	Ratio, vert to 2D disp.[6]	Ratio, vert. to net disp.[7]
Bohol	121	121	0	0	0	n/a	n/a
Cadoux	33	22	7	0	4	n/a	*0.46*
Calingiri	27	21	6	0	0	n/a	n/a
Chi-Chi	218	217	127	90	0	0.84 (0.11–1.0)	0.66 (*n*=88) (0.18–1.0)
Chon Kemin	38	38	0	0	0	n/a	n/a
El Asnam	30	29	8	0	0	0.90 (0.64–1.0)	n/a
Iwate (Inland)	32	32	10	0	0	0.53 (0.05 to 0.86)	n/a
Kaikoura[8]	796	796	796	796	0	0.73 (0.24–0.75)	0.63 (*n*=142) (0.23–0.70)
Kashmir	236	230	20	3	0	1.0 (1.0–1.0)	n/a
Kern County	30	18	15	15	0	0.64 (0.07-0.96)	n/a

FDHI Event	N, principal disp. measures[1]	Vert. disp.[2]	Fault-parallel disp.[3]	Fault-normal disp.[4]	3D (net) disp.[5]	Ratio, vert to 2D disp.[6]	Ratio, vert. to net disp.[7]
Killari	10	8	3	0	0	*0.95*	n/a
Le Teil	6	5	0	1	0	n/a	n/a
Marryat Creek	73	73	0	0	0	n/a	n/a
Meckering	61	45	26	0	9	0.79 (0.51-0.98)	n/a
Mikawa-Fukozu	68	59	26	0	0	0.91 (0.71-1.0)	n/a
Nagano	96	81	1	63	0	0.66 (0.23-0.99)	n/a
Petermann	83	83	0	0	0	n/a	n/a
Pukatja	26	26	0	0	0	n/a	n/a
Rikuu	15	15	1	0	0	*0.0*	n/a
San Fernando	165	43	36	40	93	0.63 (0.31–0.97)	0.42 (*n*=5) (0.18–0.66)
Spitak	17	16	13	1	0	0.82 (0.71–1.0)	*0.55* (*n*=1)
Tennant Creek 1	17	16	1	0	0	n/a	n/a
Tennant Creek 2	11	11	0	0	0	n/a	n/a
Tennant Creek 3	36	35	0	0	1	n/a	n/a
Wenchuan[9], SW, G1	26	24	13	0	0	0.74 (0.27–1.0)	n/a
Wenchuan, SW, G2	120	119	16	0	0	0.41 (0.0–0.85)	n/a
Wenchuan, Tear, G1	33	32	29	0	0	0.74 (0.37–1.0)	n/a
Wenchuan, Tear, G2	136	136	28	0	0	0.69 (0.35–0.92)	n/a
Wenchuan, FT, G1	36	36	14	0	0	0.87 (0.57–1.0)	n/a
Wenchuan, FT, G2	32	32	0	1	0	*0.87*	n/a
Wenchuan, MF, G1	13	13	4	0	0	*0.86*	n/a

FDHI Event	N, principal disp. measures[1]	Vert. disp.[2]	Fault-parallel disp.[3]	Fault-normal disp.[4]	3D (net) disp.[5]	Ratio, vert to 2D disp.[6]	Ratio, vert. to net disp.[7]
Wenchuan, MF, G2	4	4	2	0	0	*0.94*	n/a
Wenchuan, NE, G1	91	91	54	0	0	0.68 (0.04-1.0)	n/a
Wenchuan, NE, G2	44	44	14	0	0	0.66 (0.43-0.86)	n/a

Notes:
1. Number of principal displacement measurements in FDHI database.
2. Number of vertical offset measurements. Most are vertical separation, but some are scarp height.
3. Fault-parallel displacement measurements, defined as right-lateral or left-lateral.
4. Fault-normal displacement measurements; most are shortening.
5. Three-dimensional, or net, displacement measurements. The numbers listed here are for cases where the net displacement was recorded, but the component parts were not recorded in the database
6. Ratio, vertical displacement to a 2D displacement. Vast majority of cases are of the 2D displacement consisting of a vertical and fault-parallel (lateral) component. A ratio of 0.71 indicates a 1:1 vertical to lateral displacement ratio. Values in italics are based on 4 measurements or fewer.
7. Ratio, vertical displacement to the 3D (net) displacement. There are very few cases where both the vertical and net displacement are reported. The italicized values for the Cadoux earthquake are based on a reported vertical displacement near a reported 3D displacement; the result is therefore unreliable.
8. The Kaikoura earthquake rupture was divided into 17 parts based on rupture pattern. The preferred values for the vertical displacement ratios shown are based on the four sections of the rupture that displayed a clear reverse displacement pattern; the range of ratios shown are based on the range of ratios calculated for each section; at a site-by-site scale, the range of vertical displacement ratios is much broader.
9. The Wenchuan earthquake rupture was divided into four parts: the southwest (SW) section, the tear fault, the frontal thrust, the parallel rupture behind the frontal thrust, and the northeast (NE) section. Also, there are two sets of rupture measurements that were analyzed separately and then averaged: Group 1 (G1) used vertical separation as the vertical measure; group 2 (G2) used scarp height as the vertical measure.

We recognize the non-trivial challenges of collecting post-earthquake offset measurements, especially offset measurements that capture the 3D net displacement vector. Fault-normal shortening is difficult to measure accurately in the field, as reverse fault scarps are commonly irregular and chaotic, bury the footwall piercing point, and often destroy the near-surface fault plane (e.g., McCalpin and Carver, 2009; Yeats et al., 1997). The fault-parallel horizontal component of surface displacement is also difficult to document for reverse events. Whereas vertically offset landforms and scarp faces are relatively common along reverse ruptures, clear lateral offset features are relatively rare, difficult to reconstruct, and often treated with secondary importance to a more imposing (and compelling) vertical offset feature. In addition, it is uncommon for field reports to record zero or minimal lateral offset along reverse earthquake ruptures unless the field investigators are particularly thorough.

A review of the FDHI database for the 25 reverse and reverse-oblique ruptures demonstrates that there are insufficient data to calculate net MD or AD for most of the events (Table 4.2), consistent with the known challenges to field data collection described above. Only two ruptures—the 1999 Chi-Chi and 2017 Kaikoura—have sufficient detail in measured displacement components such that a reliable estimate of net displacement may be calculated; the 1972 San Fernando earthquake may represent a third. Based on such incomplete documentation of a lateral component of slip (even if documenting a zero value), and a very low number of shortening measurements, we suspect that many surveys of historical earthquake

ruptures that report "net" displacements are more likely reporting just the vertical component or perhaps vertical and lateral only (but not shortening). Thus, we interpret the values for AD and MD in italics in Table 4.1 to be reasonable estimates of vertical displacement, and probably a closer estimate of vertical displacement than the 3D net displacement.

Using information from the Chi-Chi rupture plus sections of the Kaikoura rupture that had a dominant reverse component, we calculate average ratios of vertical displacement to net displacement of 0.63 (Kaikoura rupture, reverse-dominated sections) and 0.66 (Chi-Chi rupture). The point-specific variability in the vertical displacement to net displacement ratio varies from less than 0.2 to 1.0. A few other opportunities where the net displacement was measured suggest vertical to net ratio values of approximately 0.4 to 0.6. From these limited examples, we suggest a general approximation for converting vertical displacements to net displacements:

$$\mathrm{AD_V} \sim 0.6 \times \mathrm{AD_{NET}} \tag{4.1}$$

where AD_V is the average vertical component of displacement and AD_{NET} is the average net displacement for reverse and reverse-oblique faulting. For a general idea, the ratio value of 0.6 is consistent with a near-surface dip angle of approximately 40 degrees and a horizontal to vertical (H:V) displacement ratio of approximately 0.5. We emphasize that the variability of this ratio for any one earthquake rupture and at any point along a rupture is high and should be considered in any analysis.

There are many more opportunities to estimate the ratio of vertical displacement to a 2D displacement (combination of vertical and one horizontal displacement) (Table 4.2). These ratios, which generally range in rupture averages of about 0.6 to 0.9, represent maximum values for the ratio of vertical to net displacement. As these 2D displacements are mostly combinations of vertical and lateral displacement, this range in 2D ratios is consistent with H:V displacement ratios of 0.5 to 1.3.

With a focus on the fault displacement intensity measure of vertical displacement, values of MD_V were compiled and values of AD_V were calculated from the FDHI database and entered in Table 4.1. We hereafter use MD_V and AD_V when specification of the vertical component is important to distinguish from the net displacements. Otherwise, the terms MD and AD (no subscript) are used with the implied specification of the vertical component for our model.
The procedure used to harvest values from the FDHI database is as follows. First, data were filtered for principal and "cumulative" displacements only (distributed displacements and "total" displacements were removed). Measurements with a use recommendation of "Toss" were removed, such that records either judged "keep" or "check" were considered. If a preferred value is entered, the preferred value is considered. If no preferred value is provided, but a range (i.e., min and max) is recorded, the midpoint of the two is used, if available, and if only one bounding value is provided that value is considered after specific review. For each event, the maximum vertical amount (either scarp height or vertical separation) was used for the event MD_V.
The method for calculating AD_V from the FDHI data is less straightforward. First, data were filtered to preclude distributed displacement measurements, total measurements, and "Toss" records as described above for MD_V. For each record of either vertical separation (VS) or scarp height (SH), a preferred value is noted, if available. If there is no preferred value but a range is

provided, the midpoint of the two is noted. If only one bounding value is provided, that value is considered after specific review. Next, the spatial distribution of points is examined as well as rupture complexity such that data are grouped into separate sections. If the spatial distribution is generally uniform, all data are within one group. For more complex ruptures such as the 2008 Wenchuan and 2016 Kaikoura earthquakes, measurements are grouped by part of the rupture (e.g., Wenchuan contained a SW section, a Tear Fault section, a Frontal Thrust section, and Parallel Thrust section, and a NE section; Table 4.2). Within each group, the arithmetic mean of the vertical displacements is calculated. Our decision to use the arithmetic mean of the displacements—as opposed to the geometric mean or median—is based on our interpretation that most non-FDHI records of AD are closer to measures of the arithmetic mean, and thus the arithmetic mean provides the most consistent measure when combined with non-FDHI data. The arithmetic mean value of each group is combined with the other groups within each earthquake rupture by weighting based on the rupture length of the group as a fraction of the total rupture length.

The final database in Table 4.1 includes 32 values of AD and 60 values of MD. These data are plotted in Figure 4.5. All records have estimates of M_W, but other details such as rupture width, fault dip, nucleation depth, etc. have not been compiled. We have not compiled alternative estimates of M_W, MD, AD, nor have we developed quality (reliability) ratings for the different events. Implicit in the compilation is an assumption that there are no systematic errors in M_W, MD, or AD estimates across the database or systematic correlated errors between parameters.

4.2.2 DISPLACEMENT SCALING RELATIONS

A key objective of the MD & AD database is to derive empirical relations between MD or AD and M_W that can be used to scale the normalized displacements (D/MD or D/AD) that have model distributions as a function of x/L. As our primary application is hazard assessment for engineering evaluation, an objective of the final models is that they are provided with appropriate context regarding the earthquakes used to derive the model parameters and the underlying assumptions or interpretations of the data. Ideally, alternative models are presented, each with clear documentation of the criteria underlying the data selection process and intended applicability of the model.

As will be described below, we interpret several earthquakes in the database to have produced surface displacements that are much lower than would be expected given their magnitude, even accounting for natural variability. These events are named “incomplete” surface ruptures in contrast with “complete” surface ruptures that have displacements that scale more as expected given their moment magnitude. Our goal is to identify “incomplete” surface rupture events, filter them, and develop a set of AD_V-M_W and MD_V-M_W models based only on “complete” ruptures. We also develop models that incorporate the “incomplete” events, acknowledging that in the vast majority of examples the underlying data are unlikely to be flawed, and therefore the “incomplete” events represent physical examples of surface-fault displacements from reverse earthquakes. However, until it is better understood whether a particular tectonic setting, crustal fault geometry, etc. is associated with much-lower-than expected displacements, it is desirable for engineering applications to have a more conservative model available for consideration.

Conservatism in this case applies both to estimates of median scaling and the variability about the median. Even if the data indicating much-lower-than expected surface displacements are judged to be reliable, it is another question as to whether such data should be included in a regression to be used in hazard. Although it is current standard practice to develop mean-centered models with clear documentation of uncertainties and allow engineering design criteria and/or stakeholder decision-making to determine the appropriate hazard level for evaluation, it is also not reasonable to develop empirical models based on data that are not representative of the phenomena the model purports to capture. If a fault under investigation for a site-specific FDHA demonstrates geomorphic or geologic evidence of recent, relatively large surface-fault ruptures, for example, then an empirically-based model ideally is developed based on examples of past "complete" surface-fault rupture that have occurred on similar faults.

By inspection of Figure 4.5, there are a few data outliers that require some consideration as to whether they should be considered "incomplete" ruptures and filtered out for additional analysis. Several MD datapoints appear to have much lower than expected values, including the MD measurements that plot below AD values of comparable M_W. In particular, there are four values that have MD < 0.2 m, only one of which is associated with an earthquake M_W < 5.0. From our review of these examples, it seems highly likely that these low MD values are based on reliable measurements, and that more modern post-earthquake surveys would likely resolve different values but not change the MD estimates by an order of magnitude or even a factor of 4.

4.2.3 AD VS MAGNITUDE SCALING, INITIAL ANALYSIS

The AD data span a magnitude range of M_W 4.7 (Katanning, Australia) to M_W 8.02 (Chon Kemin, Kyrgyzstan) and a vertical displacement range of 0.05 m (2019 Le Teil, France) to 3.5 m (1911 Chon Kemin, Kyrgyzstan) (Figure 4.6). There are 11 AD values from Australia, which represent the vast majority of events in the $4.5 < M_W < 6.7$ range (indicated by boxes in Figure 4.6). The country with the next-highest number of events in the database is Japan (4 AD values; indicated by diamonds in Figure 4.6), which span a magnitude range of M_W 5.8 to 7.2. The data show a generally linear trend across the magnitude range for the log of the displacements, and we fit an initial least-squares linear regression to the entire dataset. Following Wells and Coppersmith (1994) and others, we report results in the form:

$$\log_{10} AD = a + bm + s\varphi, \tag{4.2}$$

where a and b are the intercept and slope of the best-fit regression line, respectively, m is magnitude in the moment magnitude scale, s is the standard error in the $\log_{10} AD$ value, which we take here to be equivalent to the standard deviation, and φ represents the standard normal probability density function.

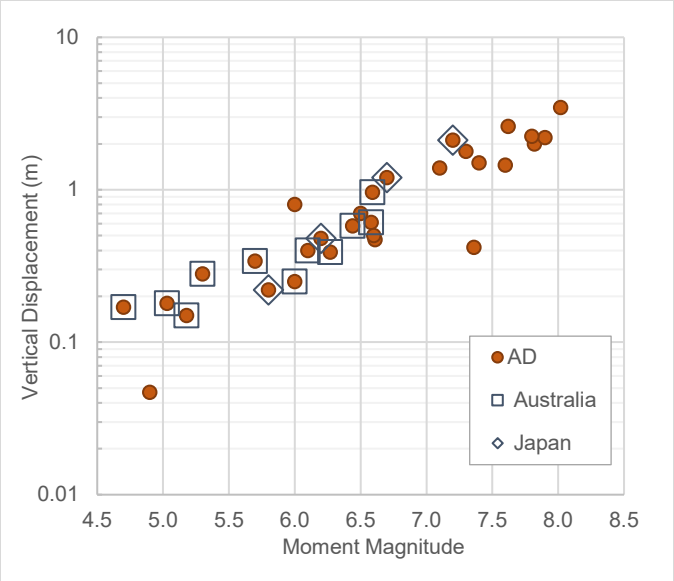

Figure 4.6. Log-linear plot of AD vs MW for the 32 reverse and reverse-oblique faults in the database. Australia and Japan events indicated by symbols.

The results of the initial fit to the 32 datapoints yields values of $a = -2.98$, $b = 0.427$, and $s = 0.18$. The preferred and ± 1s lines show a reasonable fit, with residuals being approximately equally distributed above and below the average line across all magnitudes (Figure 4.7).

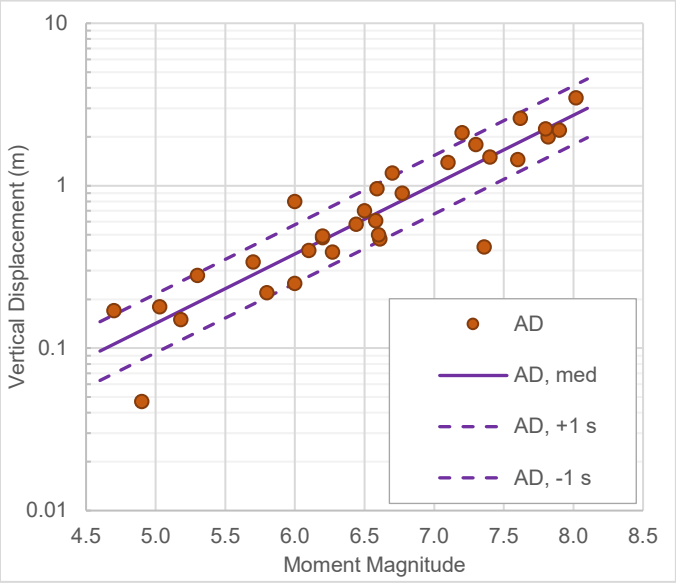

Figure 4.7. AD vs MW data with preferred least-squares linear regression line (solid) and ± 1 standard error lines (dashed).

The empirical AD data are also compared to a theoretical average displacement for dip-slip faults, which we will indicate as $\overline{D}$. To estimate $\overline{D}$, we combine the definition of M_W by Hanks and Kanamori (1979):

$$\log_{10} M_0 = \frac{3}{2} M_W + 9.05 \tag{4.3}$$

where seismic moment M_0 is in N·m, with the definition of M_0:

$$M_0 = \mu A \overline{D} \tag{4.4}$$

where μ is the shear modulus, A is rupture area, and $\overline{D}$ is the average displacement on the rupture plane. Substituting the seismic moment definition into equation (4.3) and rearranging, we get:

$$\log_{10} \mu + \log_{10} A + \log_{10} \overline{D} = \frac{3}{2} M_W + 9.05. \tag{4.5}$$

The value of μ may be treated as a constant, with commonly estimated values of approximately 3.0–3.3 × 10^{10} N/m^2. Also, we recognize that the constant in the moment magnitude definition is also commonly stated as 9.1 instead of 9.05 based on Kanamori (1977), and our decision to show 9.05 instead of 9.1 in Equation 4.3 is somewhat arbitrary. The difference in the moment magnitude definition constant and difference in estimated μ using values noted above results in a maximum impact of about 10% on estimated $\overline{D}$, which is small and is implicitly contained within our final estimation of M_W-$\overline{D}$ uncertainty. We continue with the constant of 9.05 and a value $\mu = 3.0x10^{10}\ N/m^2$ as that combination is centered reasonably well within the range of constant and μ combinations and is nearly identical to a combination of 9.1 and $\mu = 3.3x10^{10}\ N/m^2$ used by Leonard (2010).

Using the simple scaling arguments and empirical analysis by Leonard (2010) for dip-slip faulting, where $\log_{10} A \propto M_W$, we can use the Leonard (2010) relationship:

$$M_W = \log_{10} A - 2.0 + s\varphi, \tag{4.6}$$

where A is in m^2, and s and φ are the same as described for Equation 4.2. We estimate s, the standard deviation in M_W from A, to be approximately 0.1–0.2 based on examination of the literature and alternative proposed models (Wells and Coppersmith, 1994; Hanks and Bakun, 2002; 2008; 2014; Ellsworth, 2003; Leonard, 2010; Shaw, 2009; 2013). For fun and to incorporate uncertainties discussed above, we define a "useful" estimate of the standard deviation $s_u = 0.2$ in the analysis. Rearranging, substituting in the prior equation, and adopting $\mu = 3.0x10^{10}\ N/m^2$, the relation between $\overline{D}$ and M_W is:

$$\log_{10} \overline{D} = 0.5 M_W - 3.43 + 0.2\varphi. \tag{4.7}$$

The scaling-based $\overline{D}$ with ± 1 s_u is plotted along with the vertical surface AD data in Figure 4.8. The prediction is that $\overline{D}$ would be comparable to, but slightly higher than, the AD data for "complete" surface ruptures given our use of AD_V for the FDHI events and our interpretation that most other empirical AD data are based on vertical displacements and not net displacement.

Slightly higher $\overline{D}$ values also would be consistent with a proposed shallow slip deficit (e.g., Fialko et al., 2005; Xu et al., 2016; cf. Marchandon et al., 2021), whereby localized surface fault displacement is estimated to be less than the displacement at seismogenic depths (Dolan and Haravitch, 2014). In contrast, Figure 4.8 shows the theoretical $\overline{D}$-M_W model to provide a reasonable fit to the AD_V data, and several earthquakes at the lower magnitudes (all events with $M_W < 5.5$) show measured vertical AD_V values greater than those predicted by the model at the +1 s_u level.

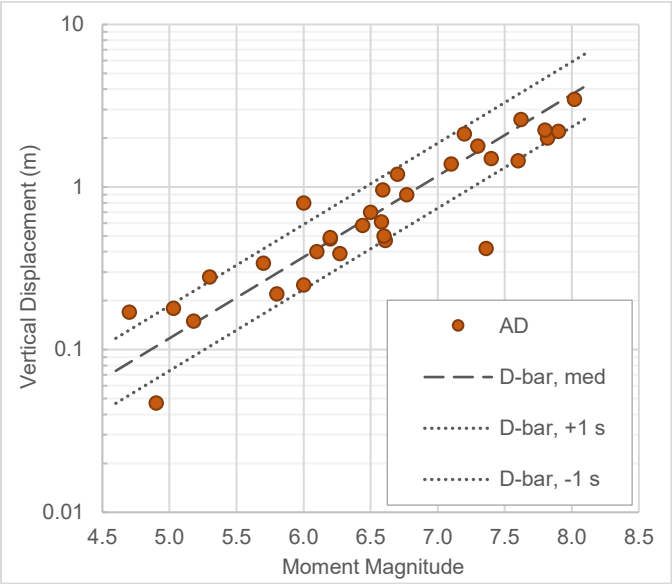

Figure 4.8. AD vs MW data with a theoretical log displacement-magnitude relation.

Plots of the data residuals to the two regressions (Figure 4.9) show reasonably unbiased results, with the residuals of the scaling-based relation showing the slight negative slope with magnitude that reflects the difference between the slope of the empirical regression (0.427) and the slope of the scaling-based equation (0.5). The empirical regression has a coefficient of determination (R^2) of 0.83, a residual sum of squares of 0.981, and a residual standard error (again -- assumed equivalent to the regression standard deviation) of 0.18. In comparison, the scaling-based equation has an R^2 value of 0.80, a residual sum of squares of 1.15, and an equivalent residual standard error (using the same n-2 = 30 degrees of freedom as the empirical regression) of 0.20. Given uncertainties in the M_W and AD values in the database, we consider both models to be useful for purposes of further data evaluation.

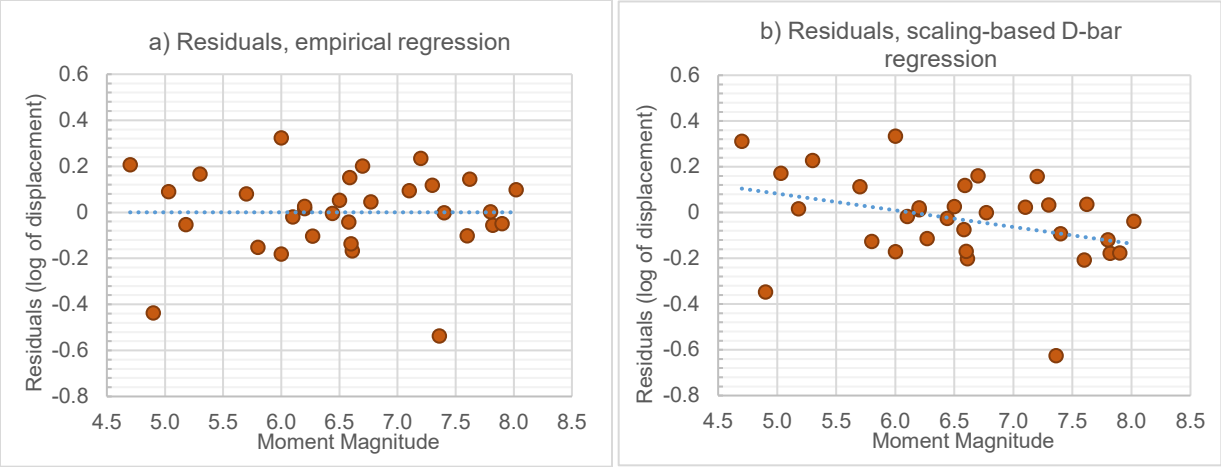

Figure 4.9. Plots of residuals of log10AD data to (a) the least-squares regression, and (b) the scaling-based regression.

We note that the event with the largest absolute residual in both regressions is the 1952 M_W 7.36 Kern County, California earthquake (Oakeshott, 1955). This earthquake, which ruptured the White Wolf fault at the southern margin of California's Central Valley, has long been recognized for the unusual surface-fault rupture (Buwalda and St. Amand, 1955), which included a blind rupture along its southwest portion (no surface rupture) and surface displacements much lower than expected given the earthquake magnitude and calculated displacement at depth (e.g., Bawden, 2001).

Another useful piece of information for evaluating whether certain AD or MD values in the database represent incomplete ruptures, and for evaluating whether certain values are problematic and may be of poor quality, is the evaluation of the ratio of MD to AD. This ratio is a simple measure of the variability of surface displacements about the average, although focused on the upper half of the displacement distribution. Figure 4.10 shows MD/AD versus M_W for the 32 reverse and reverse-oblique earthquakes in the database, with the solid line indicating the median value and dashed lines indicating the 10^{th} and 90^{th} percentile values.

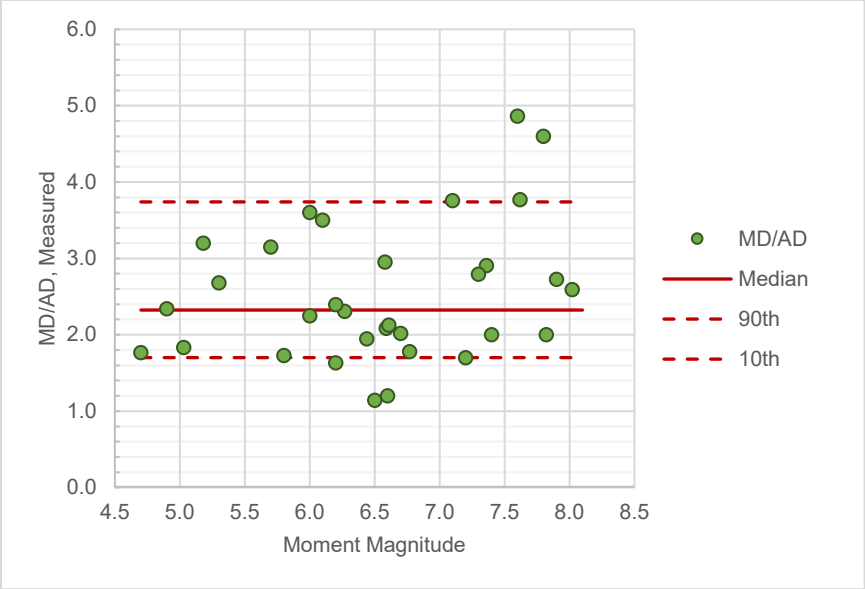

Figure 4.10. MD/AD ratios of the 32 events vs moment magnitude. Median ratio shown as a solid line, and 10th and 90th percentile ratios are dashed lines.

The plot shows no apparent relation between MD/AD and magnitude, and most of the data (between 10th and 90th percentiles) indicate a ratio of 1.7 to 3.7. The median value is 2.3. These results are generally similar to the findings of Wells and Coppersmith (1994) who point to a general rule of thumb that MD is approximately two times AD. Surface-fault ruptures with ratios close to 1 are unexpected, as these indicate little displacement variability and maximum displacements that are close to the average displacement. The events with the two lowest MD/AD ratios in Figure 4.10 are the 2002 M_W 6.5 Avaj, Iran earthquake (AD = 0.7 m; MD = 0.8 m) and the 1975 M_W 6.6 Lice, Turkey earthquake (AD = 0.5 m; MD = 0.6 m) (Table 4.1). The two events with the highest MD/AD are the 2005 M_W 7.6 Kashmir, Pakistan earthquake (AD = 1.5 m; MD = 7.1 m) and the 2016 M_W 7.8 Kaikoura, New Zealand earthquake (AD = 2.2 m; MD = 10.3 m) (Table 4.1). Although the Avaj and Lice earthquakes are not in the FDHI database, and therefore little analysis is available as to the thoroughness of the field surveys, the Kashmir and Kaikoura events are in the FDHI database and are well reviewed and vetted. Although one interpretation is that the AD and MD estimates for the Avaj and Lice earthquakes are unreliable, an alternative is that the low MD/AD ratios may be an attribute of an incomplete surface rupture, in that the up-dip rupture extent included the ground surface but perhaps not sufficiently to reflect the displacement variability and/or absolute amounts that occurred at depth. We note that at this point we are not filtering any events based on MD/AD from use for log *D* - M_W scaling relations, but rather the intention is to explore the average and range of MD/AD ratios as indicators of the expected natural variability for a complete rupture.

4.2.4 EVALUATING MD DATA FOR INCOMPLETE

The empirical and scaling-based $\log_{10}$AD - M_W relations, combined with estimates of MD/AD, are used to evaluate the broader MD database and identify outlier events that are candidates for "incomplete" ruptures. To restate our objective, we want to develop $\log_{10}$AD-M_W and $\log_{10}$MD - M_W models useful for predicting displacements that are representative of "complete" reverse or reverse-oblique surface-fault rupture, which we informally define as earthquakes producing surface displacements that are generally comparable to displacements over the full rupture plane at depth. Separately, we can also develop models based on the events interpreted as producing "incomplete" surface-fault ruptures such that practitioners can have the flexibility to include a combination of models in a weighted logic-tree approach.

Figure 4.11 is a log-linear plot of $\log_{10}$MD vs M_W for the 60 reverse and reverse-oblique events in the database. Also shown are solid and dashed lines representing the empirical $\log_{10} AD - M_W$ and scaling-based $\log_{10} \overline{D} - M_W$ relations. Events with estimated vertical MD values that plot below and near the predicted average displacement lines are suspected of representing incomplete ruptures according to our general definition. However, our goal is to develop a mean-centered model for complete ruptures, and therefore we need to consider cases where AD is below average but still "complete."

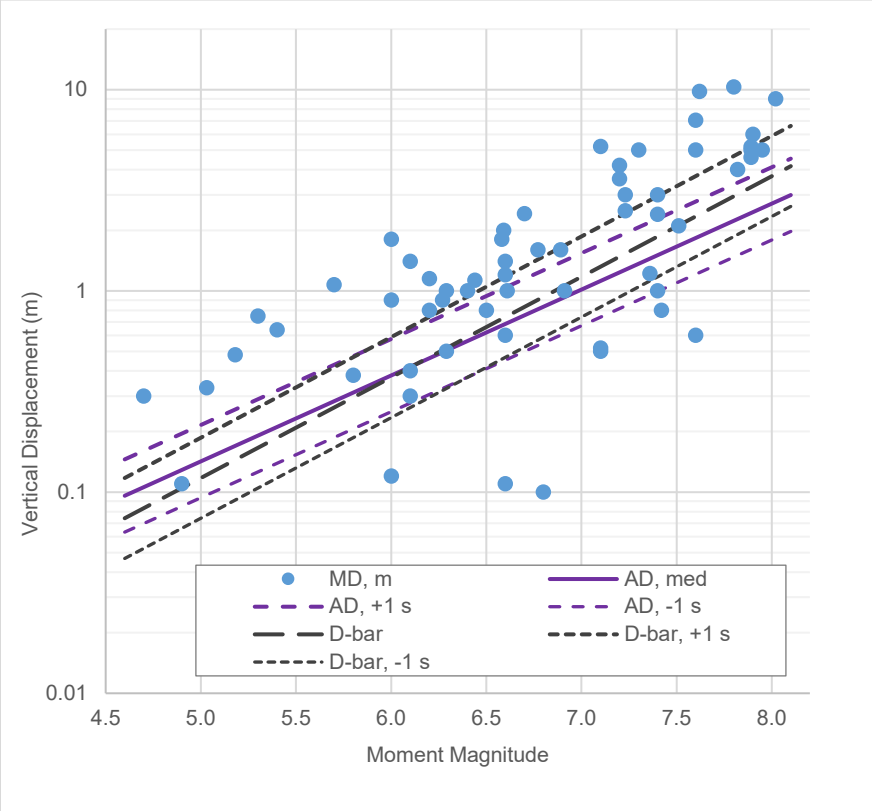

Figure 4.11. Estimated vertical MD vs MW data showing alternative relations for average displacement. MD values that plot below the predicted AD lines are candidates for incomplete surface-fault rupture.

For filtering criteria, we only want to exclude events where the MD is less than expected even for cases of a below-average AD (but still within an expected range for a "complete" rupture). To do this, we consider two criteria. First, we evaluate predicted $\overline{D}$ and AD values at the -1 standard deviation level, using our estimated "useful" standard deviation of $s_u = 0.2$ for the theoretical $\overline{D}$ model and $s_{AD} = 0.18$ for the empirical AD model. Second, we assume the MD/AD ratio is not less than a factor of 1.7 (the 10th percentile value from the dataset; Figure 4.10), which retains a minimum of expected rupture variability between AD and MD. Events failing these criteria are flagged as incomplete and removed from the regression analysis for complete ruptures.

Our criteria for characterizing an event as an incomplete rupture uses a minimum threshold line defined by the -1 s AD regression prediction (noted as AD(-1s)) times a 1.7 MD/AD value (representing the 10th percentile in the MD/AD dataset; Figure 4.10). These criteria allow for lower than average "complete" displacements with an also below-average upper tail variability (indicated by MD/AD). Figure 4.12 shows the MD values above the threshold values as solid blue circles and the MD values below the threshold as open blue circles. Of the 60 events, 15 are interpreted as incomplete based on these criteria. These events span a range of magnitudes from M_W 4.9 to M_W 7.6 and represent a range of tectonic environments from low seismicity areas (e.g., Le Teil, France) to active deforming areas (e.g., Kern County, California). For reference, we also show in a gray dash-dot line a threshold based on the $\overline{D}$(-1s) regression line and the minimum 1.7 MD/AD value. Adopting this as the main threshold criterion line would have added one additional earthquake to the "incomplete" category, but overall the results using this alternative average displacement relation are similar.

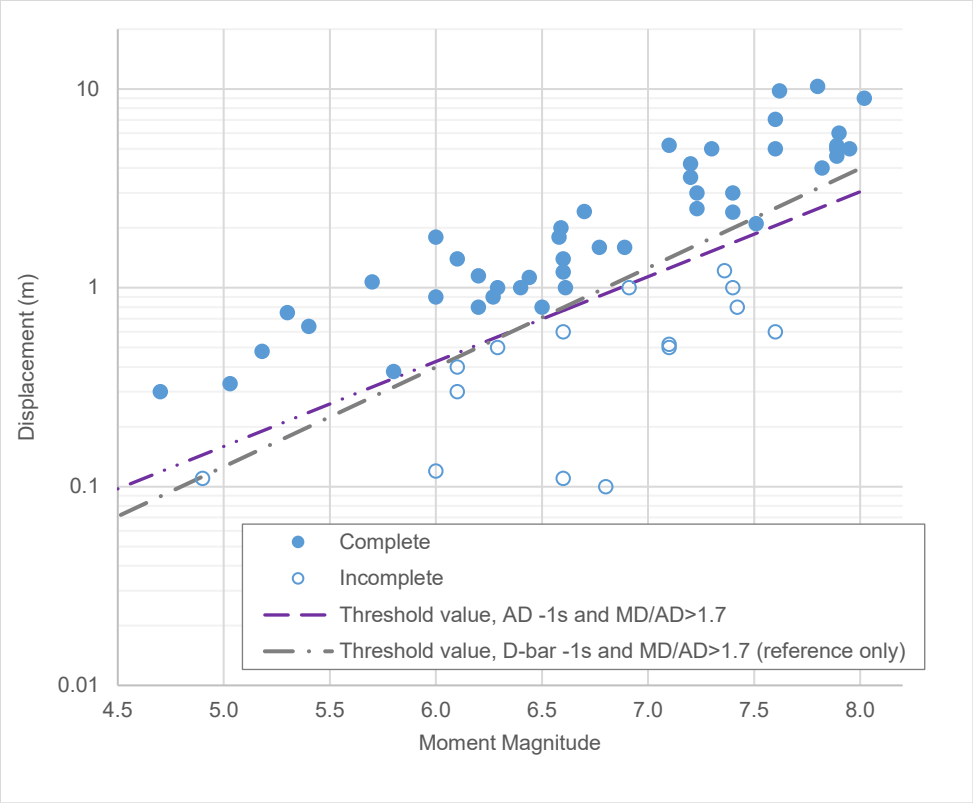

Figure 4.12. MD data and interpretations of complete (solid circle) or incomplete (open circle) reverse and reverse-oblique ruptures based on the AD(-1s) and MD/AD>1.7 criteria line (in purple). For reference, a similar threshold line derived from the scaling-based D-bar(-1s) relation is shown in gray.

Of the 15 earthquake ruptures that are classified as incomplete based on analysis of their MD values, three have estimated values of AD that are used in the AD regression. These three earthquakes are the 1952 Kern County, California, 1975 Lice, Turkey, and 2019 Le Teil, France events. The Kern County and Le Teil earthquakes had the highest absolute residuals in the analysis of $\log_{10}$AD vs M_W (Figure 4-5), and the Lice earthquake was one of two events with a suspiciously low value of MD/AD (Figure 4-6). In the case of the Le Teil earthquake, the AD and MD values are from very precise measurements of surface rupture by Ritz et al. (2020), so the displacement values are well constrained and documented (Sarmiento et al., 2021). Importantly, Ritz et al. (2020) show greater amounts of vertical deformation distributed over a broad (10s to 100s of meters wide) zone in the hanging wall based on differential InSAR analysis. If the broad aperture folding plus fault deformation are considered, the MD_V for this event is 0.23 m and the AD_V is closer to 0.12 m. These values would be more aligned with a complete earthquake rupture. This finding indicates that at least some of the events interpreted as having incomplete surface-fault ruptures may have total vertical displacements that scale with "complete" ruptures, but a significant fraction of the total vertical deformation is distributed as broader folding rather than as localized surface-fault rupture.

Given the classification of the Kern County, Lice, and Le Teil earthquake ruptures as incomplete, we re-run the least-squares linear regression analysis of $\log_{10}$AD vs M_W with these

events removed from the empirical dataset. Figure 4.13 shows the revised AD regression line based on the 29 earthquakes with estimated AD and interpreted as having complete ruptures. The new regression has intercept, slope, and regression standard error values of $a = -2.87, b = 0.416, s = 0.13$. Also shown in Figure 4.13 are the median regression line using all 32 AD records and the scale-based median D-bar line. The plot shows strong similarity to the initial AD regression, with the main differences being a slight lowering of the slope and a reduction in the regression standard error.

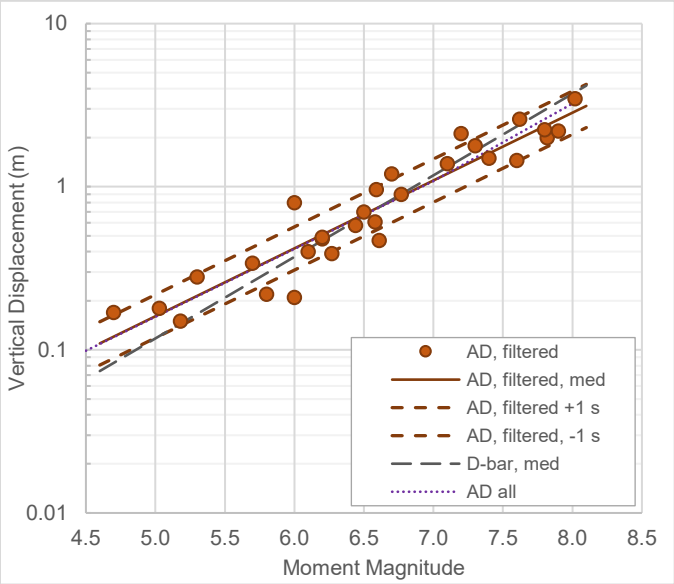

Figure 4.13. Revised Vertical AD vs MW data and regression results. For comparison are the initial AD regression line (purple dotted) and the scaling-based D-bar line (gray dashed).

The filetered dataset of 29 "complete" earthquakes with AD and MD were used to re-evaluate the MD/AD values. The updated median and 10th percentile values of MD/AD are unchanged (2.3 and 1.7, respectively), although the 90th percentile value increased from 3.7 to 3.9. Applying the same threshold criteria for a "complete" vs "incomplete" MD rupture using the same threshold criteria (-1 s AD and MD/AD = 1.7) using the revised AD regression identifies three additional events with MD values defined as "incomplete": The 1998 Iwate (Inland), Japan, the 1929 Baghan, Iran, and the 2002 Avaj, Iran earthquakes. The final MD dataset of complete ruptures therefore has N = 42 events, with N = 18 events classified as "incomplete". Although the Iwate and Avaj earthquakes include estimates of AD, we decided to not perform another iteration of the $\log_{10}$AD - M_W regression with these additional events removed.

Table 4.3 lists the events in order of the ratio between the MD value and the -1s AD value predicted based on the final $\log_{10}$AD - M_W regression. The MD/AD(-1s) threshold of 1.7 is indicated by the thick line and rows with text noting the change from "complete" to "incomplete" ruptures.

Table 4.3. Earthquakes in the database in order from highest to lowest ratio between measured MD and predicted AD (-1s).

Number	Date	Event	Location	M_W	AD, m	MD, m	Ratio, MD / predicted AD,-1s
48	9/21/1999	Chi-Chi	Taiwan	7.62	2.6	9.8	6.73
58	11/13/2016	Kaikoura	New Zealand	7.8	2.2	10.3	5.96
55	10/15/2013	Bohol	Philippines	7.1	1.4	5.2	5.90
43	12/25/1989	Ungava	Canada	6.0	0.80	1.8	5.84
51	10/8/2005	Kashmir	Pakistan	7.6	1.5	7.1	4.94
59	11/8/2018	Lake Muir	Australia	5.3	0.28	0.75	4.76
32	10/10/1980	El Asnam	Algeria	7.3	1.8	5.0	4.67
37	3/30/1986	Marryat Creek	Australia	5.7	0.34	1.1	4.63
45	8/19/1992	Suusamyr	Kyrgyzstan	7.2		4.2	4.32
5	1/3/1911	Chon Kemin	Kyrgyzstan	8.02	3.5	9.0	4.22
31	6/2/1979	Cadoux	Australia	6.1	0.4	1.4	4.13
15	1/13/1945	Mikawa-Fukozu	Japan	6.7	1.2	2.4	4.01
2	08/31/1896	Rikuu	Japan	7.2	2.1	3.6	3.70
35	6/11/1983	Coalinga aftershock - Nuñez	California, USA	5.4		0.64	3.69
22	10/14/1968	Meckering	Australia	6.59	0.96	2.0	3.69
9	5/6/1930	Salmas	Iran	7.6		5.0	3.50
54	3/23/2012	Pukatja	Australia	5.18	0.15	0.48	3.41
52	10/10/2007	Katanning	Australia	4.7	0.17	0.30	3.38
40	1/22/1988	Tennant Creek (LSE)	Australia	6.58	0.61	1.8	3.35
53	5/12/2008	Wenchuan	China	7.9	2.2	6.0	3.15
56	11/22/2014	Nagano	Japan	6.2	0.48	1.2	3.08
13	4/21/1935	Tuntzhuchio	Taiwan	7.23		3.0	3.00
57	5/20/2016	Petermann	Australia	6.0	0.25	0.90	2.92
8	6/17/1929	White Creek	New Zealand	7.89		5.2	2.76
25	3/10/1970	Calingiri	Australia	5.03	0.18	0.33	2.71
16	3/17/1947	Dari	China	7.89		5.0	2.65
18	2/12/1953	Torud	Iran	6.6		1.4	2.56
30	9/16/1978	Tabas	Iran	7.4	1.5	3.0	2.55
3	12/23/1906	Manas	China	7.95		5.0	2.50
4	1/23/1909	Silakhar	Iran	7.23		2.5	2.50
41	12/7/1988	Spitak	Armenia	6.77	0.90	1.6	2.48
12	11/28/1933	Behabad	Iran	6.29		1.0	2.46
10	2/2/1931	Hawkes Bay	New Zealand	7.89		4.6	2.44
39	1/22/1988	Tennant Creek (LSW)	Australia	6.44	0.58	1.1	2.40
11	12/25/1932	Changma	China	7.82	2.0	4.0	2.27
38	1/22/1988	Tennant Creek (Kunayungku)	Australia	6.27	0.39	0.90	2.25
36	8/23/1985	Wuqai	China	6.89		1.6	2.21

Number	Date	Event	Location	M_W	AD, m	MD, m	Ratio, MD / predicted AD,-1s
50	2/22/2005	Zarand	Iran	6.4		1.0	2.21
24	10/1/1969	Pariahuanca	Peru	6.6		1.2	2.19
46	9/29/1993	Killari-Latur	India	6.2	0.49	0.80	2.14
1	05/08/1847	Zenkoji	Japan	7.4		2.4	2.04
26	2/9/1971	San Fernando	California, USA	6.61	0.47	1.0	1.81
Complete ruptures (above)							
Incomplete ruptures (below)							
49	6/22/2002	Avaj	Iran	6.5	0.70	0.80	1.61
7	5/1/1929	Baghan	Iran	7.51		2.1	1.60
47	9/3/1998	Iwate (Inland)	Japan	5.8	0.22	0.38	1.49
19	12/13/1957	Farsinaj	Iran	6.91		1.0	1.36
6	4/18/1911	Raver	Iran	6.29		0.50	1.23
23	7/24/1969	Pariahuanca	Peru	6.1		0.40	1.18
28	9/6/1975	Lice	Turkey	6.6	0.50	0.60	1.10
17	7/21/1952	Kern County	California, USA	7.36	0.42	1.2	1.08
60	11/11/2019	Le Teil	France	4.9	0.05	0.11	1.02
29	1/1/1977	Mangya	China	6.1		0.30	0.88
44	6/20/1990	Rudbar-Tarom	Iran	7.4		1.0	0.85
20	9/1/1962	Ipak	Iran	7.42		0.80	0.67
21	5/24/1968	Inangahua	New Zealand	7.1		0.52	0.59
34	7/27/1981	Sirch	Iran	7.1		0.50	0.57
14	1/15/1944	San Juan	Argentina	7.6		0.60	0.42
42	10/29/1989	Chenoua	Algeria	6.0		0.12	0.39
33	6/11/1981	Golbaf	Iran	6.6		0.11	0.20
27	4/10/1972	Qir	Iran	6.8		0.10	0.15

4.2.5 MD VS MAGNITUDE SCALING

A plot of the MD data with three sets of linear regression lines is in Figure 4.14. Ruptures interpreted as complete are shown in solid circles; incomplete ruptures are open circles. A least-squares linear regression of $\log_{10}$MD – M_W based on the N = 42 complete ruptures yields intercept, slope, and regression standard error values of $a = -2.50, b = 0.415, s = 0.15$. This regression has an $R^2 = 0.87$. The median MD line is shown in Figure 4-10 as a solid line, with the ± 1 s values shown as dotted lines. A least-squares linear regression using the N = 18 incomplete ruptures yields values of $a = -2.71, b = 0.354, s = 0.30$, with an $R^2 = 0.42$. Although this R^2 value is low, we consider this relation to be useful to represent epistemic uncertainty for surface displacement hazard for some reverse faults, particularly in cases where distributed surface folding is more expected. If the incomplete rupture regression parameters are used, we recommend that practitioners account for the "remaining" deformation, at least qualitatively (e.g., expected distributed deformation over a hanging-wall fold). Also, a least-squares linear regression for the entire 60 events with estimated MD yields values of $a =$

$-2.73, b = 0.422, s = 0.35$, with an R^2 of 0.50. Whereas we present these results for completeness, our guidance would be to not use this in a logic tree, but rather consider weighted combinations of the complete and incomplete models.

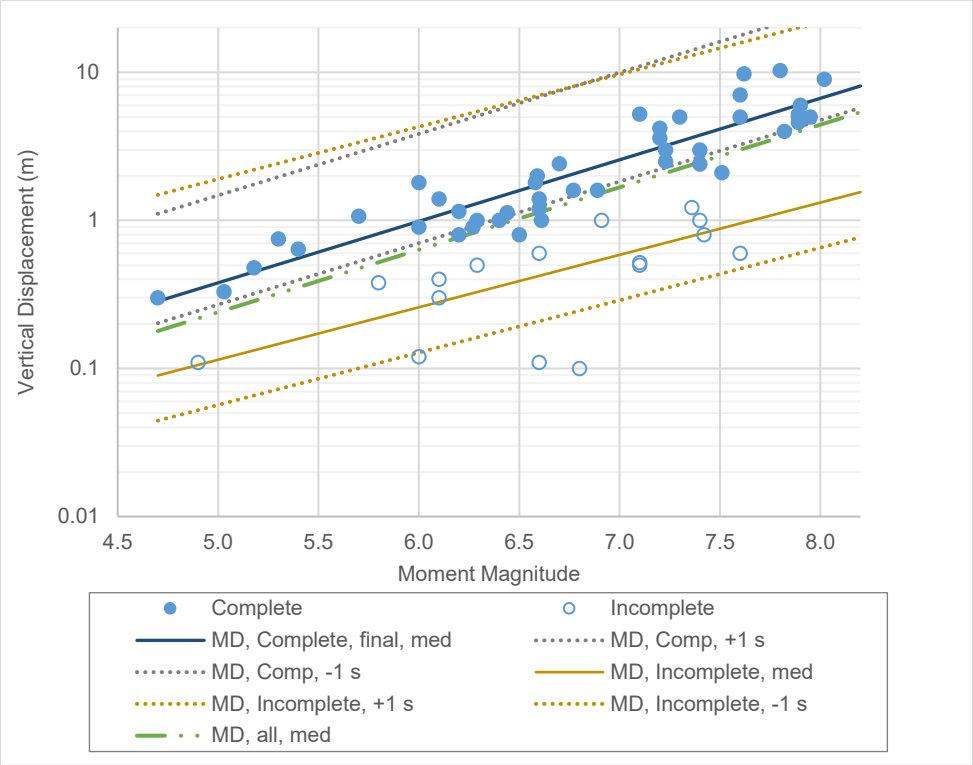

Figure 4.14. Vertical MD vs MW showing final interpretation of complete ruptures (solid circles; N = 42) and incomplete ruptures (open circles; N = 18). Least-squares linear regression lines for complete ruptures shown in dark gray (solid for median; dotted for ± 1s). Least-squares linear regression lines for incomplete ruptures shown in gold (solid for median; dotted for ± 1s). The median least-squares linear regression line fit to the whole MD dataset shown in green dash-dot-dot pattern.

Table 4.4 summarizes the recommended regression parameters for reverse and reverse-oblique earthquakes based on our evaluation. Note we provide precise results for the regression *a*, *b*, and *s* parameters, and also provide recommended values that include rounding and increases in *s*. The increases in *s* in particular are important to consider as displacement-magnitude regressions have been shown to be highly dependent on the dataset (e.g., Wells and Coppersmith, 1994; Moss and Ross, 2011; Wesnousky, 2008) and it is desirable that uncertainties applied to these models capture changes to regressions based on future events. Further reduction of uncertainties in the future can be based on larger and/or better filtered datasets. We note the values of *s* calculated from earlier studies (e.g., Wells and Coppersmith, 1994) were on the order of 0.3 to 0.4 and this analysis suggests they have been appropriately reduced based on additional data.

Table 4.4. Recommended parameter values for log-linear relations between vertical AD or vertical MD and moment magnitude for reverse and reverse-oblique surface-fault ruptures. Regression parameters and R^2 values at higher decimal places shown in parentheses. Parameters are for the form $\log_{10}(D) = a + bm$, with standard error of the regression s.

Name	AD or MD	a	b	s	R^2	s, recommended	Notes
Empirical AD, complete only (n=29)	AD	-2.87	0.416	0.133	0.89	0.2	Recommend for estimating AD assuming complete ruptures
Empirical AD, all data (n=32)	AD	-2.98	0.427	0.181	0.83	0.25	Alternative AD regression parameters to consider; captures all reverse ruptures
Empirical MD, complete only (n=42)	MD	-2.50	0.415	0.148	0.87	0.2	Recommend for estimating MD assuming complete ruptures; epistemic alternative
Empirical MD, incomplete only (n=18)	MD	-2.71	0.354	0.305	0.42	0.35	Recommend for estimating MD assuming incomplete ruptures; epistemic alternative
Empirical MD, all data (n=60)	MD	-2.73	0.422	0.354	0.50	n/a	Provided for completeness; do not recommend use for hazard.

4.2.6 DISCUSSION

The updated database of reverse and reverse-oblique surface-fault ruptures represents a significant improvement in data quality and completeness over previous compilations largely thanks to the SURE 1.0 and FDHI database efforts. The methodology used here to filter the data and classify events as "complete" or "incomplete" is one of many potential approaches to apply for developing useful models for displacement hazard. Other potential methodological choices, such as employing alternative methods for estimating AD from the rupture dataset, using orthogonal regression, or regressing displacements against surface rupture length, may be applied as well to yield epistemic alternative equations useful for hazard assessment. The choices we have made largely reflect our preference for simple models that build directly on previous efforts. In this regard, Figure 4.15 shows plots comparing median models of AD vs M_W (panel a) and MD vs M_W (panel b) developed from this study to other models compiled from the literature. All can be expressed in the form provided in equation (4.2), and the a, b, and s regression parameters are listed in Table 4.5. Interestingly, the result of this analysis for vertical AD (median model) is very similar to the empirical $\log_{10}AD - M_W$ regression parameters determined by Hecker et al. (2013) based on data from all rupture types compiled by Wesnousky (2008). Also of note are the steep slopes of the Wells and Coppersmith (1994) empirical displacement relations (based on all slip types; 0.69 for AD and 0.82 for MD) compared to the other empirical relations (0.32 to 0.51).

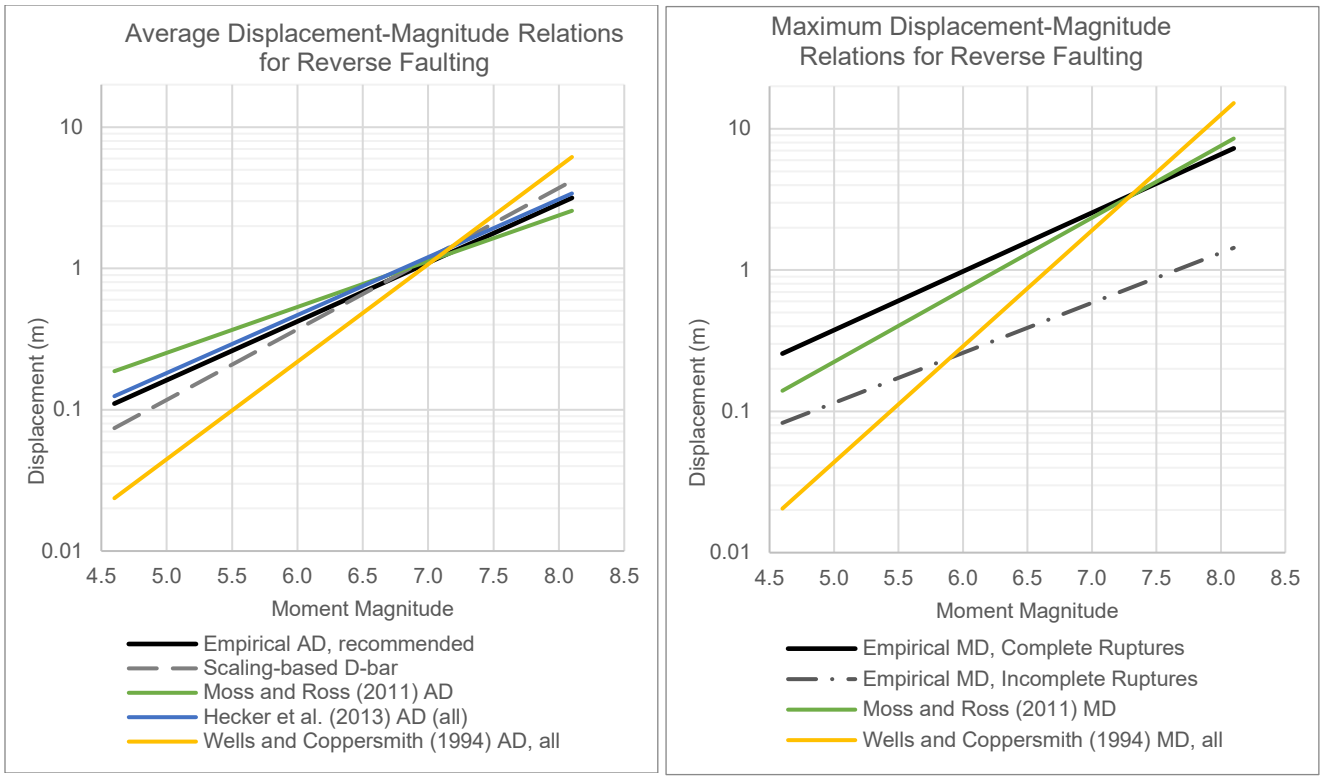

Figure 4.15. Comparison of empirical log-linear relations between AD (panel a) or MD (panel b) and moment magnitude applicable to reverse or reverse-oblique faulting.

Table 4.5. AD and MD Regression Parameters for the form $Log_{10}D = a + b\mathbf{M} + s\varphi$

Model, R and RO data unless specified	*AD* or *MD*	*a*	*b*	s	N	R^2
Theoretical (this study)	AD	-3.43	0.5	n/a	n/a	n/a
Complete ruptures (this study)	AD	-2.87	0.416	0.133	29	0.89
All ruptures (this study)	AD	-2.98	0.427	0.181	32	0.83
MR11	AD	-2.2192	0.3244	0.17		0.62
WC94, R data only	*AD*	*-0.74*	*0.08*	*0.38*	*15*	*0.01*
WC94, All slip types	AD	-4.80	0.69	0.36	56	0.56
HEA13, All slip types	AD	-2.79	0.41	0.33	W08	n/a
Complete ruptures (this study)	MD	-2.50	0.415	0.148	42	0.87
Incomplete ruptures (this study)	MD	-2.71	0.354	0.305	18	0.42
All ruptures (this study)	MD	-2.73	0.422	0.354	60	0.50
MR11	MD	-3.1971	0.5102	0.31	55	0.53
WC94, R data only	*MD*	*-1.84*	*0.29*	*0.42*	*21*	*0.13*
WC94, All slip types	MD	-5.46	0.82	0.42	56	0.61

Note: MR11 = Moss and Ross (2011); WC94 = Wells and Coppersmith (1994); HEA13 = Hecker et al. (2013); W08 = Wesnousky (2008). The WC94 Reverse (R) data only regression parameters were interpreted to be not significant and are shown in italics.

The implementation of alternative AD or MD models in hazard should be guided by project objectives, design criteria, available information about the fault posing the hazard, and the approach to risk and engineering decision making adopted by the project owner and/or other stakeholders. The filtered models we developed for complete ruptures are intended to better represent cases for surface-fault rupture from faults with a clear, repeated history of surface faulting. Although the median displacement for the "complete" rupture case is higher than for the "all" data regression (Figure 4.10), the lower standard error of the complete rupture regression results in lower displacement estimates at the 84th and higher percentiles compared to the "all" data regression. Because a lot of the higher standard error in the "all" data regression is due to lower displacement events (those we interpret as incomplete), the consequence to hazard is unrealistically high displacement values at higher statistical percentiles that are often considered in hazard studies.

With regards to incorporating the possibility for an incomplete rupture in a hazard analysis, this decision should be based on an assessment of the fault in question and the project parameters. If additional conservatism is desired and/or a geologic assessment of the subject fault suggests it is likely to generate complete ruptures, then the complete rupture regression may be given full weight in a hazard analysis. If, on the other hand, a mean-centered hazard is desired, and/or there

is no compelling case for asserting a fault will not produce an “incomplete” rupture, then capturing epistemic uncertainty by weighting complete and incomplete rupture regression parameters is warranted. As a starting point for assigning weights, we suggest utilizing the ratio of complete to incomplete ruptures in the dataset as a proxy for the site-specific probability of a particular fault generating a complete vs incomplete rupture. In this case, the complete rupture regression would receive a weight of ($^{42}/_{60}$ =) 0.7 and the incomplete rupture regression would receive a weight of ($^{18}/_{60}$ =) 0.3. Separating the ruptures into epistemic alternatives for complete vs incomplete ruptures has the advantage over the “all” regression parameters of capturing the observed rupture behavior of the empirical dataset, while not penalizing the model with an overly high standard error that would result in unrealistically high average or maximum displacements at high probability levels.

5 Probability of Distributed Displacement

Distributed displacements often require more effort to document in the field than primary displacements. And different mechanisms other than secondary displacement can contribute to the observations. In this study we look at two different databases to evaluate the probability of distributed displacement for reverse events: FDHI and SURE. To provide some basis for the observed results, an analytical solution was developed as a function of rupture mechanism.

5.1 ANALYTICAL ESTIMATES

An attempt was made to provide an analytical basis for the distance of displacements that can be observed. The assumptions are:

- Particulate mechanics controls the physics of surface-fault rupture,
- Local stress fields are the same as regional stress fields,
- The example, which is derived for a dip of 60 degrees and a friction angle of 30 degrees, is reasonably representative.

We are only focusing on the physics of particulate mechanics and ignoring tectonic or structure controlled surface displacements for this example. The boundary that is often used to differentiate between rock and soil at the ground surface is 1500 m/s shear-wave velocity, which often indicates the limit of material that is "rippable" with heavy equipment. Material with a velocity less than this often behaves like a particulate; material with a shear-wave velocity greater than 1500 m/s often behaves like a solid.

The stress conditions that result in the distributed displacements propagating in a particulate material are different dependent upon if the stress regime is compressional or extensional. Using a linear failure criteria like Mohr-Coulomb, we can map the stresses into Mohr space (normal stress and shear stress) and visualize the initial stress conditions and failure stress conditions that result in particle dislocation, rupture propagation, and displacement that occurs away from fault strike. This particle dislocation produces planes of weakness that coalesce into a wedge type failure commonly evaluated in near surface conditions for civil works and construction purposes (Terzaghi, 1943) but used here to better understand propagation of distributed fault rupture deformations.

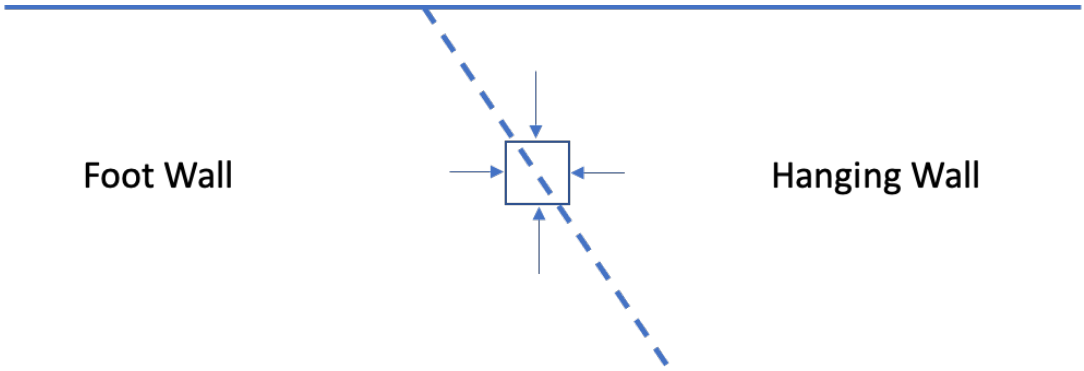

Figure 5.1. For dip-slip earthquakes we evaluate the stress conditions along primary fault rupture with respect to the hanging wall and footwall.

5.1.1 REVERSE MECHANISM

For reverse events the stress field is compressional. The compression will result in horizontal stresses exceeding vertical stress to the point where the stress circle touches the failure envelope defined by the friction angle. The failure plane is then equal to 45 minus half the friction angle as found by geometry.

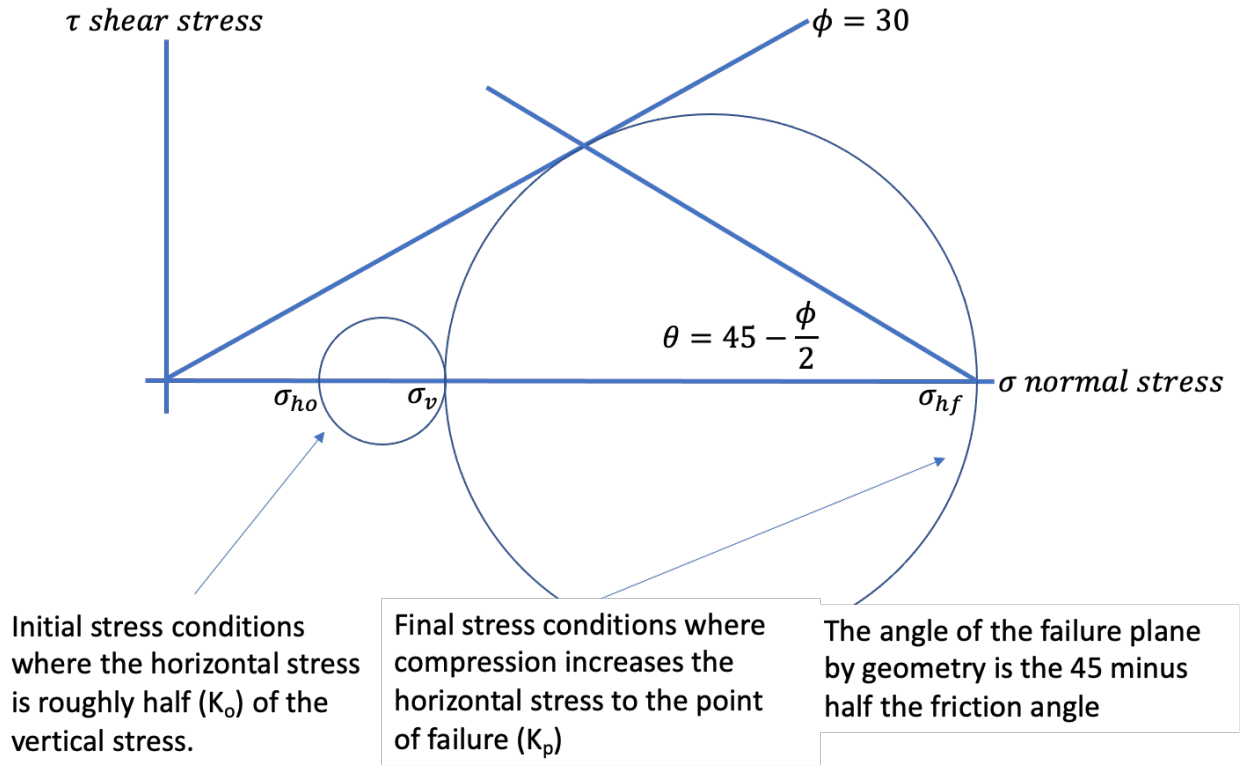

Figure 5.2. Mohr-Coulomb plot of the stress conditions that results in particulate failure when subjected to a compressional stress field.

The distance from strike (r) that the failure plane propagates is then a function of depth (z) of a failure wedge of a particulate material undergoing compression (Figure 5.3). Using a dip angle of 60 degrees we find that that distance can be defined geometrically as:

$$r = \frac{z\ csc(60)}{sin\left(45 - \frac{\phi}{2}\right)} \tag{5.1}$$

For a friction angle of 30 degrees, the distance $r = 2.31z$ or greater than two times the depth of the failure wedge. Equation (5.1) indicates that as the friction angle increases that the distance from strike increases for distributed displacements. As the dip angle decreases the distance increases. If we assume a sediment depth of 1 km (using a threshold of 1500 m/s) then the distance we would expect displacements to propagate from strike would be roughly 2.3 km. But on average material would get stronger with depth due to higher stress conditions and/or higher friction angles so we would expect displacements further than this.

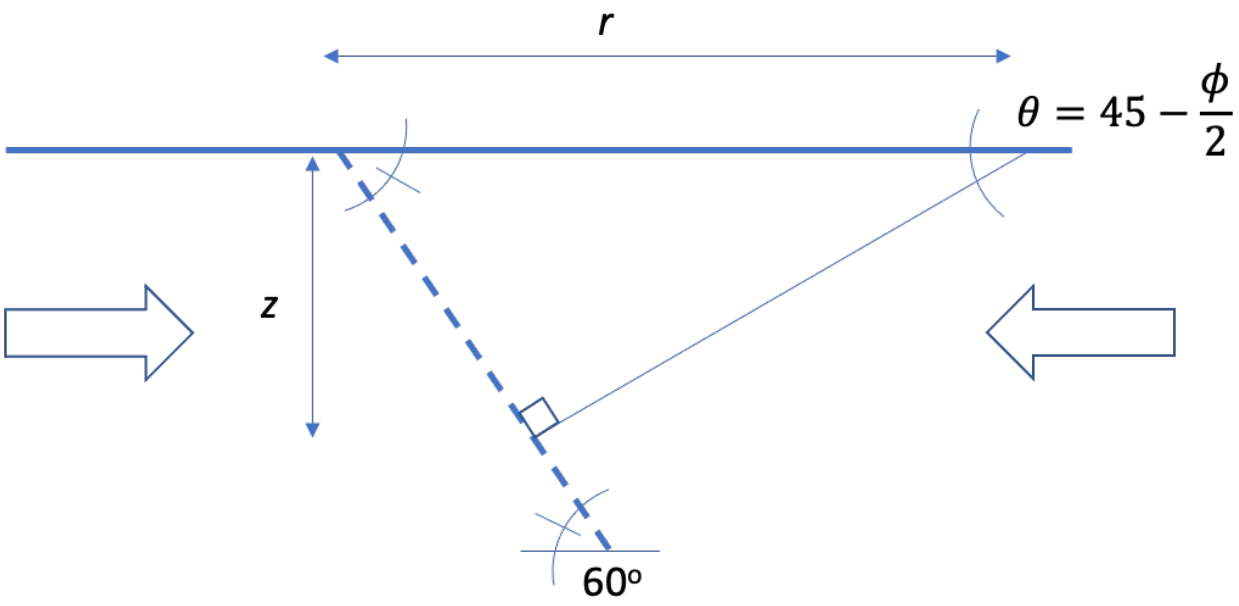

Figure 5.3. Passive wedge geometry in a compressional stress field.

When solving for the force required (Fig 5.4) to mobilize the wedge of soil (typically called a passive wedge) we find that:

$$P_p = \frac{1}{2}K_p\gamma z^2\ where\ K_p = \frac{\sigma_{hf}}{\sigma_v} = \frac{1 + sin\phi}{1 - sin\phi} = tan^2\left(45 + \frac{\phi}{2}\right) \tag{5.2}$$

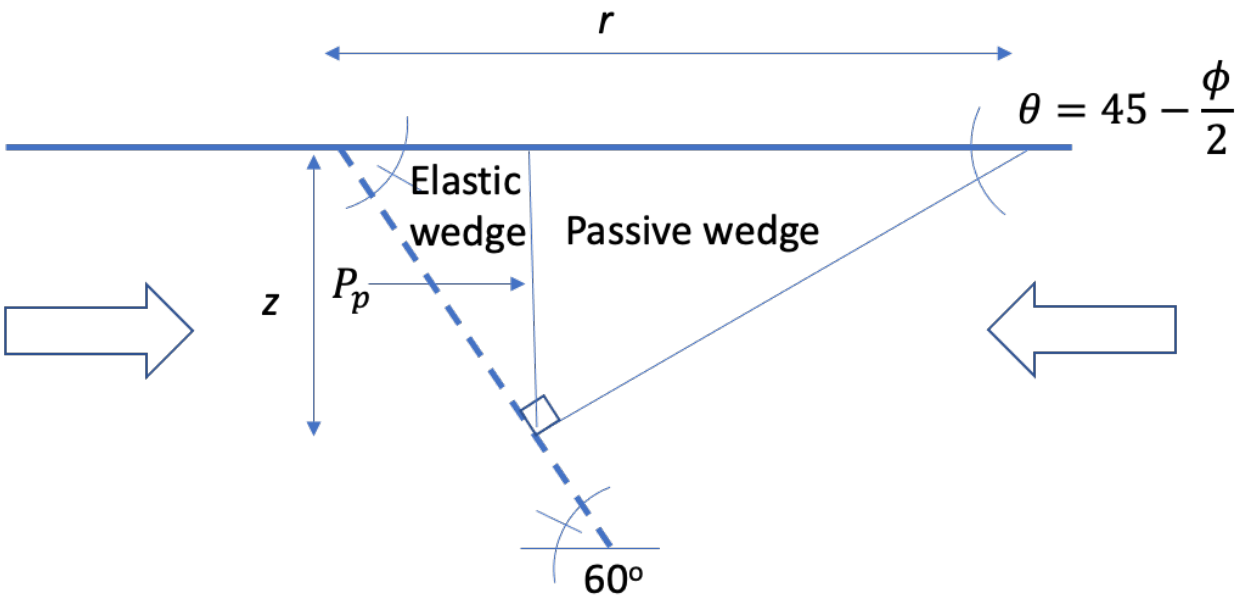

Figure 5.4. Solving for the force P_p required to mobilize the passive wedge to failure.

A linear failure surface from the Mohr-Coulomb assumption as we have used here, or a more realistic log-spiral failure surface (Carquot and Kerisel, 1948) can be used to model the propagation of distributed displacement. The log-spiral failure surface would result in slightly less distance from strike (r) than the linear failure assumption.

5.1.2 NORMAL MECHANISM

In normal earthquakes, where the stress field is extensional in nature, we see a different progression towards distributed displacements. Here the horizontal stress will decrease to the point where the stress circle touches the failure envelope resulting in a failure plane of 45 plus half the friction angle. The change from compressional to extensional in this problem only changes the sign in the denominator of Equation 5.1 from minus to plus:

$$r = \frac{z\ csc(60)}{sin\left(45 + \frac{\phi}{2}\right)} \tag{5.3}$$

Given a 30 degree friction angle and 60 degree dip, the distance $r = 1.33z$. For normal events, an increase in friction angle results in a decrease in the distance from strike we would expect to see distributed displacements. As in the reverse faulting mechanism case, a decrease in the dip angle results in an increase in distance. And with material strengthening with depth we would expect to see smaller distances from strike.

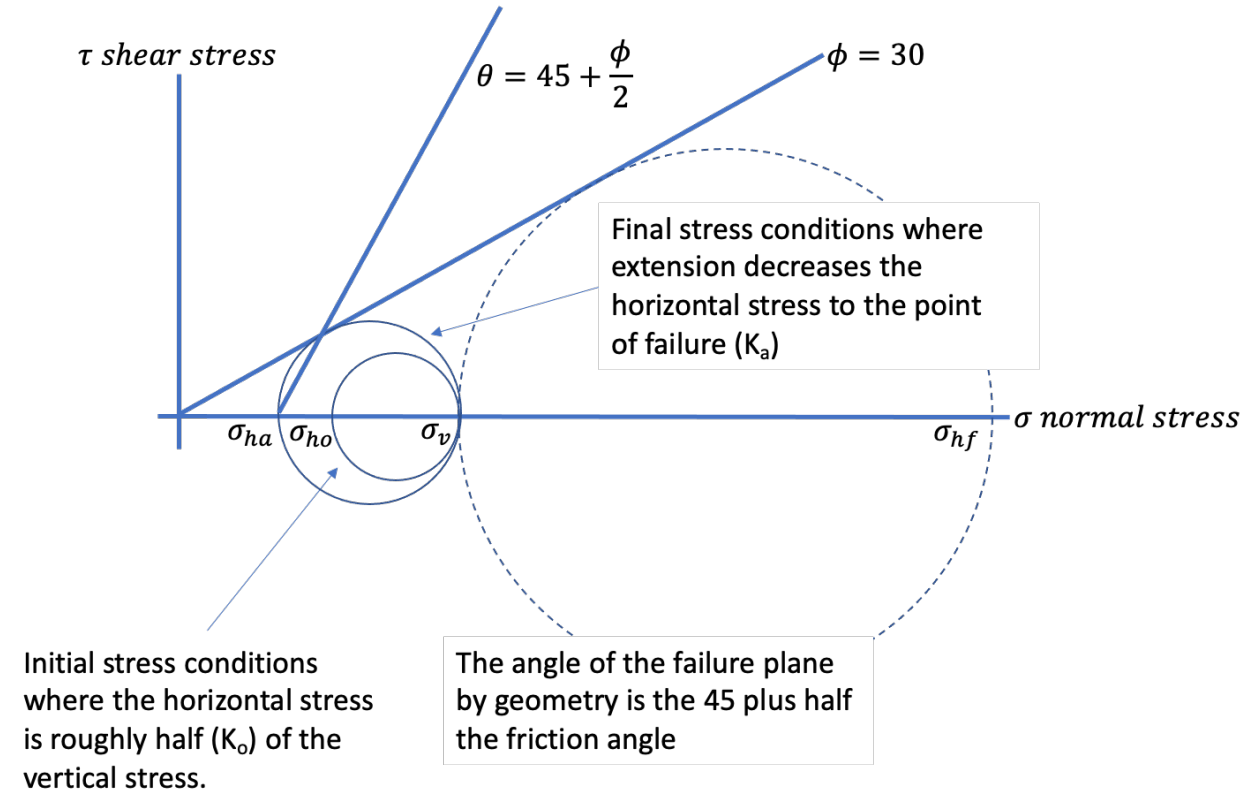

Figure 5.5. Mohr-Coulomb plot of the stress conditions that results in particulate failure when subjected to an extensional stress field.

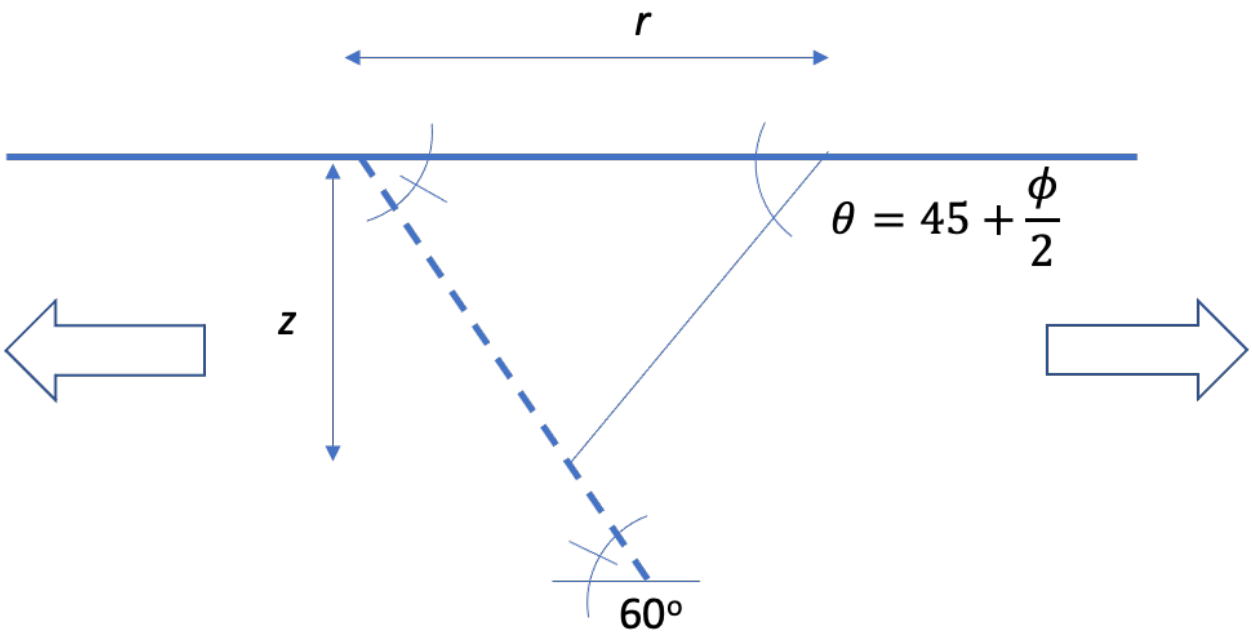

Figure 5.6. Active wedge geometry in an extensional stress field.

The wedge failure is now what is typically called and active wedge. The force required to mobilize the active wedge is:

$$P_a = \frac{1}{2} K_a \gamma z^2 \; where \; K_a = \frac{\sigma_{hf}}{\sigma_v} = \frac{1 - sin\phi}{1 + sin\phi} = tan^2\left(45 - \frac{\phi}{2}\right) \tag{5.4}$$

If we plug in some reasonable numbers and leave z as unknown, we find that there is roughly an order of magnitude more force required to mobilize the compressional (passive) failure versus the extensional (active) failure. If we relate proportionally the seismic moment (M_o) to the force required (P) then if a normal (extensional) event displays distributed displacements for a M_w 6 (M_o~10^{12} MN*m), a reverse (compressional) event would take just under a M_w 7 (M_o~ 10^{13} MN*m) to display the same distributed displacements.

5.1.3 STRIKE SLIP MECHANISM

Finally with strike slip events we tend to have near vertical fault planes. The stress conditions are quite different for strike-slip earthquakes in that only shear is being added and particulate will fail in a simple shear manner. The stress conditions are such that the horizontal and vertical stresses remain unchanged but shear stress is added until the failure envelope is reached.

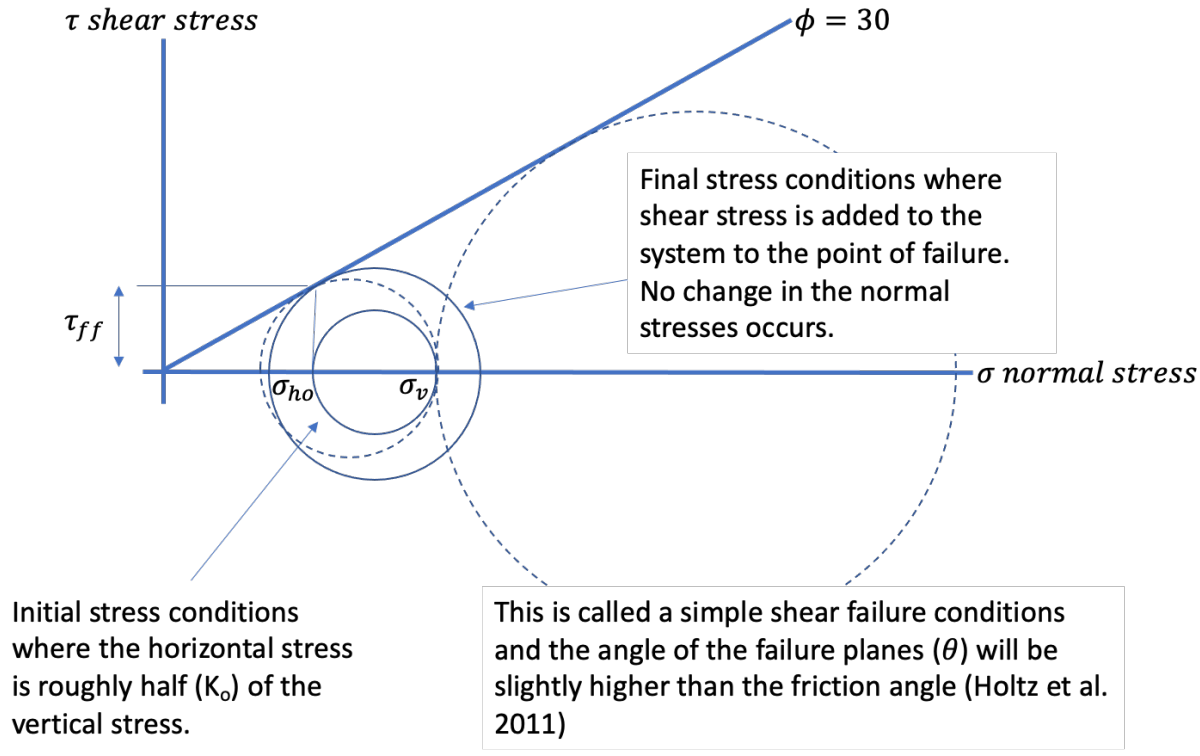

Figure 5.7. Mohr-Coulomb plot of the stress conditions that results in particulate failure when subjected to a pure shear stress field.

This type of failure mechanisms does not inherently result in distributed displacements, and it is thought that off-strike displacements are due to oblique stresses, asperities and bends in the fault, strain hardening behavior of the particulate forcing strains to migrate off the plane, or other mechanisms.

5.1.4 ANALYTICAL SUMMARY

In summary, a simple analytical approach considering particulate physics was used to compare how the distance of distributed displacement from strike can be considered a function of the fault rupture stress conditions and the fault rupture mechanism.

- The particulate mechanics indicate that reverse events will tend to propagate displacements 1.7 times greater than normal events for a friction angle of 30 degrees; friction angles of 20 and 40 degrees would suggest reverse:normal ratios of secondary displacement widths of about 1.4 to 2.1, with all else being equal.

- A decreasing dip angle will tend to propagate displacements further from strike for both normal and reverse.

- Changing material properties, i.e., friction angle, has the opposing effects depending on if the mechanism was reverse or normal.

- The force required to mobilize reverse failure wedges is an order of magnitude greater than the force required for normal failure wedges, which is roughly equal to 1 unit of moment magnitude. This translates to a significantly higher likelihood of observing normal fault distributed displacements than reverse all things being equal, which will be shown to be verified in the data.

- Strike-slip events are simple shear in nature and distributed displacements are likely a function of conditions that cause a deviation from that such as fault bends, fault steps, fault asperities, strain hardening material behavior, or other.

Some additional thoughts on the analytical exploration of distributed displacements:

- The dip angle of primary displacement in a particulate material will be controlled by the same physics which would lead to normal faults being steeper (45 plus half the friction angle) than reverse faults (45 minus half the friction angle) if all else is held equal.

- Some dip-slip fault planes have started out in a compressional stress field and evolved or transitioned to an extensional stress field. An example of this would be overthrust faults in the Montana Rockies that were once compressional and have transitioned in the current geologic era to extensional. Transitioning from compressional to extensional would result in a shallower predefined dip angle than would likely happen otherwise.

This would result in distributed displacements further away from strike than if it were not the case.

- Geologic structure in solid material will follow different physics such as a non-linear failure envelope like Hooke-Brown. This will result in steeper dip angles when rupturing through intact rock and steeper distributed displacement angles as well. However existing structure and existing fault planes will provide weaknesses and conduits for displacement that control the location and angle for primary and distributed displacements. The strain will find the easiest path to work its way to the ground surface.

5.2 STATISTICAL RESULTS

In prior studies of normal (Youngs et al., 2003) and strike slip (Petersen et al., 2011) earthquake displacement datasets, the approach to modeling the probability of distributed displacements was two-fold. The first step was to grid the fault region (e.g., 500 m grid squares), class the gridded data into yes or no observations, and then fit a logistic regression to this class data. The second step was to then to evaluate the amplitude of distributed displacements with distance from strike.

Here we are taking a slightly different approach. We evaluate distributed displacements in three steps;

1) The probability of nonzero displacement, P(d>0) using a 500m grid squares to observe the occurrence of distributed traces.
2) The frequency of displacements as a function of distance from primary fault strike, P(d>0).
3) The amplitude of distributed displacements with respect to maximum and average displacement, d/MD and d/AD.

Where applicable we have compared the FDHI data with the SURE 2.0 to provide confidence in the results. We evaluated the distributed data from several perspectives to determine if there was any dependence on magnitude, surface rupture length, or location along fault. Below in figure 5.8 is a plot of displacement as a function of x/L, and no relationship can be observed.

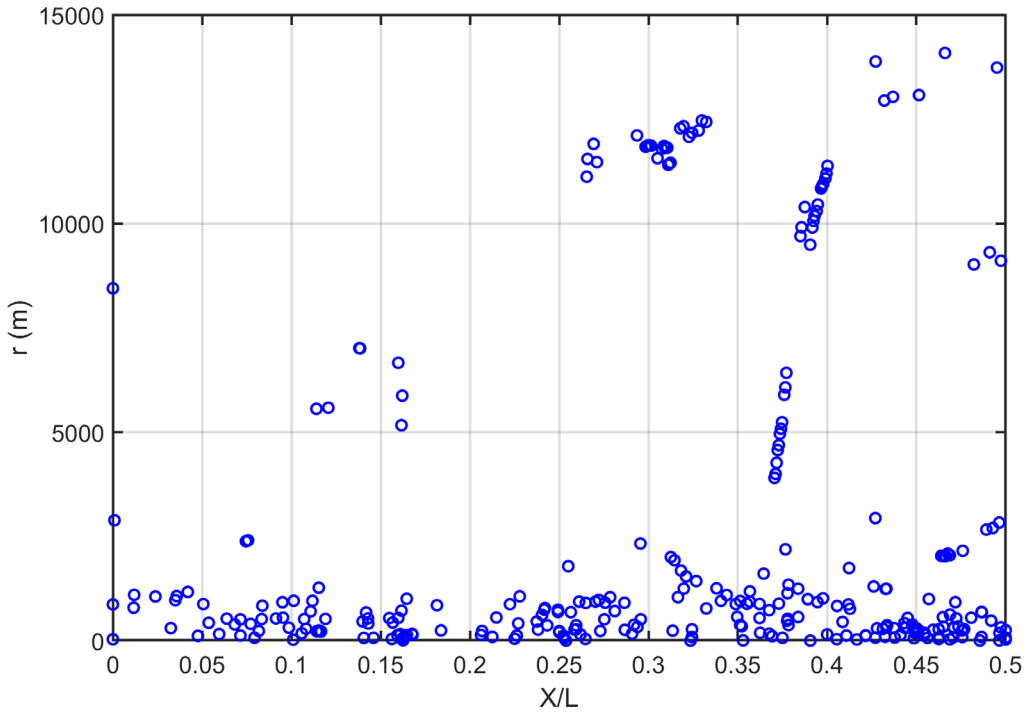

Figure 5.8. Plot of r versus x/L for all R/RO events in the FDHI database. The obvious string of data from x/L of 0.37 to 0.40 is from the Kaikoura event.

5.2.1 PROBABILTY OF NONZERO DISTRIBUTED DISPLACEMENT

To determine the probability of nonzero distributed displacement, P(d>0), all the reverse (RV) and reverse-oblique (RV-OBL) events from the FDHI database were used. A list of the 25 events found in the FDHI database is provided below. For validation this data was compared at times to the SURE 2.0 database.

Table 5.1. List of FDHI events used in this analysis.

	Event Name	Event Date	Mechanism	Mw	SRL (km)
1.	Wenchuan China	5/12/2008	RV-OBL	7.9	240
2.	ChiChi Taiwan	9/20/1999	RV-OBL	7.62	72
3.	Nagano Japan	11/22/2014	RV	6.2	8.5
4.	Kashmir Pakistan	10/8/2005	RV	7.6	70
5.	Kaikoura New Zealand	11/13/2016	RV-OBL	7.8	200
6.	San Fernando California	2/9/1971	RV	6.61	19
7.	Bohol Philippines	10/15/2013	RV	7.1	50
8.	Kern California	7/21/1952	RV	7.36	32
9.	Petermann Australia	5/20/2016	RV	6.0	16
10.	El Asnam Algeria	10/10/1980	RV	7.3	36
11.	Cadoux Australia	6/2/1979	RV	6.1	14
12.	Calingiri Australia	3/10/1970	RV	5.03	3.25
13.	Marryat Creek Australia	3/30/1986	RV	5.7	13

14. Meckering Australia	10/14/1968	RV	6.59	37
15. Pukatja Australia	3/23/2012	RV	5.18	1.25
16. TennantCreek1 Australia	1/22/1988	RV	6.27	15
17. TennantCreek2 Australia	1/22/1988	RV	6.44	8
18. TennantCreek3 Australia	1/22/1988	RV	6.58	8.25
19. Rikuu Japan	8/31/1896	RV	6.7	40
20. Mikawa Japan	1/12/1945	RV	6.6	7
21. IwateInland Japan	9/3/1998	RV	5.8	1.2
22. ChonKemin Kyrgyzstan	1/3/1911	RV	8.02	177
23. LeTeil France	11/11/2019	RV	4.9	5
24. Spitak Armenia	12/7/1988	RV-OBL	6.77	7.5
25. Killari India	9/29/1993	RV	6.2	0.25

A gridding approach was taken to evaluate the frequency of distributed displacements (d) in the hanging wall (HW) and footwall (FW). Each event was plotted using the coordinate system provided with the data and then a 500m by 500m cell grid was overlayed. The occurrence of distributed displacement traces were then marked if they fell within a 500m cell and the sum of these were then divided by the total number of cells at that grid spacing or distance (r) from the principle fault. Figure 5.9 shows and example of this approach for the San Fernando event. The red lines show principal traces, blue lines distributed traces, green circles the cell where HW traces were observed, and red x's where FW traces were observed. Appendix B shows each FDHI event with the grid and observed traces. This gridding approach was found to be more defensible compared to the 500m slice approach that was used in the first round of this research.

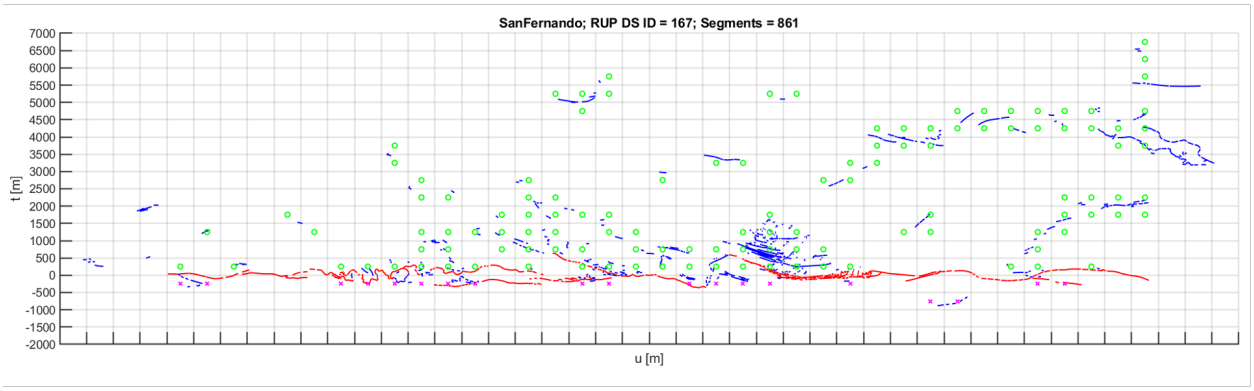

Figure 5.9. Gridded fault rupture (500m x 500m) showing principal and distributed surface fault rupture traces. The red lines show principal, blue lines distributed on the hanging wall, and green lines distributed on the footwall. Marked grid blocks were those counted toward occurrence.

The plotted data and the upper range as defined by the 95th percentile shown in figures 5.10 and 5.12. For the hanging wall (HW) side the following plots show for the entire data range, the 3 km range, and for additional percentiles of 85th and 50th percentile. Some observations; the FDHI and SURE2.0 databases are in good agreement providing confidence in the probability values, the 50th percentile drops off to zero around 1km distance, and that distributed displacements have been observed out to 22.5 km in some situations.

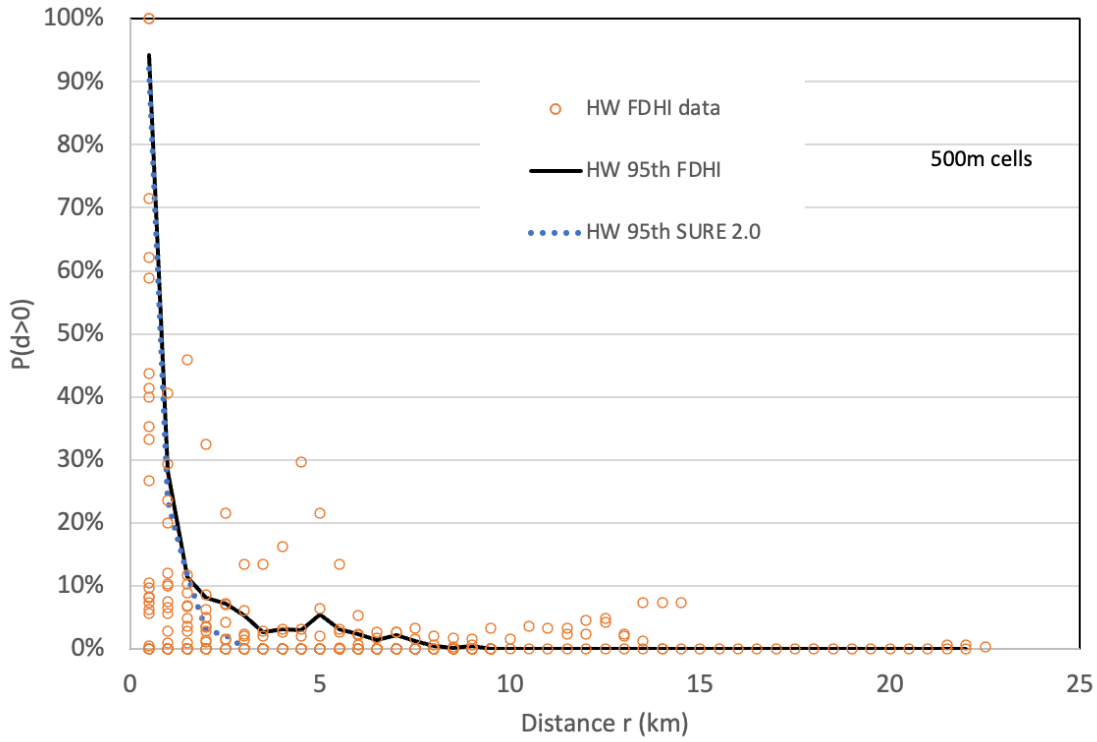

Figure 5.10. Distance versus probability of distributed surface fault rupture for hanging wall.

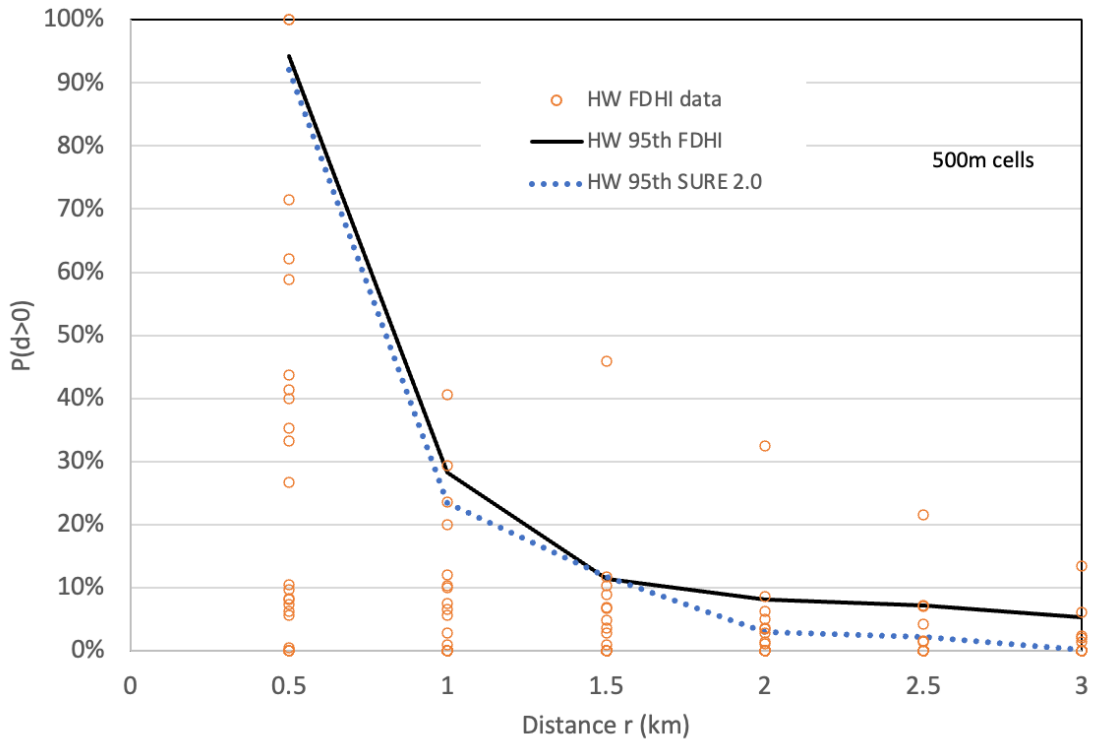

Figure 5.11. Distance versus probability of distributed surface fault rupture for hanging wall.

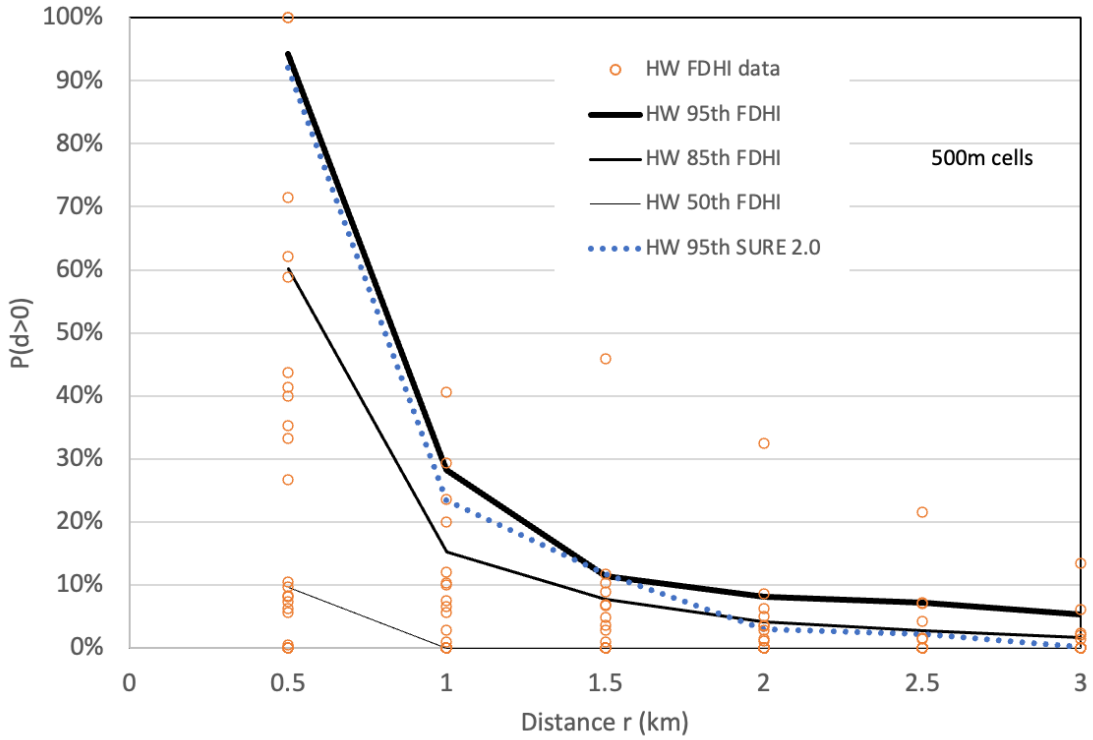

Figure 5.12. Distance versus probability of distributed surface fault rupture for hanging wall.

Examining further the data has been parsed by specific events to see if any one event or region is dominating the percentiles. Figure 5.13 shows event by event how the HW side is influenced by specific events compared to the 95th percentile. As can be seen the San Fernando event drives the upper bound across most of the range, with the small Killary and Pukatja events controlling the upper bound at 0.5 km distance. The latter two events are small magnitude small surface rupture events where the interpretation of primary versus secondary can be subjective and most of the displacements fall within one or two 500 m cells (see gridded events in the Appendix B).

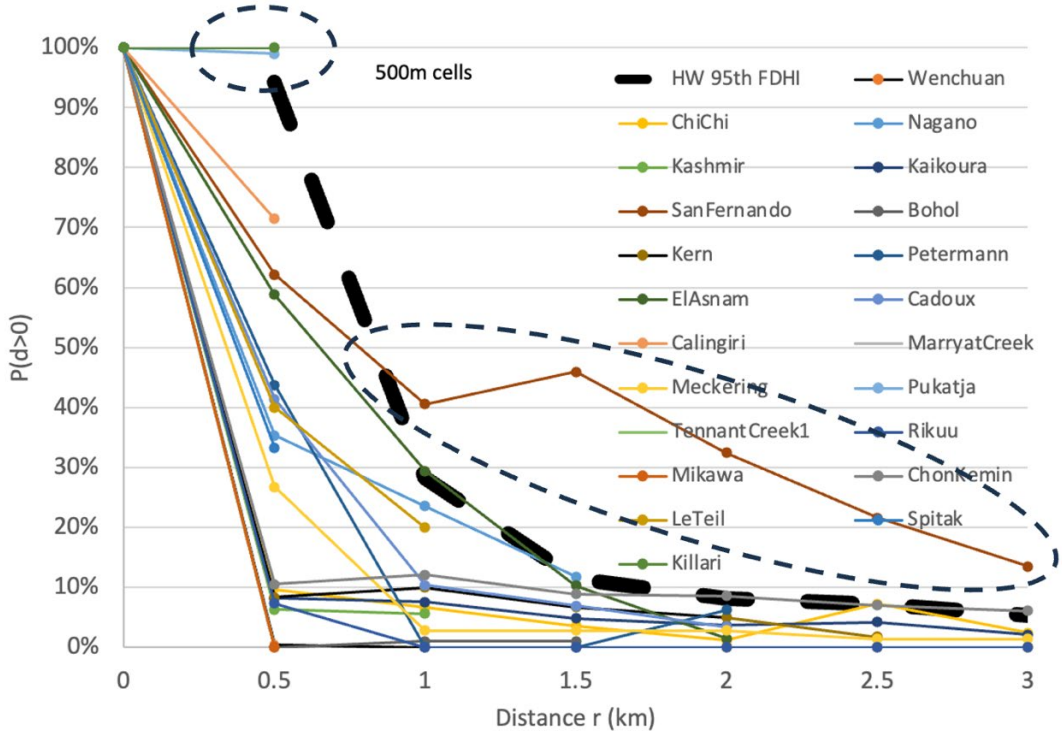

Figure 3.13. Examining occurrence of distributed surface fault rupture by event for hanging wall.

On the footwall (FW) side the same plots are shown (Figures 5.14 through 5.16). Some observations of the FW data; the FDHI and SURE2.0 data differ some in the 95th percentiles, the 50 percentile goes to zero at 1 km similar to HW, and distributed displacements have been observed out to 11km. The two small events of Killary and Pukatja again strongly influence the frequency at 0.5km, and Cadoux and TennentCreek2 events influence the upper bound across the 0.5 to 1.5km range. The difference between SURE2.0 and FDHI data has to do with how each database assigns hanging and foot wall designation with respect to principal fault designation.

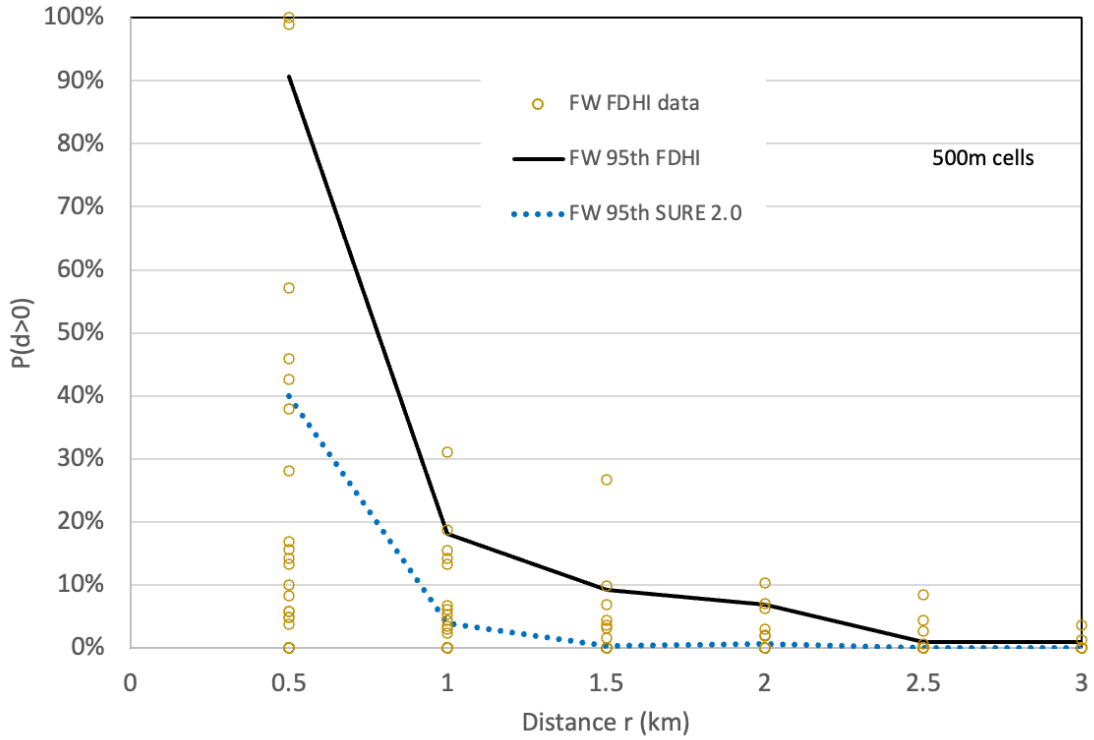

Figure 5.14. Distance versus probability of distributed surface fault rupture for footwall.

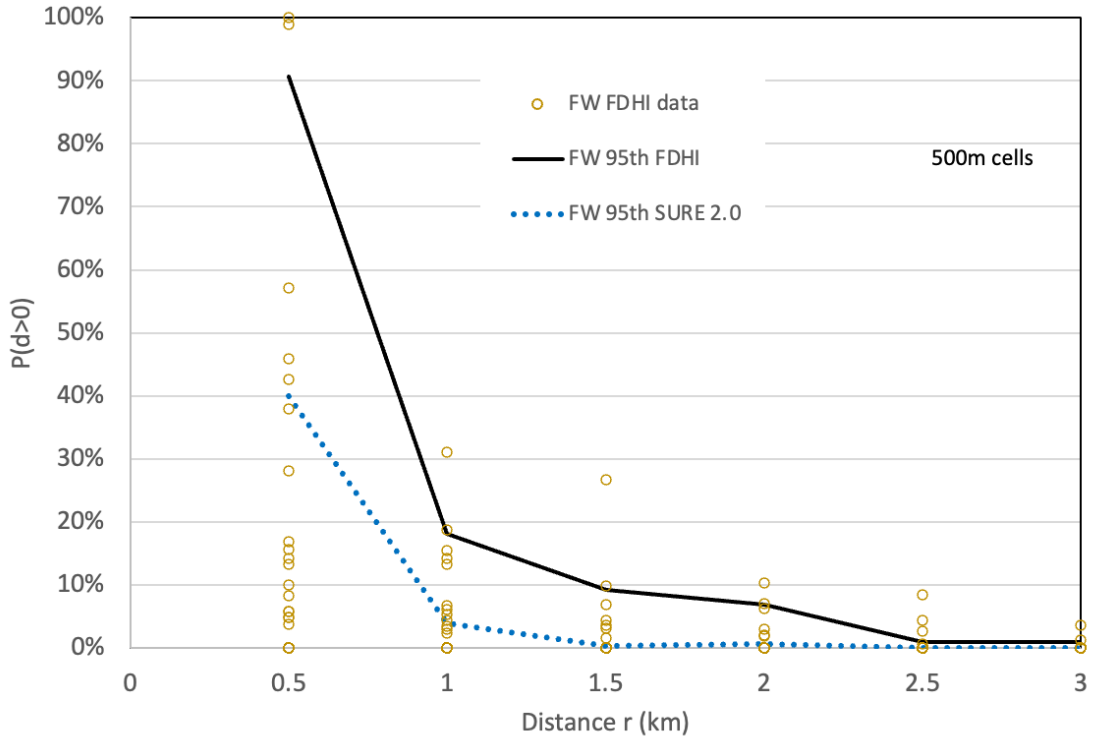

Figure 5.15. Distance versus probability of distributed surface fault rupture for footwall.

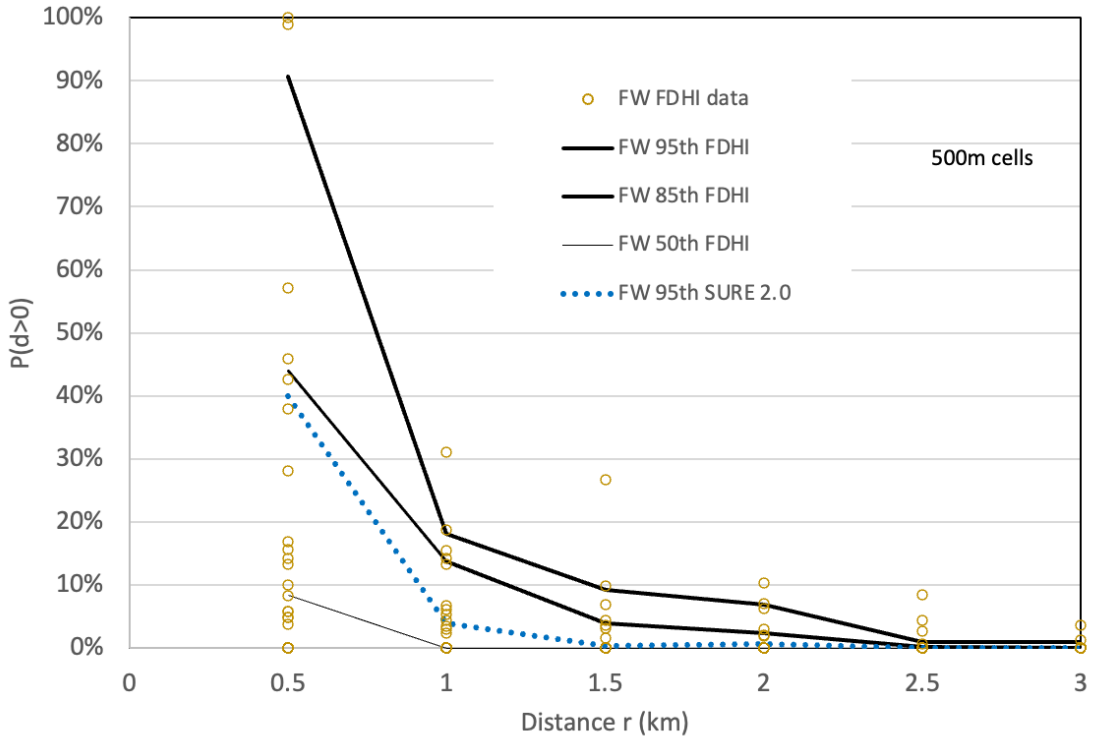

Figure 5.16. Distance versus probability of distributed surface fault rupture for footwall.

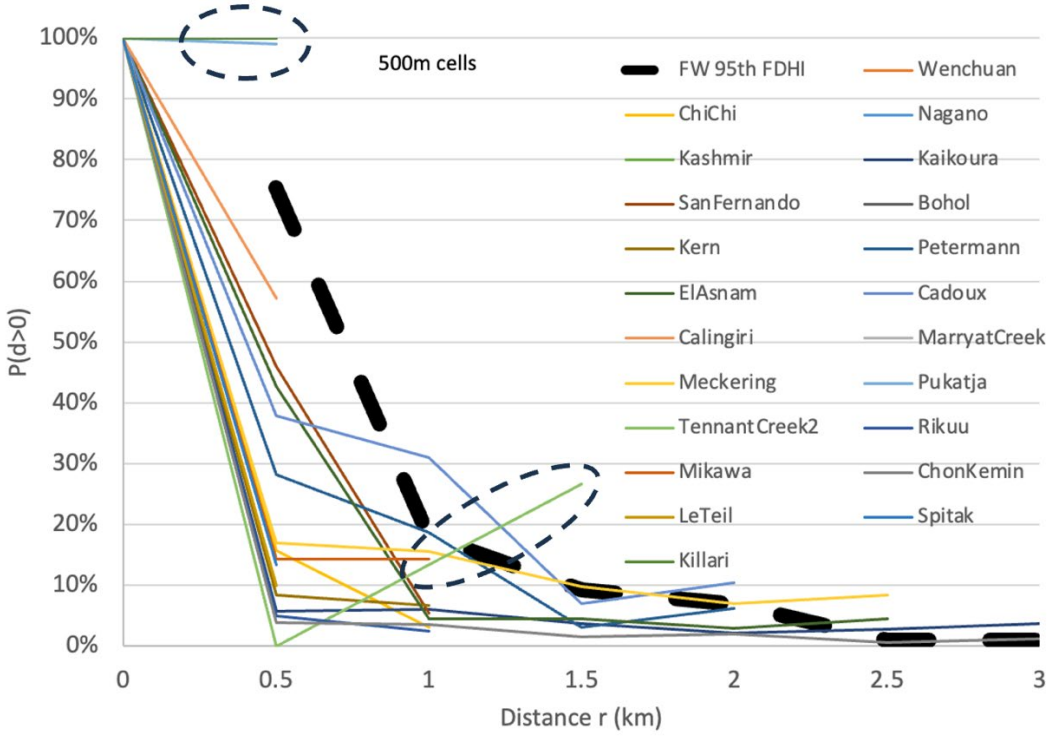

Figure 5.17. Examining occurrence of distributed surface fault rupture by event for footwall.

Tabular values of the percentiles are provided to allow users to define the threshold they are comfortable using in forward analysis. Although the 95th percentile goes to zero at specific distances, some projects may warrant using a nonzero value to account for complex faulting situations that can produce distributed displacements at long distance from principal faulting.

Table 5.2: Percentiles for Hanging Wall (HW) left, and Footwall (FW) right.

r (km)	95th	85th	50th
0.5	0.94286	0.60156	0.0964
1	0.28234	0.1526	0
1.5	0.11466	0.07708	0
2	0.0813	0.04184	0
2.5	0.07186	0.02698	0
3	0.05322	0.01694	0
3.5	0.0272	0	0
4	0.0309	0	0
4.5	0.02968	0	0
5	0.0552	0	0
5.5	0.0309	0	0
6	0.02382	0	0
6.5	0.01456	0	0
7	0.0216	0	0
7.5	0.01272	0	0
8	0.00512	0	0
8.5	0.00256	0	0
9	0.0048	0	0
9.5	0	0	0
10	0	0	0
10.5	0	0	0
11	0	0	0
11.5	0	0	0
12	0	0	0
12.5	0	0	0
13	0	0	0
13.5	0	0	0
14	0	0	0
14.5	0	0	0
15	0	0	0
15.5	0	0	0
16	0	0	0
16.5	0	0	0
17	0	0	0
17.5	0	0	0
18	0	0	0
18.5	0	0	0
19	0	0	0
19.5	0	0	0
20	0	0	0
20.5	0	0	0
21	0	0	0
21.5	0	0	0
22	0	0	0
22.5	0	0	0

r	95th	85th	50th
0.5	0.75428	0.4397	0.0833
1	0.18098	0.13714	0
1.5	0.09268	0.03948	0
2	0.06882	0.02448	0
2.5	0.01016	0.00256	0
3	0.01016	0	0
3.5	0.01272	0	0
4	0.00512	0	0
4.5	0.00256	0	0
5	0	0	0
5.5	0	0	0
6	0	0	0
6.5	0	0	0
7	0	0	0
7.5	0	0	0
8	0	0	0
8.5	0	0	0
9	0	0	0
9.5	0	0	0
10	0	0	0
10.5	0	0	0
11	0	0	0

Exponential curves were fit the 85th percentiles for ease of coding. The curves follow the function form below where r is the distance in km from the principal fault, a and b are coefficients as a function of hanging wall or footwall, and the probability value is capped at 1.0.

$$P(d > 0) = exp(-a * r + b) \leq 1.0 \quad (5.5)$$

Table 5.3. Coefficients for 85th percentile function for P(d>0).

coefficients	Hanging Wall	Footwall
a	2.2	2.4
b	0.5	0.4

If we examine this data for magnitude or surface rupture length dependence, we first look at the relationship between magnitude and surface rupture length for these 25 R/RO events. The best fit to the data in semi-log space compares to prior relationships such as Wells and Coppersmith (1994).

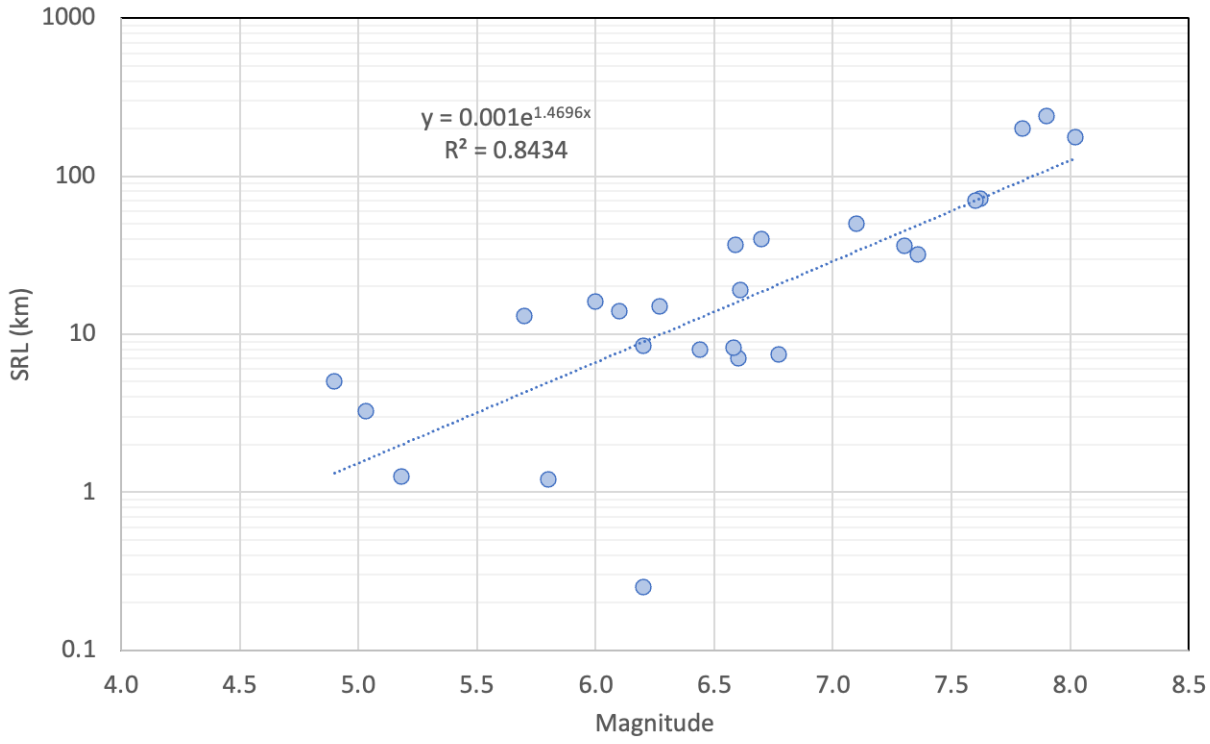

Figure 5.18. Magnitude versus Surface Rupture Length (SRL) in km for the data used in this analysis.

The following plots show the data binnned by magnitude ranges of; 8.0 to 7.5, 7.5 to 7.0, 7.0 to 6.5, 6.5 to 6.0, and 6.0 to 4.9. This binning provided a relatively even distribution of the number of events for each bin and coincides with magnitude ranges that are commonly used in engineering practice. Figure 5.19 shows the data out to the distance extents represented in the FDHI data. No clear trends are observed other than San Fernando dominating the M 6.5 to 6.0 range. Figure 5.20 focuses on the 0 to 3km range and shows the data as well as median trends

for each magnitude bin. Here the median trends show that for this R/RO data that magnitude less than 6.5 tend to dominate the 0.5 km range, which are also on the higher end for the 1.0 km range. This would suggest that the smaller magnitude reverse events have a higher likelihood of producing distributed displacements at these distances than the larger magnitude events.

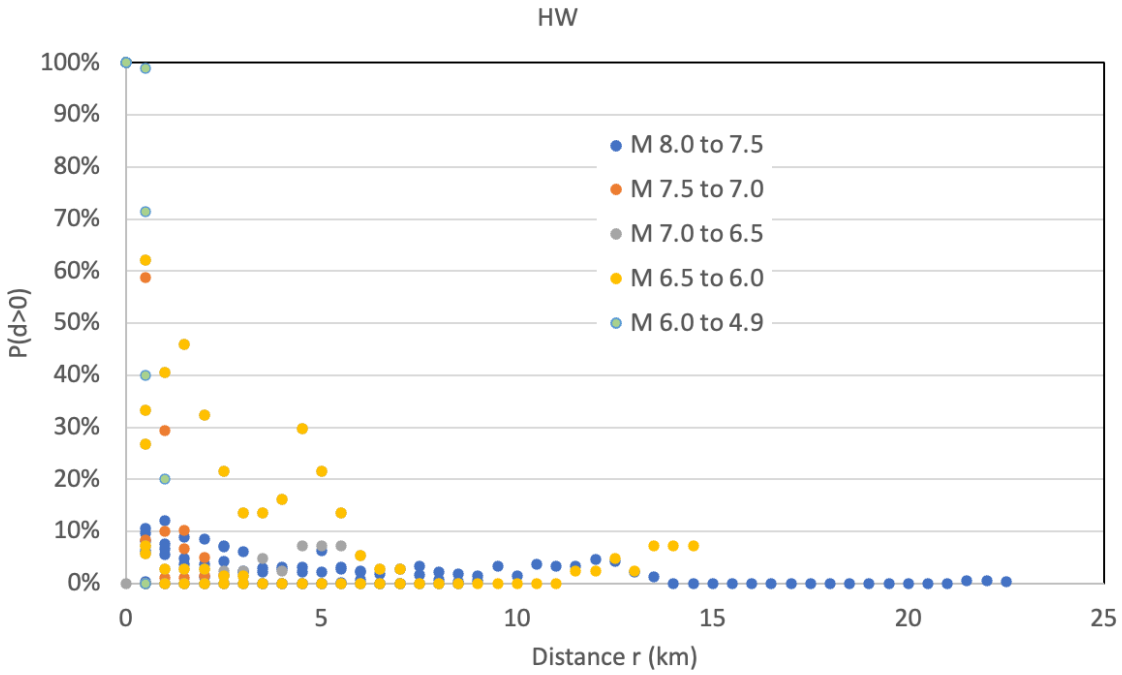

Figure 5.19. Distance versus distributed surface fault rupture binned by magnitude, hanging wall.

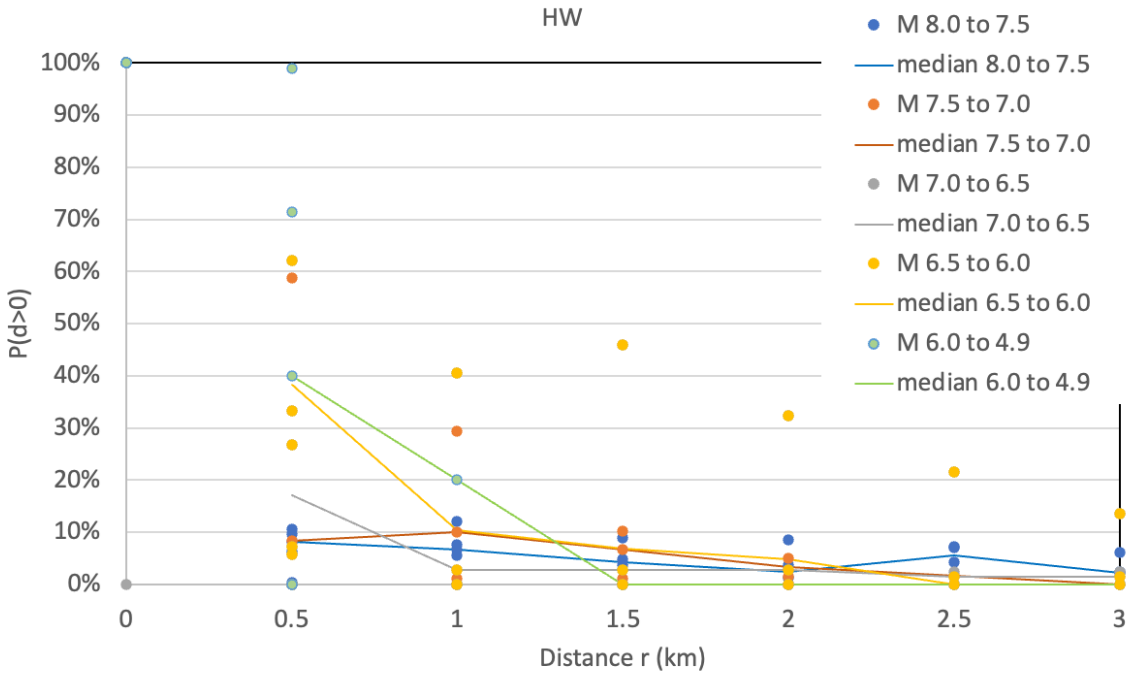

Figure 5.20. Distance versus distributed surface fault rupture binned by magnitude, hanging wall.

The same process was performed for the footwall data. Figures 5.21 shows to the data extent and Figure 5.22 shows out to 3 km with median values. The trend is not as strong as with the hanging wall data.

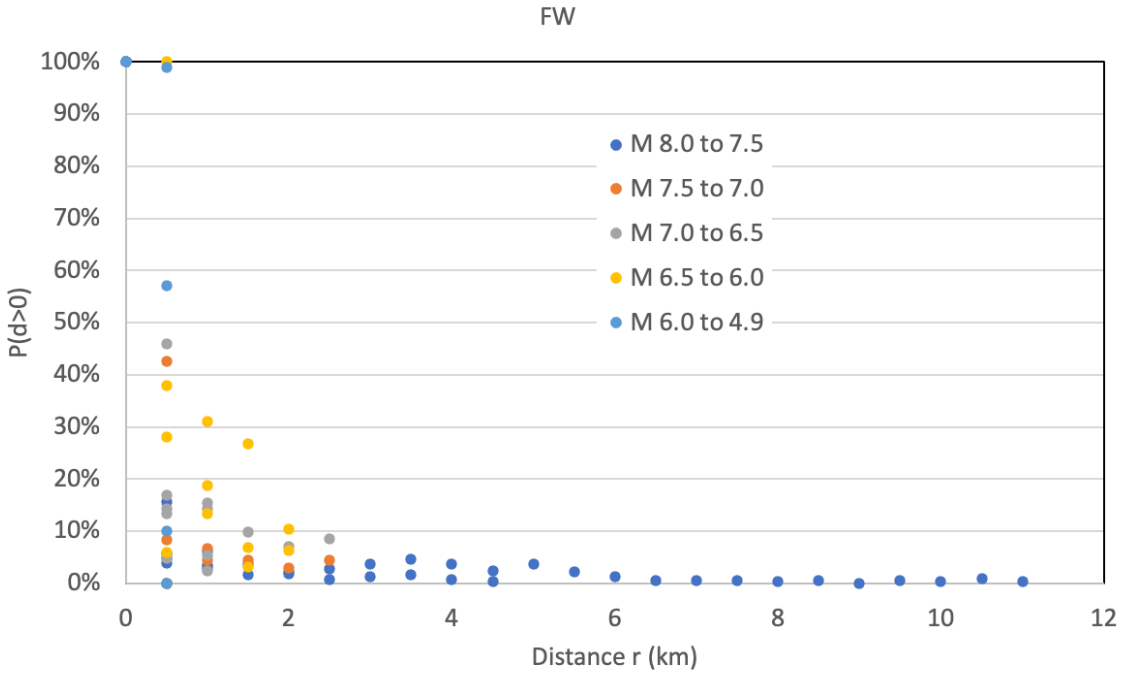

Figure 5.21. Distance versus distributed surface fault rupture binned by magnitude, footwall.

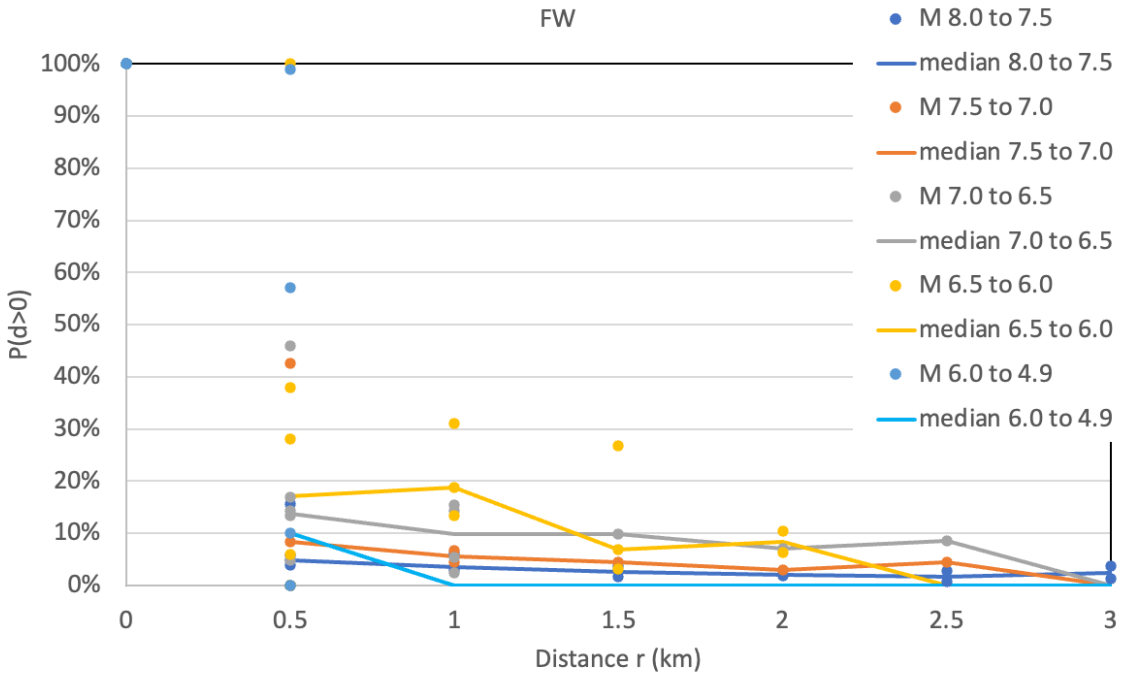

Figure 5.22. Distance versus distributed surface fault rupture binned by magnitude, footwall.

If we inspect the data from a surface rupture length (SRL) perspective, we would expect similar trends because of the correlation between magnitude and SRL. The bins did not necessarily align with the magnitude bins as there is not a 1:1 correlation. Here the bins of > 100 km, 100 to 50, 50 to 25, 25 to 10, 10 to 5, and < 5 km were used as that gave an even distribution of events per bin. We see on the hanging wall side (Figure 5.23) that the bin of 25 to 10 km tends to dominate, however that is due to the San Fernando and Cadoux events falling into this bin. The same is true for the footwall side (Figure 5.24).

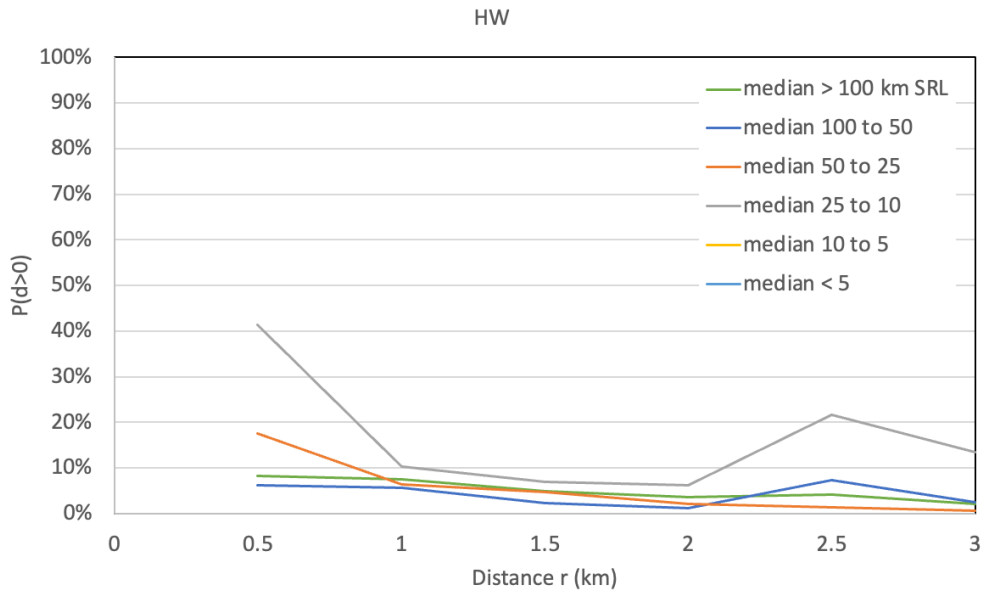

Figure 5.23. Distance versus distributed surface fault rupture binned by surface rupture length, hanging wall.

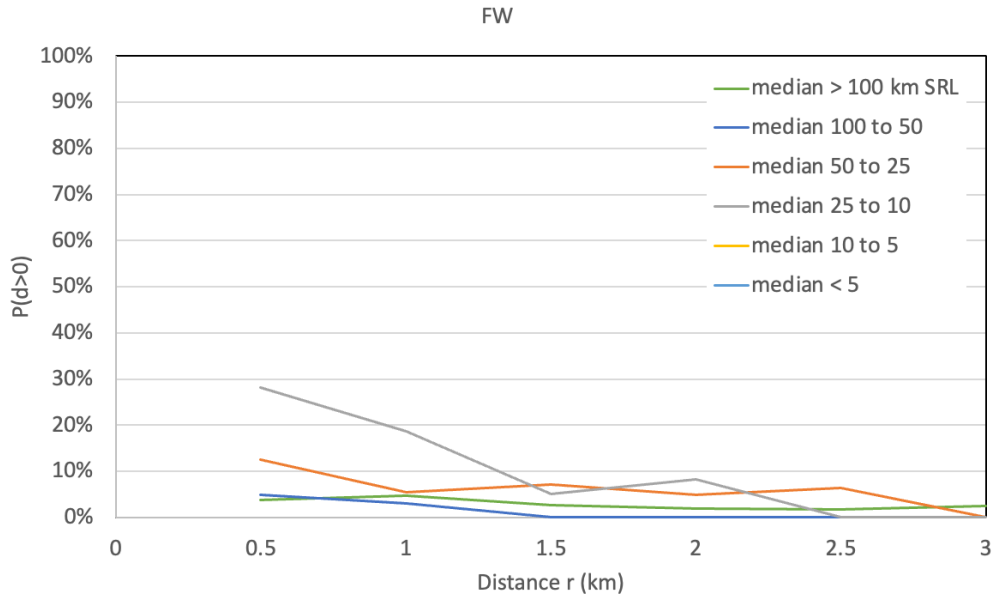

Figure 5.24. Distance versus distributed surface fault rupture binned by surface rupture length, footwall.

Summary of P(d>0) Assessment

The probability of distributed rupture has been examined here for R/RO events. A gridded approach was used (e.g., Petersen et al, 2011). The occurrences of distributed rupture traces were counted within each 500 x 500 m grid cell, and divided by the total number of cells at that specific grid distance from the principal fault trace. Both the FDHI and SURE 2.0 databases were evaluated in this way and reasonable agreement between the two databases was observed in the percentile curves. In general, there is an exponential decay of the probability of distributed deformations away from principal fault trace. Percentiles were calculated and tabulated, and curves were fit to the 85th percentiles for PFDHA coding purposes.

The dependence of this decay was examined per each event, as well as a function of magnitude and surface rupture length. It was found that some events have produced widespread distributed deformations whereas others very limited distributed deformations. For example, the San Fernando event produced many distributed deformation traces out to distances greater than 3 km which was atypical of other events in the database.

There was some magnitude dependence observed in the hanging wall data, where smaller event less than M 6.5 tended to produce a higher likelihood of distributed rupture out to 1 km when compared to larger magnitude events. The dependence on surface rupture length was not as prominent and tended to be controlled by atypical events such as San Fernando.

Distributed deformations were documented out to 22.5 km on the hanging wall and 11 km in the footwall, but these are associated with complex faulting conditions (e.g., conjugate or sympathetic faults) and should be considered when evaluating similar tectonic setting. The 95th percentiles tended towards zero at these large distances because the occurrences were an exception. When working in complex faulting settings it is advised to set the probability to some non-zero value to account for the potential of these rare but not unobserved distributed deformations.

As in most statistical analysis in the geohazard realm, more data is always warranted. We have only 25 events to inform our inferences which is not enough. The median trends are expected to hold true as more data is collected whereas the standard deviation may diminish with more observations.

5.2.2 FREQUENCY OF DISTRIBUTED DEFORMATIONS

The frequency distribution of the data was plotted both in aggregate form and as a function of magnitude bins. Fitting a function to the cumulative frequency data will produce a cumulative distribution function (CDF) that can enable the forecasting of the probability of exceedance.

A key observation of the frequency distribution of the data (e.g., Figure 5.25) is that there is an exponentially decreasing portion that is within the initial few kilometers, followed by a random portion that can reach tens of kilometers from strike. The exponential portion agrees with the analytical solution, whereas the random portion can be seen in other prior studies such as Youngs et al. (2003). After examining the events that contribute to the random portion of the distributed displacements (Wenchuan, Kaikoura, and Rikuu) it was found that these far displacements can be attributed sympathetic and/or conjugate faults and therefore are controlled by a different process than displacement on a single "simple" fault.

To aid in forward modeling of this we have separated the data and provided distributions that fit both;

a) A single fault trace where the mechanics of distributed displacements can be conceptualized similar to the analytical solution presented above, or
b) A complex fault system where distributed displacements may occur at distance due to sympathetic release on adjacent or nearby faults.

The hanging and foot wall plots below show all the data with the exponential and random displacements as well as the exponential displacements only.

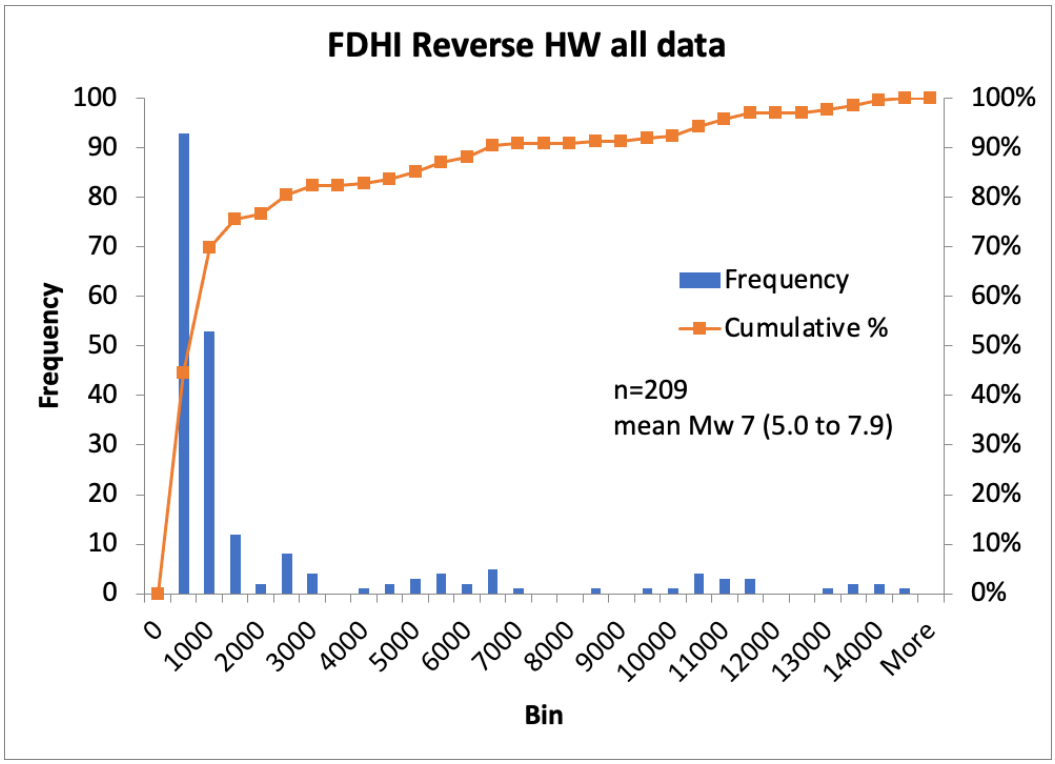

Figure 5.25. FDHI Reverse HW All Data Frequency Plot.

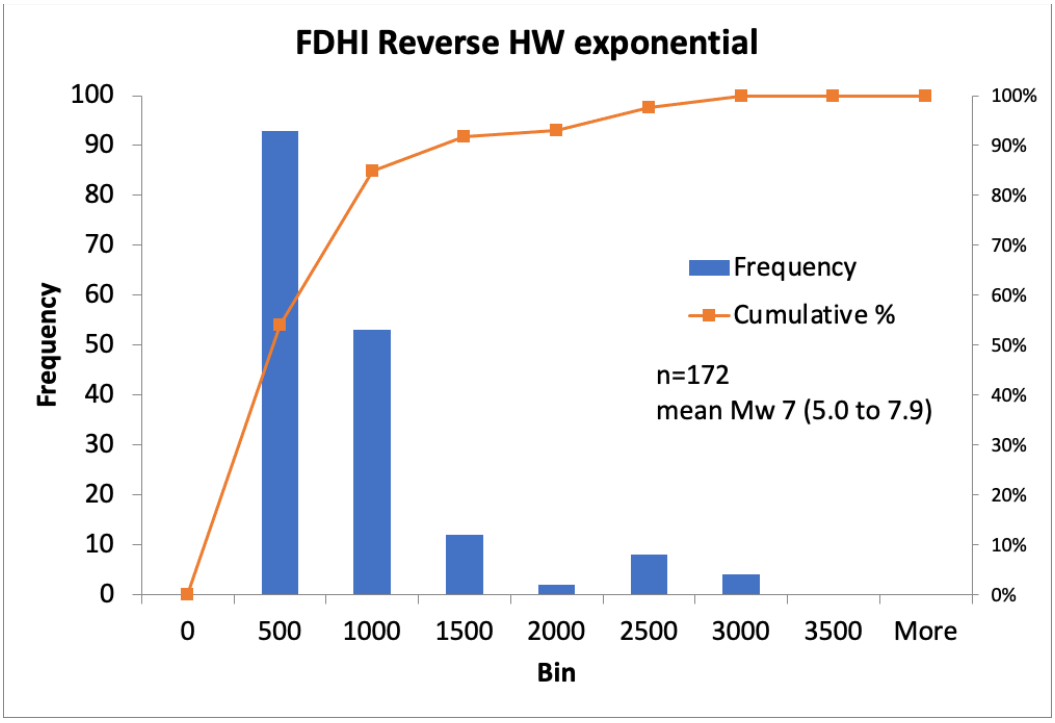

Figure 5.26. FDHI Reverse HW Exponential Data Frequency Plot.

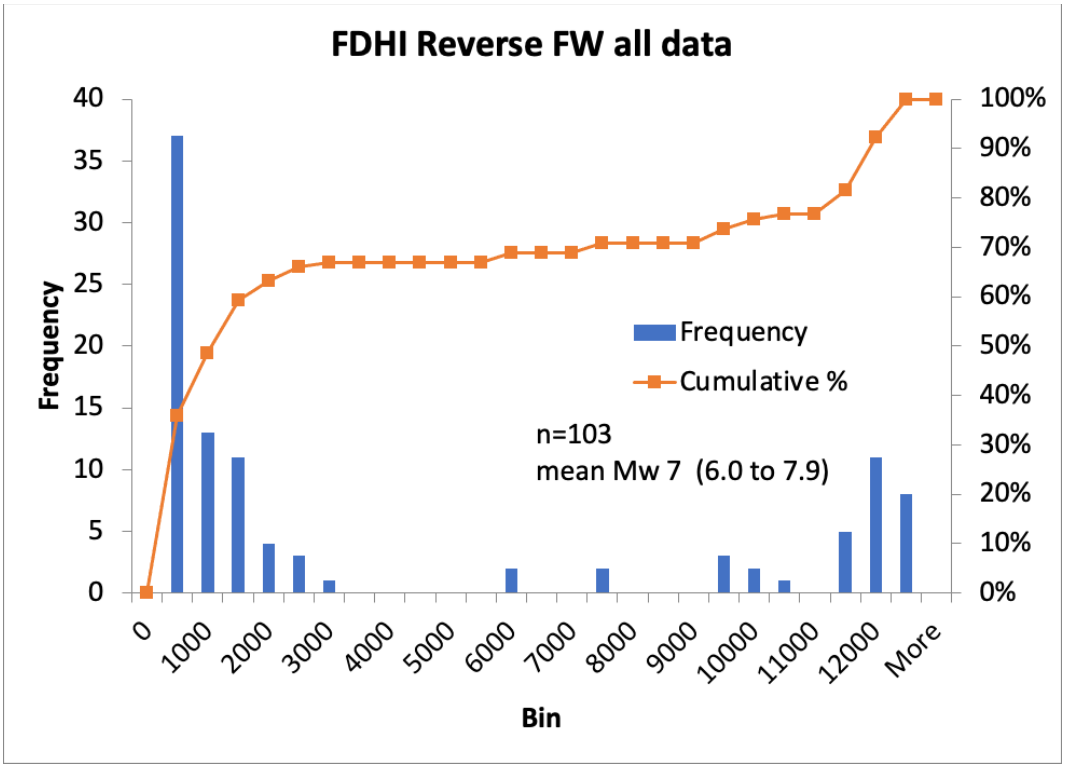

Figure 5.27. FDHI Reverse FW All Data Frequency Plot.

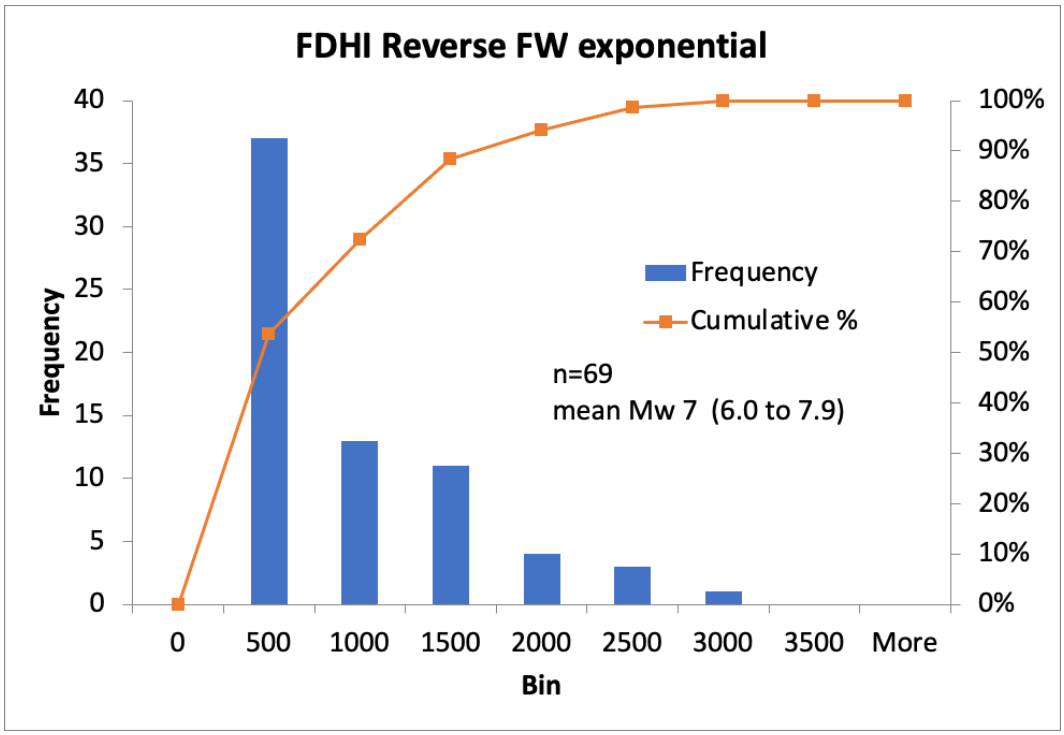

Figure 5.28. FDHI Reverse FW Exponential Data Frequency Plot.

To account for magnitude dependence, the data is binned by magnitude and the frequency distributions are plotted. We have fit curves to the cumulative distributions to provide CDF's for evaluating the probability of exceedance. Here we are accounting for magnitude dependence as well as tectonic dependence by separating out the exponential versus the random portions of displacements. Curve fitting was accomplished using the cftool in Matlab. A 2nd order exponential provided efficient fitting to the cumulative distributions and provide CDF's for forecasting the probability of exceedance. Below are the equations, table, and frequency plots of the hanging wall reverse FDHI data.

$$P(d > d_o) = 1 - F(x) < 1.0 \tag{5.6}$$

$$F(x) = a\exp(b\,x) + c\exp(d\,x) \tag{5.7}$$

Table 5.4. Coefficients for Equation 5.6 for Reverse Mechanism Hanging Wall Distributed Deformations from FDHI data.

	a	b	c	d	R^2 : RMSE
HW (7 to 7.9)+	0.6998	$2.75*10^{-5}$	-0.6931	-0.001219	0.9882 : 0.02474
HW (7 to 7.9)	0.8289	$5.682*10^{-5}$	-0.8346	-0.001735	0.9924 : 0.02972
HW (6 to 6.9)+	0.8858	$6.203*10^{-6}$	-0.8957	-0.001959	0.9904 : 0.01929
HW (6 to 6.9)	1.166	$-4.699*10^{-5}$	-1.1730	-0.001539	0.9957 : 0.03113
HW (5 to 5.9)	98.45	0.0023	-98.53	-0.0142	0.8363 : 23.83

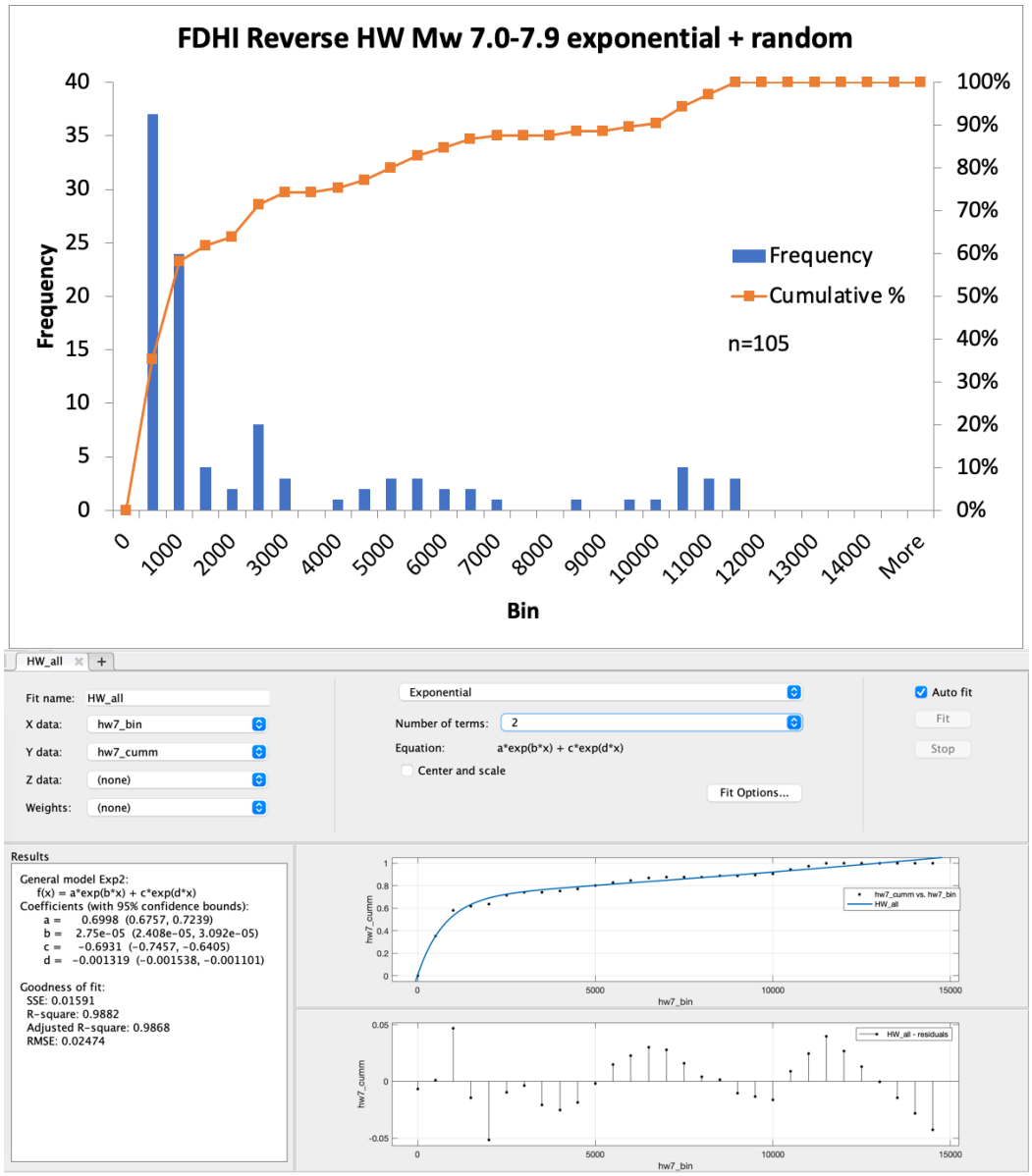

Figure 5.29. Frequency distribution (top) and CDF fitting (bottom) of Mw 7.0-7.9 FDHI hanging wall data, exponential and random.

Figure 5.30. Frequency distribution (top) and CDF fitting (bottom) of Mw 7.0-7.9 FDHI hanging wall data, exponential only.

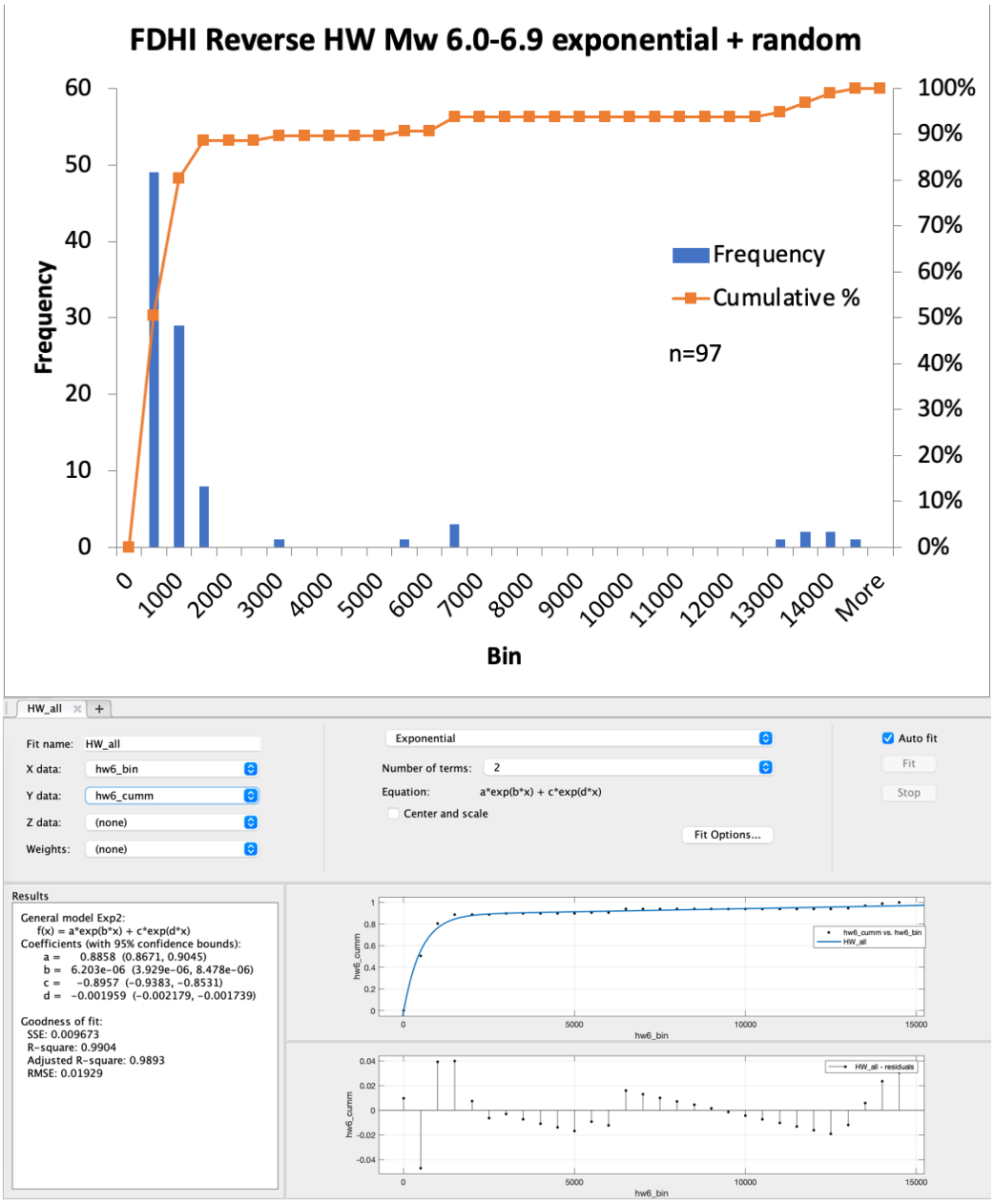

Figure 5.31. Frequency distribution (top) and CDF fitting (bottom) of Mw 6.0-6.9 FDHI hanging wall data, exponential and random.

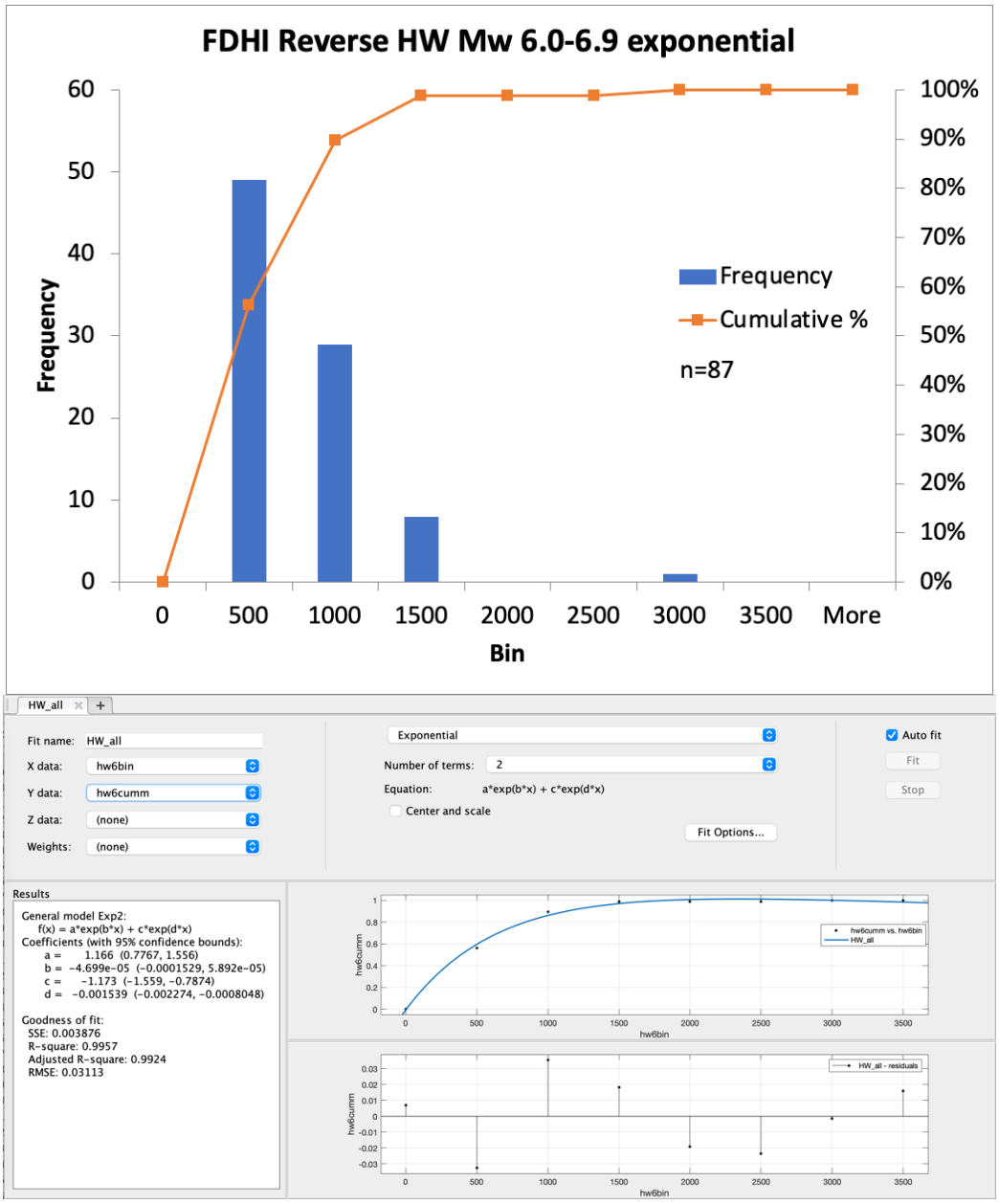

Figure 5.32. Frequency distribution (top) and CDF fitting (bottom) of Mw 6.0-6.9 FDHI hanging wall data, exponential only.

Note that there was no random portion of displacement for the Mw 5.0-5.9 bin. In addition, this bin showed displacements less than 100 m so the bin widths were reduced to 20 m to better quantify the data in this range.

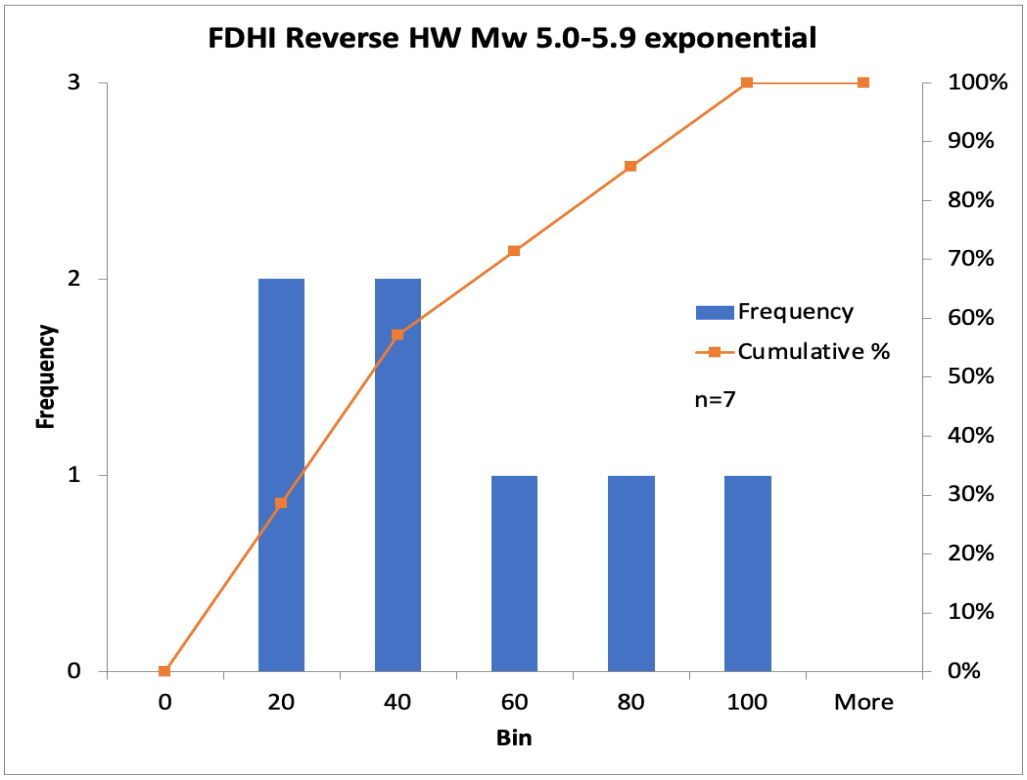

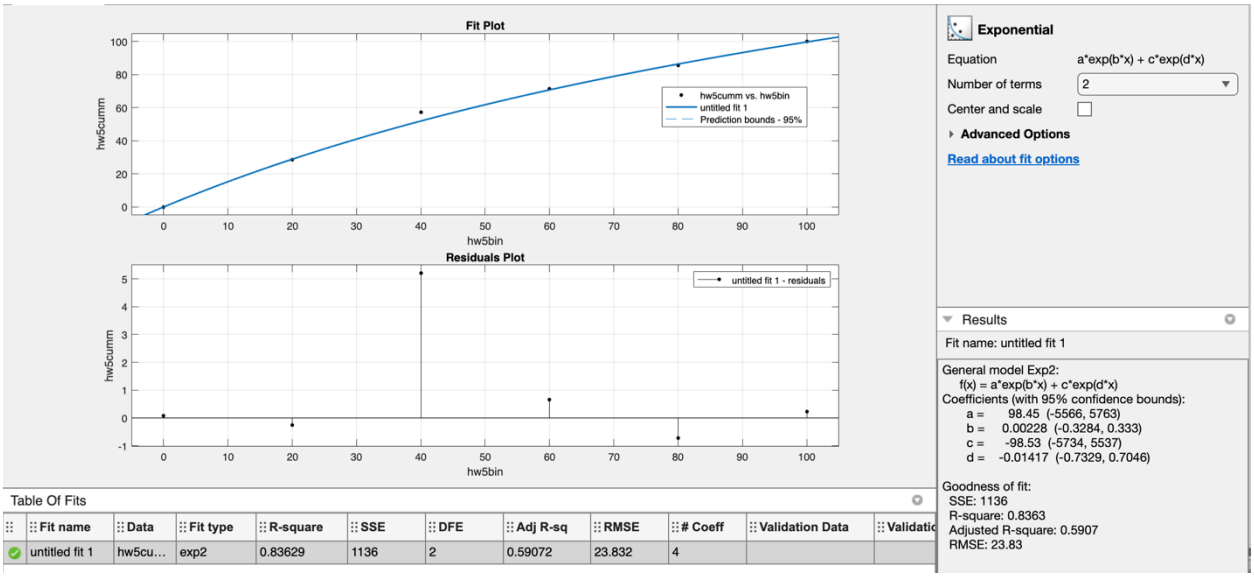

Figure 5.33. Frequency distribution (top) and CDF fitting (bottom) of Mw 5.0-5.9 FDHI hanging wall data.

Below are the frequency plots and the table of footwall data evaluated for magnitude and tectonic dependence.

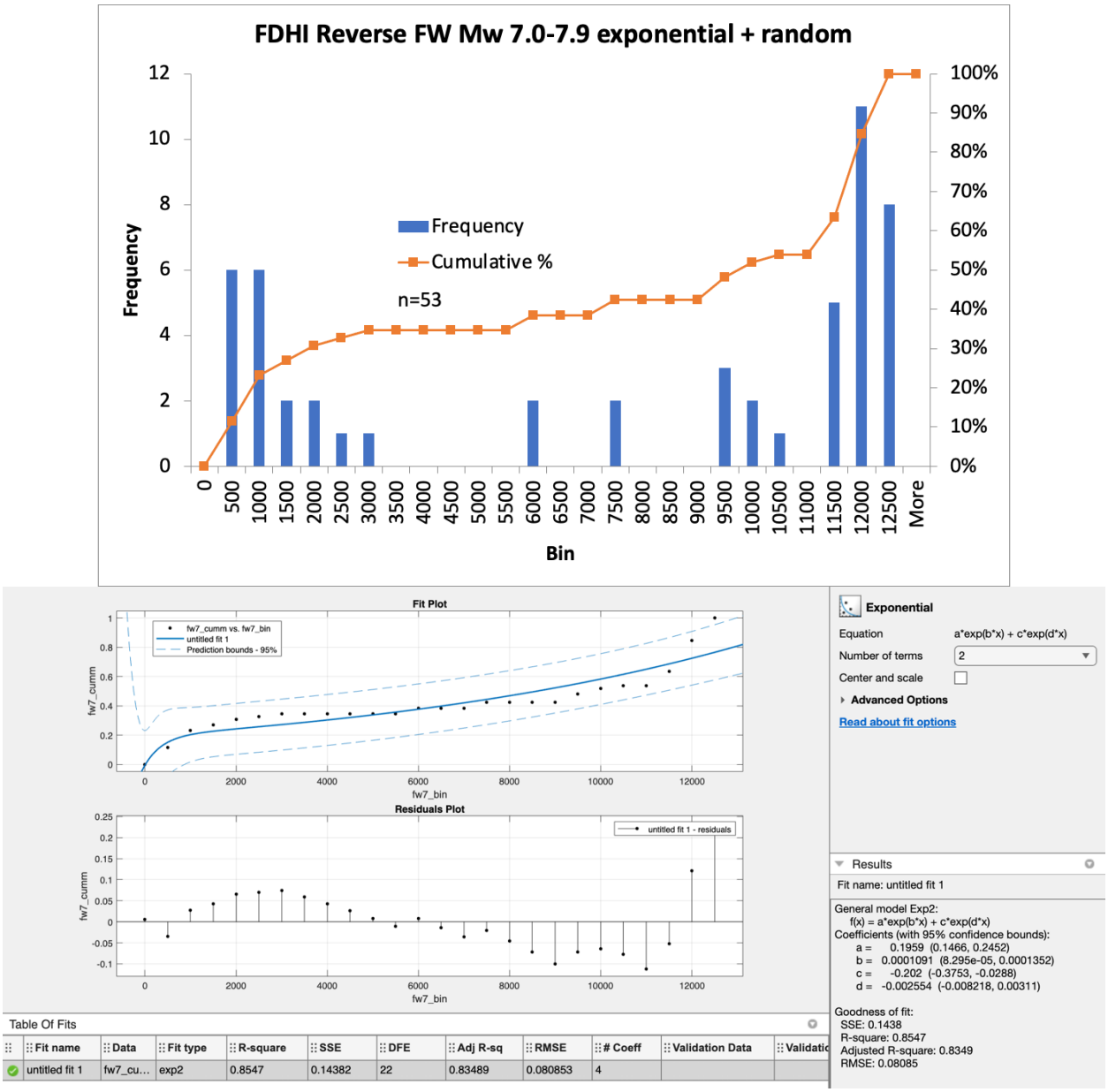

Figure 5.34. Frequency distribution (top) and CDF fitting (bottom) of Mw 7.0-7.9 FDHI footwall data, exponential and random.

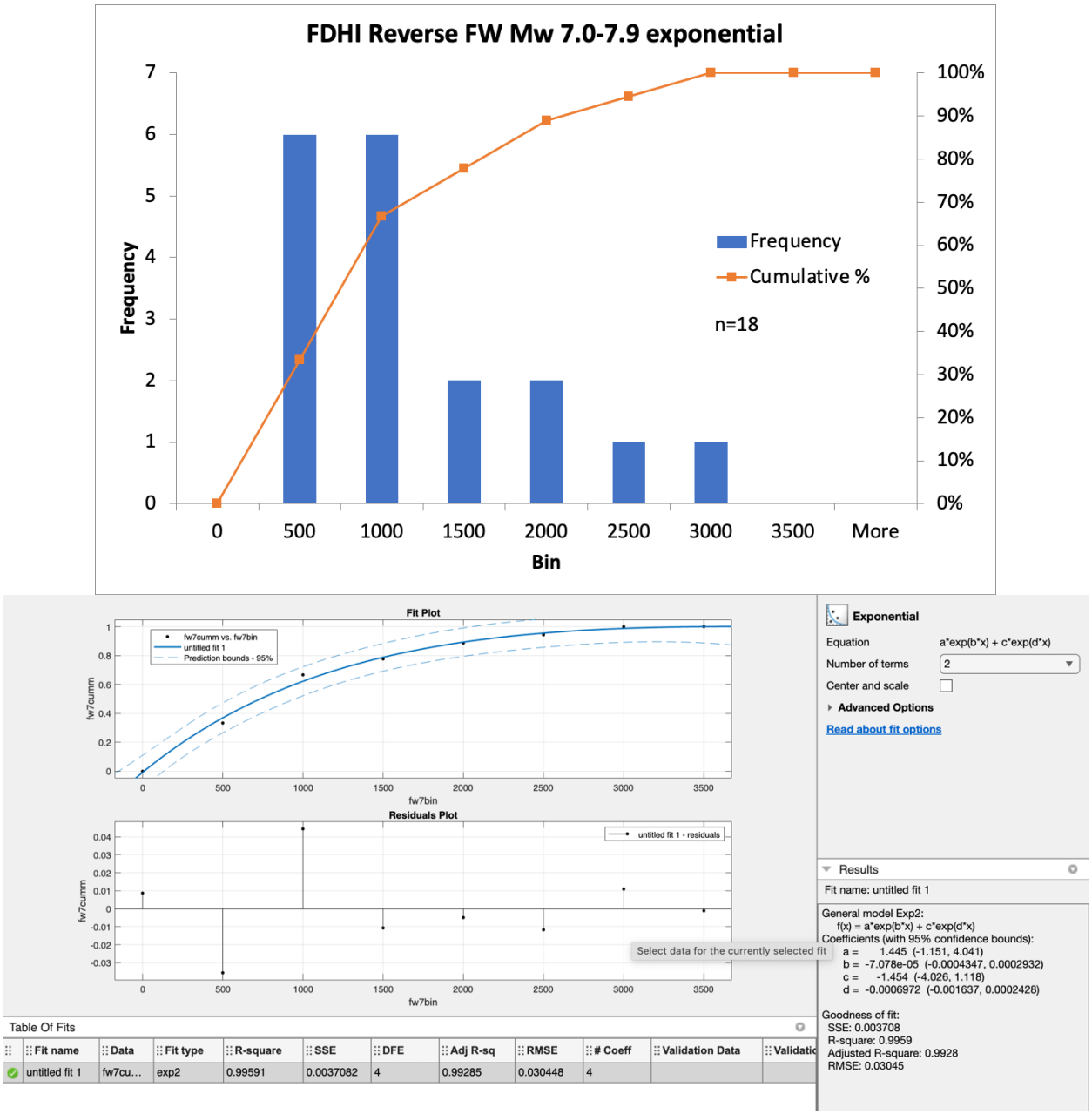

Figure 5.35. Frequency distribution (top) and CDF fitting (bottom) of Mw 7.0-7.9 FDHI footwall data, exponential only.

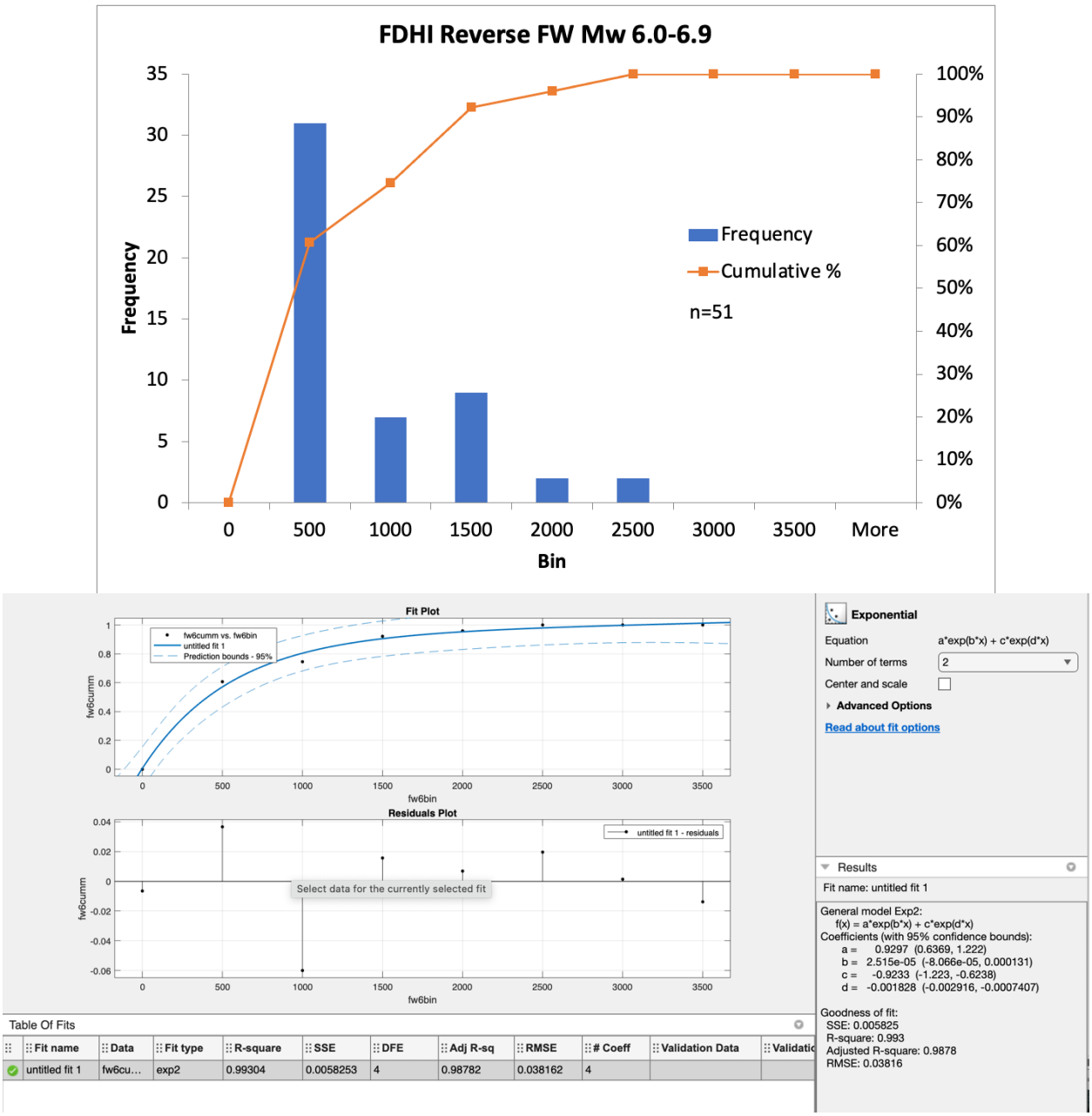

Figure 5.36. Frequency distribution (top) and CDF fitting (bottom) of Mw 6.0-6.9 FDHI foot wall data.

Note the FDHI database of reverse events contained no random portion of displacements for the Mw 6.0-6.9 bin for foot wall. In addition, there were no foot wall distributed displacements measured for Mw less than 6.0.

Table 5.5. Coefficients for Equation 26 for Reverse Mechanism Footwall Distributed Deformations from FDHI data.

	a	b	c	d	R2 : RMSE
FW (7 to 7.9)+	0.1959	0.0001	-0.2020	-0.0026	0.8547 : 0.08085
FW (7 to 7.9)	1.445	$-7.08*10^{-5}$	-1.4540	-0.0007	0.9959 : 0.03045
FW (6 to 6.9)	0.9297	$2.51*10^{-5}$	-0.9233	-0.002	0.9930 : 0.03816

5.2.3 NORMALIZED SCALING OF DISTRIBUTED DEFORMATIONS

To provide scaling of the distributed displacements (d) we have normalized it by the maximum (MD) and average (AD) principal displacement for each event. Figure 1 shows all events color coded to observe the contribution each has to the footwall (negative *r* values) and the hanging wall (positive *r* values). Here *r* is the distance from principal fault strike. Both d/MD and d/AD relationships are shown.

Figure 2 provides box plots of the data to observe the central tendency and dispersion. The lower plot shows the specific values that are used to calculate the statistics. Figure 3 shows the 50th percentile values from the binned data. Various bin sizes were evaluated and it was found that the following bins, $\pm$0.1km centered on zero, 0.1 to 1km, 1km to 3km, and greater than 3km, provided the clearest explanation of changes with distance given the current data density.

Subsequent plots (Figure 4) show the exploration of how the 50th percentiles are affected by dropping individual events out. Here we can see that Kaikoura has a large impact on the distances far from principal strike. Meckering has an impAact in the 1 to 3 km range. Other events that have a lesser impact on the percentiles at less than 3 km are Chi Chi and Tennant Creek2.

Figure 5 shows the d/MD data using the 95th percentiles compared to other studies. Figure 6 shows the d/MD data using the 50th percentile and fitting an envelope compared to other studies. The envelope uses the following exponential form:

$$d/MD = c * \exp(d * r) \tag{5.8}$$

Coefficients are shown in Tables 2 and 3. Figure 7 shows the d/AD data using the 95th percentiles compared to other studies, and Figure 8 shows the d/AD using 50th percentile and fitting an envelope compared to other studies.

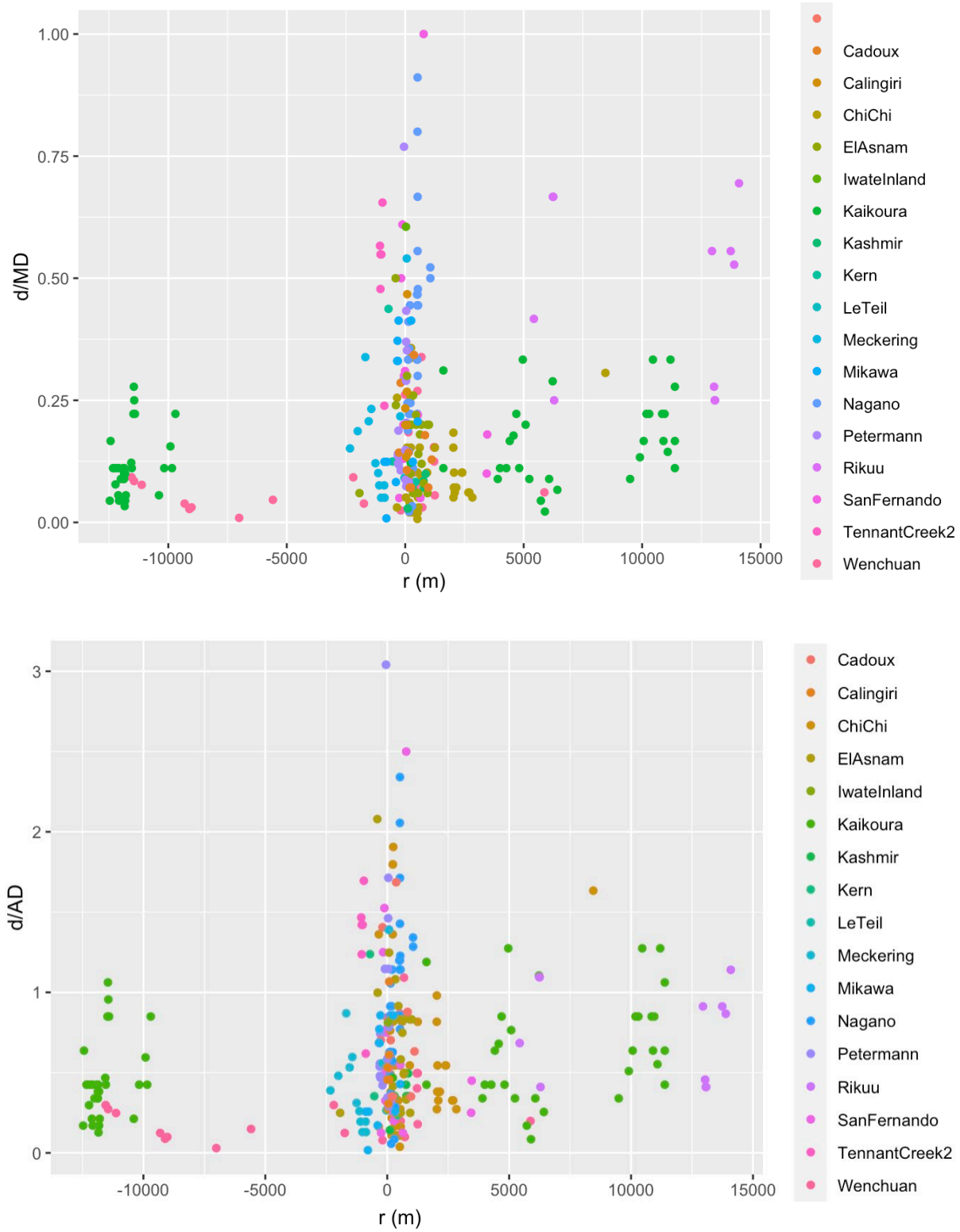

Figure 5.37. Upper figure shows d/MD, lower figure shows d/AD. Color coded by event to show the relative contribution to different regions of the footwall (negative r) and hanging wall (positive r) space.

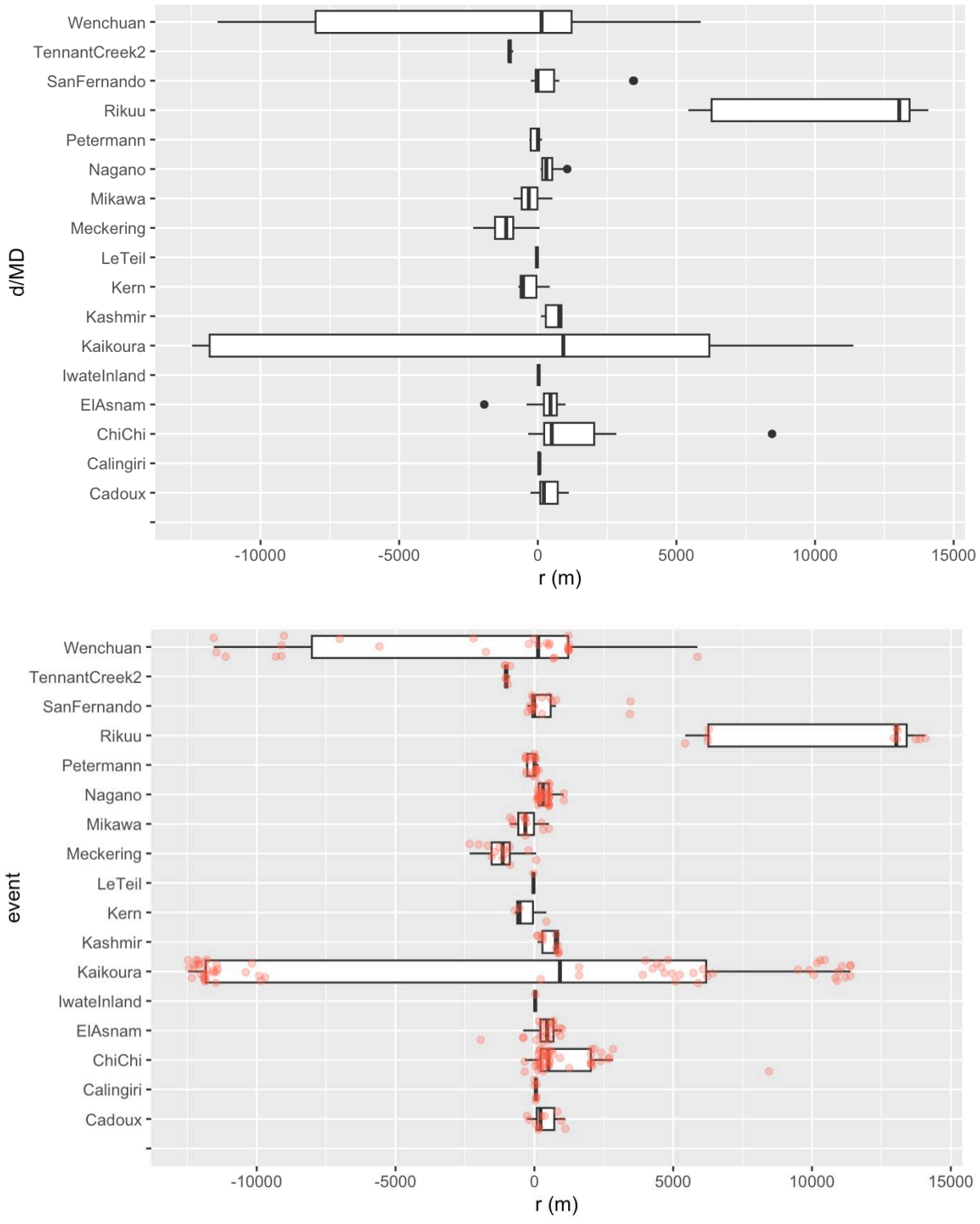

Figure 5.38. Both figures showing box plots of the normalized distributed displacements (d). Lower figure shows the individual data points for perspective.

Figure 5.39. These plots show the 50th percentiles for binned data (gray diamonds). The upper plot shows for the whole range of the data and the lower plot for the plus and minus three kilometers range. Vertical dark lines show the extents of the bins used.

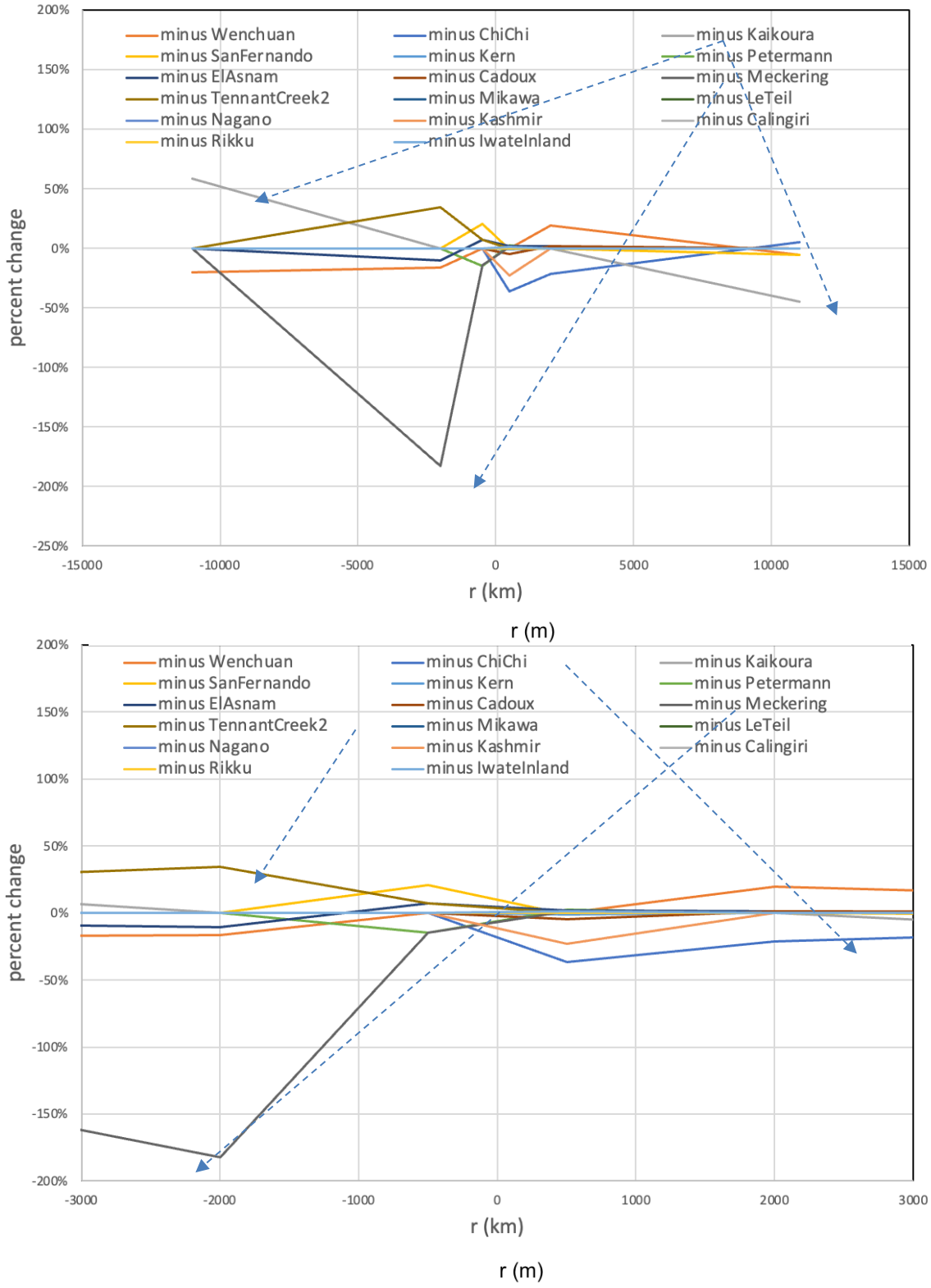

Figure 5.40. Percent change in 50th percentiles when events are dropped out individually.

Table 5.6. Showing percentiles for d/MD and d/AD over the *r* (m) range.

d/MD							
r	-11000	-2000	-550	0	550	2000	11000
95th	0.225	0.553	0.555	0.573	0.476	0.453	0.650
85th	0.159	0.531	0.425	0.402	0.350	0.188	0.379
50th	0.092	0.169	0.143	0.244	0.121	0.127	0.211
15th	0.043	0.064	0.063	0.119	0.045	0.061	0.089
5th	0.028	0.048	0.028	0.081	0.020	0.052	0.062
d/AD							
r	-11000	-2000	-550	0	550	2000	11000
95th	0.860	1.432	1.610	1.588	1.784	1.261	1.274
85th	0.607	1.375	1.306	1.318	1.119	0.869	1.095
50th	0.340	0.435	0.558	0.750	0.493	0.496	0.637
15th	0.142	0.208	0.167	0.335	0.179	0.327	0.340
5th	0.089	0.128	0.102	0.282	0.109	0.272	0.206

From this analysis the median ratio of MD/AD for distributed displacements within plus/minus 3 km of principal faulting is 3.5.

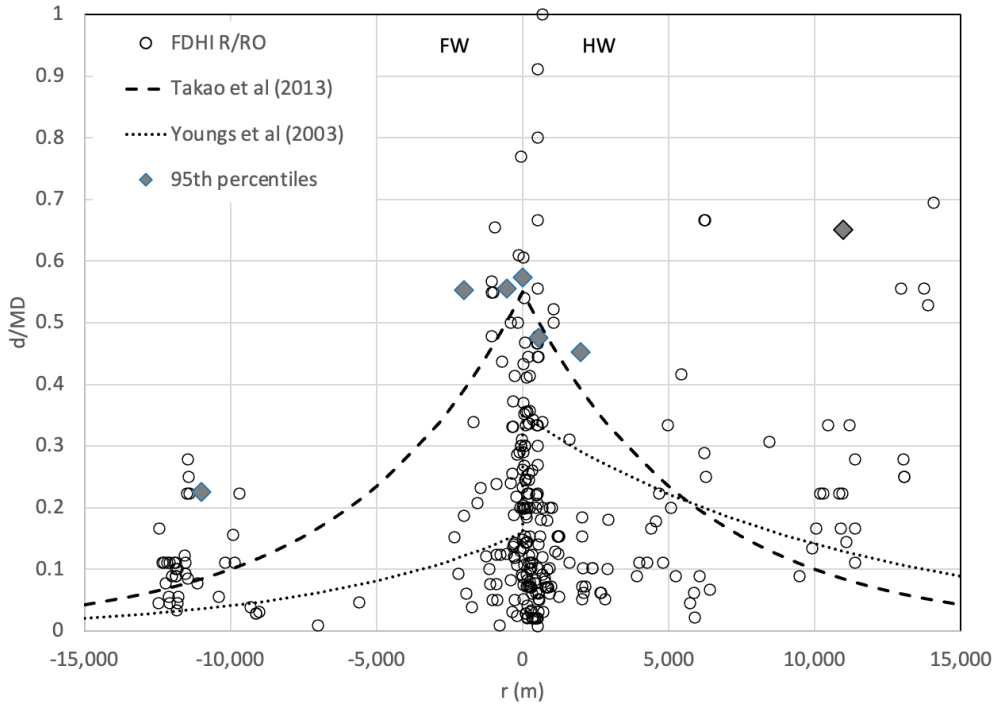

Figure 5.41. The d/MD is shown with 95th percentile values as compared to curves from other studies. Takao et al (2013) curves are for the 90th percentile for reverse and strike slip events. Youngs et al (2003) curves are for 85th to 95th percentile for normal events.

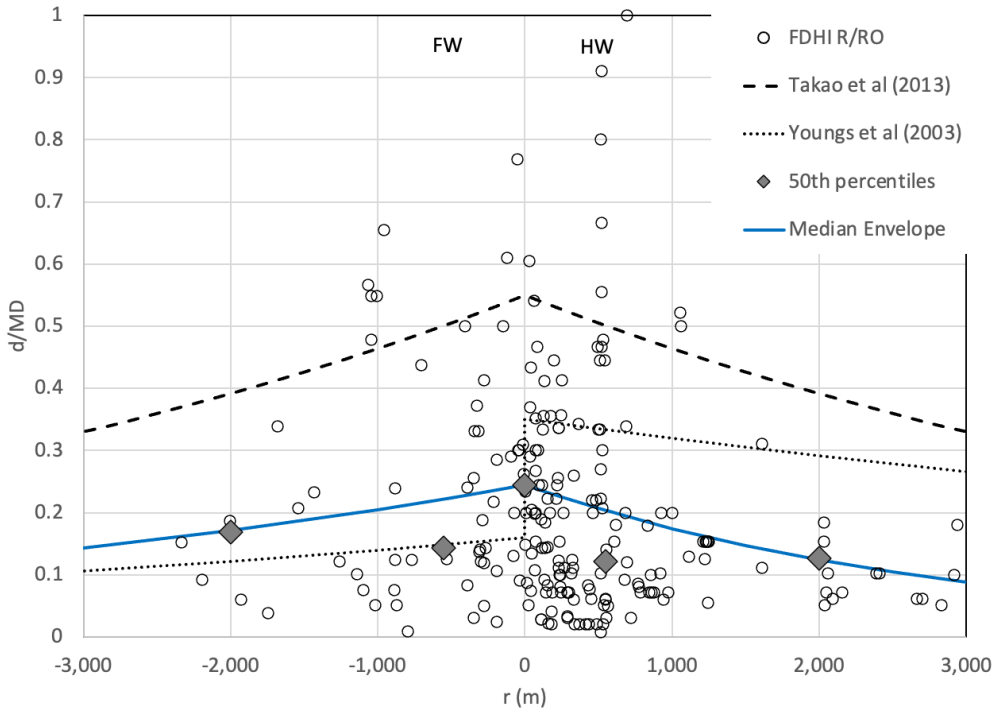

Figure 5.42. The d/MD is shown here with a 50th percentile envelope for simple faulting compared to curves from other studies.

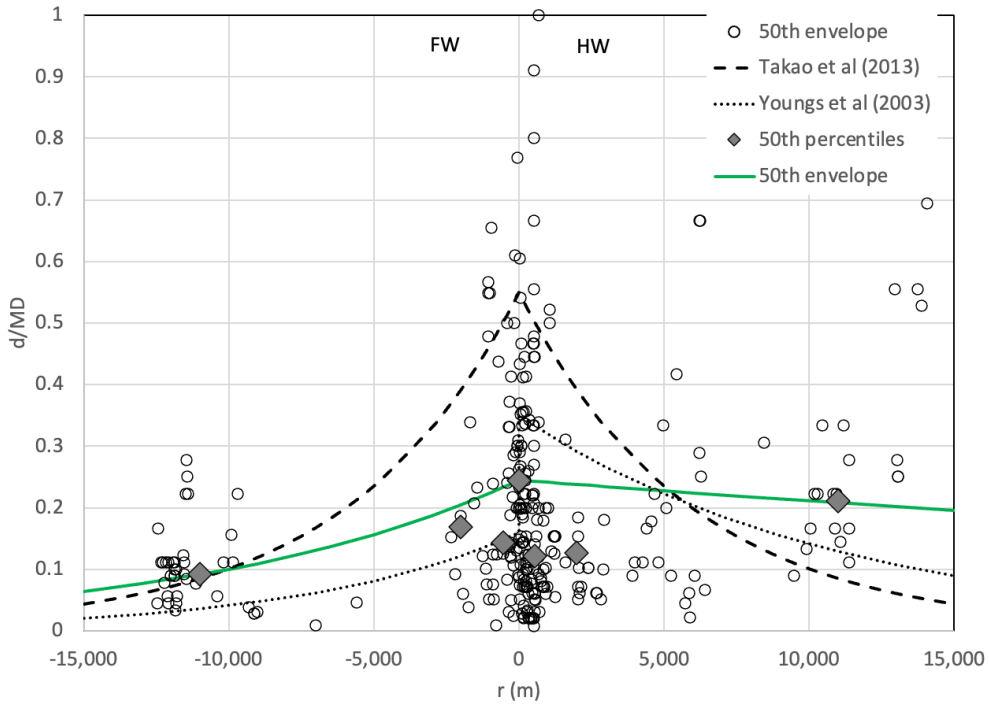

Figure 5.43. The d/MD is shown here with a 50th percentile envelope for complex faulting compared to curves from other studies.

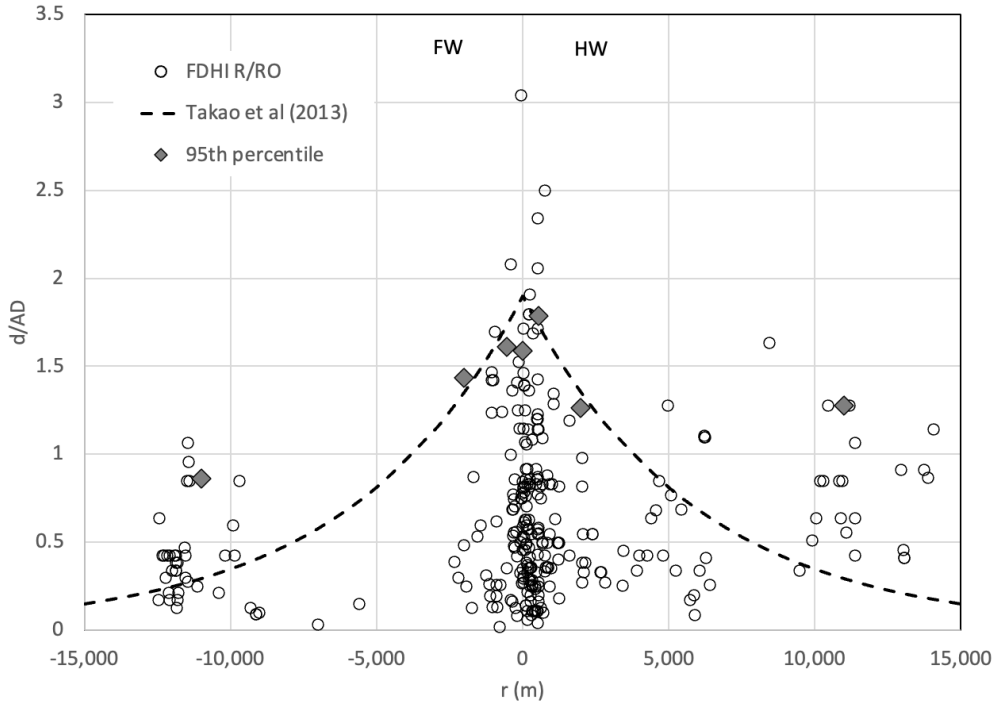

Figure 5.44. The d/AD with 95th percentile values as shown compared to another study. Takao et al (2013) curves are for the 90th percentile for reverse and strike slip events.

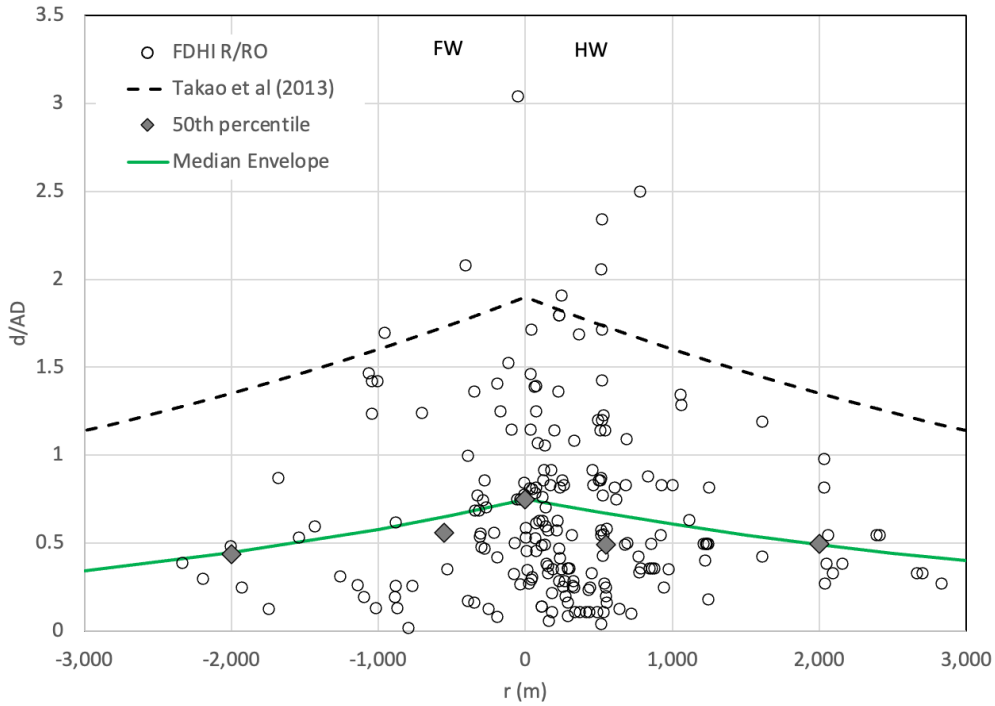

Figure 5.45. The d/AD with 50th percentile values and median envelope compared to other studies.

Table 5.7. d/MD coefficients for median envelope for simple and complex faulting.

d/MD simple

coeff c	coeff d	
0.245	-0.18	FW
0.245	-0.34	HW

d/MD complex

coeff c	coeff d	
0.245	-0.09	FW
0.245	-0.015	HW

Table 5.8. d/MD coefficients for 85th percentile envelope for simple and complex faulting.

d/MD simple

coeff c	coeff d	
0.68	-0.13	FW
0.43	-0.4	HW

d/MD complex

coeff c	coeff d	
0.68	-0.13	FW
0.43	-0.012	HW

6 Hazard Curves

Combining the spatial variability of displacement and the dependence of surface rupture on magnitude we arrive at Equation 2 from before:

$$P^*(D > D_0|m, x/L) = P(SurfRup|m, Slip)\, P\left(D > D_0\middle|m, \frac{x}{L}, SurfRup\right) \qquad (6.1)$$

The final complementary cumulative distribution is found by combining the distributions, based on one or more MD- or AD-based models. [As each of these probability distributions represents a random variable and the product of these yields a probability distribution of displacement given the occurrence of a magnitude m earthquake that ruptures past a site.]

A product of random variables can be shown to be equivalent to a logarithmic convolution (Glen et al., 2004). By combining like distribution to like distribution [i.e., $P(MD) * P(D/MD)$ or $P(AD) * P(D/AD)$] we can arrive at the probability of exceedance and combining that with the distribution of magnitude, typically a truncated exponential, and a fault rate, we can estimate the displacement for an annualized return.

$$\upsilon(D_o) = \alpha \int_{m_{min}}^{m_{max}} f(m)\, P(D > D_o|m, x/L)\, dm \qquad (6.2)$$

Numerically integrating the above equations was accomplished using Monte Carlo simulations. We generate a realization of the spatial slip distribution and multiply it by a realization of the displacement distribution and then repeat the process thousands of times to achieve a stable resultant distribution. The same calculations are performed for distributed displacement as well, which is based on normalized maximum principal displacement (*d/MD*) relationships.

An example hazard curve is shown below for a Mw7.5 reverse fault with a 5mm/yr slip rate, fault dimensions of 100km by 15km, stiff soil conditions (VS30>600m/s), middle of the fault where x/L is 0.5, hanging wall conditions, and simple fault geometry. This figure shows how principal and distributed displacements vary with distance from the fault.

Using a 975 year return period, which is typical of highway bridges, we can see that an 85th percentile estimate of displacement on the fault is 0.7m, at 100m from the fault it is 0.25m, and at 500m from the fault it is 0.03m. Displacements beyond 500m are possible but for this hazard level are not forecast.

The Matlab code for calculating hazard curves based on *AD*, *MD*, and *d* are provided in Appendix C. The code requires the Statistics and Machine Learning Toolbox to run.

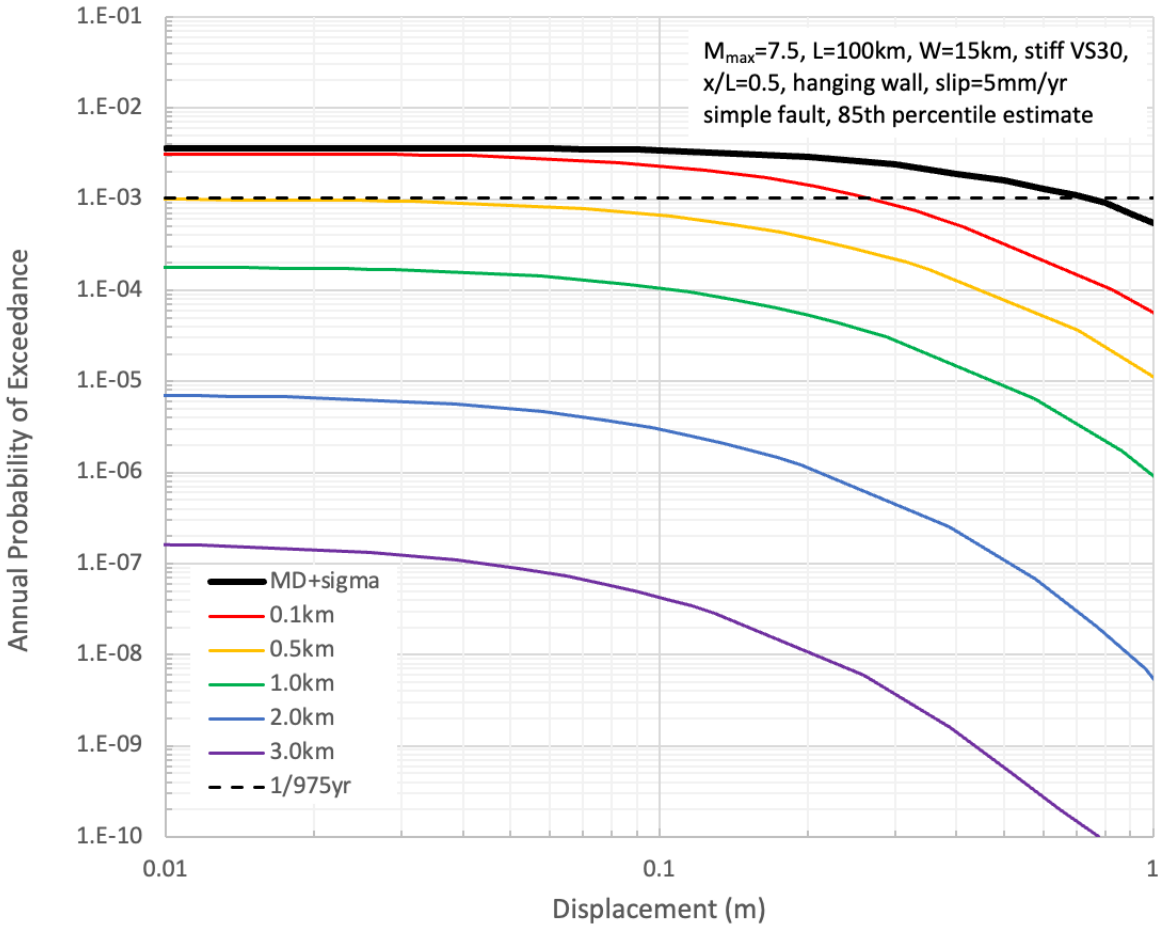

Figure 6.1. Example hazard curve showing principal and distributed displacements for different distances. These curves are showing results based on the 85th percentile of maximum displacement (MD). The 975 year return period is shown, a typical hazard level for lifeline infrastructure.

7 Summary

This report contains the current methodology developed by this research team for forecasting the probability of surface fault rupture for Reverse events. The methodology presents models for average (AD) and maximum (MD) principal displacement, as well as for distributed displacement (d). The data that was used to develop these models was primarily based on the FDHI database but was also informed by the SURE 2.0 database. The models are valid within the data ranges of the databases and extrapolating beyond those data ranges is not statistically supported.

REFERENCES

Allen, T. I., & Wald, D. J. (2009). On the use of high-resolution topographic data as a proxy for seismic site conditions (VS 30). Bulletin of the Seismological Society of America, 99(2A), 935-943.

Baize, S., Nurminen, F., Sarmiento, A., Dawson, T., Takao, M., Scotti, O., Azuma, T., Boncio, P., Champenois, J., Cinti, F. R., Civico, R., Costa, C., Guerrieri, L., Marti, E., McCalpin, J., Okumura, K., and Villamor, P. (2020). A worldwide and Unified Database of Surface Ruptures (SURE) for fault displacement hazard analyses, Seismological Research Letters, 91(1), 499–520.

Bawden, G. (2001). Source parameters for the 1952 Kern County earthquake, California: A joint inversion of leveling and triangulation observations, Journal of Geophysical Research, 106(B1), 771–785.

Biasi, G. P., & Weldon, R. J. (2006). Estimating surface rupture length and magnitude of paleoearthquakes from point measurements of rupture displacement. Bulletin of the Seismological Society of America, 96(5), 1612-1623.

Boncio, P., Liberi, F., Caldarella, M., & Nurminen, F. C. (2018). Width of surface rupture zone for thrust earthquakes: implications for earthquake fault zoning. Natural Hazards and Earth System Sciences, 18(1), 241-256.

Box, G. E., & Cox, D. R. (1964). An analysis of transformations. Journal of the Royal Statistical Society: Series B (Methodological), 26(2), 211-243

Buwalda, J. P., and St. Amand, P. (1955). Geological effects of the Arvin-Tehachapi earthquake, in Oakeshott, G. (editor), Earthquakes in Kern County, California during 1952, California Division of Mines Bulletin 171, 41–56.

Caquot, A., & Kerisel, J. (1948). Tables de butée, de poussée et de force portante des fondations. Librairie du bureau des longitudes, de l'école polytechnique.

Caskey, J. (1995). Geometric relations of dip slip to a faulted ground Surface: New nomograms for estimating components of fault displacement, Journal of Structural Geology, 17(8), 1197–1202.

Chiou, B. S. J., & Youngs, R. R. (2008). NGA model for average horizontal component of peak ground motion and response spectra. PEER Report No. 2008/09, Pacific Earthquake Engineering Research Center, University of California, Berkeley.

Dolan, J. and Haravitch, B. (2014). How well do surface slip measurements track slip at depth in large strike-slip earthquakes? The importance of fault structural maturity in controlling on-fault slip versus off-fault surface deformation, Earth and Planetary Science Letters, 388, 38–47.

Ellsworth, W. (2003). Appendix D—Magnitude and area data for strike slip earthquakes, In, Working Group on California Earthquake Probabilities (WGCEP), 2003, Earthquake probabilities in the San Francisco Bay region; 2002–2031: U. S. Geological Survey Open-File Report 2003–214, 13p., available online: https://pubs.usgs.gov/of/2003/of03-214/.

Fialko, Y., Sandwell, D., Simons, M., and Rosen, P. (2005). Three-dimensional deformation caused by the Bam, Iran, earthquake and the origin of shallow slip deficit, Nature. 435, 295–299.

Glen, J. M., McKee, E. H., Ludington, S., Ponce, D. A., Hildenbrand, T. G., & Hopkins, M. J. (2004). Geophysical terranes of the Great Basin and parts of surrounding provinces. US Geological Survey Open-File Report, 1008, 303.

Goulet, C., Bozorgnia, Y., Abrahamson, N., Kuehn, N., Al Atik, L., Youngs, R., Graves, R., and Atkinson, G. (2018). Central and eastern North America ground-motion characterization. PEER Report No. 2018/08, Pacific Earthquake Engineering Research Center, University of California, Berkeley.

Hanks, T., and Bakun, W. (2002). A bilinear source-scaling model for M-log A observations of continental earthquakes, Bulletin of the Seismological Society of America, 92(5), 1841–1846.

Hanks, T., and Bakun, W. (2008). M-log A Observations for Recent Large Earthquakes, Bulletin of the Seismological Society of America, 98, 490–494.

Hanks, T., and Bakun, W. (2014). M-log A Models and Other Curiosities, Bulletin of the Seismological Society of America, 104(5), 2,604–2,610.

Heaton, T., Tajima, F., and Mori, A. (1986). Estimating ground motions using recorded accelerograms, Surveys in Geophysics, 8(1), 25–83.

Hecker, S., Abrahamson, N., and Wooddell, K. (2013). Variability of displacement at a point: Implications for earthquake-size distribution and rupture hazard on faults, Bulletin of the Seismological Society of America, 103, 651–674.

Kaneda, H., Nakata, T., Tsutsumi, H., Kondo, H., Sugito, N., Awata, Y., ... & Kausar, A. B. (2008). Surface rupture of the 2005 Kashmir, Pakistan, earthquake and its active tectonic implications. Bulletin of the Seismological Society of America, 98(2), 521-557.

King, T., Quigley, M., and Clark, D. (2019). Surface-rupturing historical earthquakes in Australia and their environmental effects: new insights from re-analysis of observational data, Geosciences, 9, 408, doi:10.3390/geosciences9100408.

Leonard, M. (2010). Earthquake fault scaling: Self-consistent relating of rupture length, width, average displacement, and moment release. Bulletin of the Seismological Society of America, 100(5A), 1971-1988.

Leonard, M. (2014). Self-consistent earthquake fault-scaling relations: Update and extension to stable continental strike-slip faults. Bulletin of the Seismological Society of America, 104(6), 2953-2965.

Lettis, W. R., Wells, D. L., & Baldwin, J. N. (1997). Empirical observations regarding reverse earthquakes, blind thrust faults, and quaternary deformation: Are blind thrust faults truly blind? Bulletin of the Seismological Society of America, 87(5), 1171-1198.

Manighetti, I., Campillo, M., Sammis, C., Mai, P. M., & King, G. (2005). Evidence for self-similar, triangular slip distributions on earthquakes: Implications for earthquake and fault mechanics. Journal of Geophysical Research: Solid Earth, 110(B5).

Marchandon, M., Hollingsworth, J., and Radiguet, M. (2021). Origin of the shallow slip deficit on a strike slip fault: influence of elastic structure, topography, data coverage, and noise, Earth and Planetary Science Letters, 554, doi:10.1016/j.epsl.2020.116696.

McCalpin, J. and Carver, G. (2009). Chapter 5—Paleoseismology of compressional tectonic environments, in, McCalpin, J. (ed)., Paleoseismology, Second Edition, International Geophysics, 95, 315–419.

Moss, R. E. S., Buelna, M., & Stanton, K. V. (2018). Physical, analytical, and numerical modeling of reverse-fault displacement through near-surface soils. Bulletin of the Seismological Society of America, 108(6), 3149-3159.

Moss, R. E. S., Stanton, K. V., & Buelna, M. I. (2013). "The impact of material stiffness on the likelihood of fault rupture propagating to the ground surface." Seismological Research Letters, 84(3), 485-488.

Moss, R.E.S. and Ross, Z. (2011). "Probabilistic Fault Displacement Hazard Analysis for Reverse Faults." Bulletin of Seismological Society of America, 101(4), 1542-1553.

Nurminen, Fiia, Baize, Stéphane, Boncio, Paolo, Blumetti, Anna Maria, Cinti, Francesca R., Civico, Riccardo, & Guerrieri, Luca. (2022a). SURE 2.0. [Data set]. Zenodo. https://doi.org/10.5281/zenodo.6461588

Nurminen, Fiia, Baize, Stéphane, Boncio, Paolo, Blumetti, Anna Maria, Cinti, Francesca R., Civico, Riccardo, & Guerrieri, Luca. SURE 2.0. (2022b). New release of the worldwide database of surface ruptures for fault displacement hazard analyses. Scientific Data. (submitted)

Oakeshott, G. (editor) (1955). Earthquakes in Kern County, California During 1952, California Division of Mines Bulletin 171, 294 p.

Petersen, M. D., Dawson, T. E., Chen, R., Cao, T., Wills, C. J., Schwartz, D. P., & Frankel, A. D. (2011). Fault displacement hazard for strike-slip faults. Bulletin of the Seismological Society of America, 101(2), 805-825.

Ritz, J-F., Baize, S., Ferry, M., Larroque, C., Audin, L., Delouis, B., and Mathot, E. (2020). Surface rupture and shallow fault reactivation during the 2019 Mw 4.9 Le Teil earthquake, France, Communications Earth & Environment, doi:10.1038/s43247-020-0012-z.

Sarmiento, A., Madugo, D., Bozorgnia, Y., Shen, A., Mazzoni, S., Lavrentiadis, G., Dawson, T., Madugo, C., Kottke, A., Thompson, S., Baize, S., Milliner, C., Nurminen, F., Boncio, P., and Visini, F. (2021). Fault Displacement Hazard Initiative Database: GIRS Report 2021-08, B. John Garrick Institute for the Risk Sciences, University of California Los Angeles, available online: https://www.risksciences.ucla.edu/girs-reports/2021/08

Savage, H. M., & Brodsky, E. E. (2011). Collateral damage: Evolution with displacement of fracture distribution and secondary fault strands in fault damage zones. Journal of Geophysical Research: Solid Earth, 116(B3).

Shaw, B. E. (2013). Earthquake surface slip-length data is fit by constant stress drop and is useful for seismic hazard analysis. Bulletin of the Seismological Society of America, 103(2A), 876-893.

Shaw, B.E. (2009). Constant stress drop from small to great earthquakes in magnitude-area scaling, Bulletin of the Seismological Society of America, 99(2A), 871, doi:10.1785/0120080006.

Shaw, B.E. (2013). Appendix E—Evaluation of Magnitude-Scaling Relationships and Depth of Rupture, in, Field, E.H., et al., Uniform California earthquake rupture forecast, version 3 (UCERF3) - The time-independent model, U.S. Geological Survey Open-File Report 2013–1165_Appendix E., 23 p.

Streig, Ashley R., Charles M. Rubin, Wen-Shan Chen, Yue-Gau Chen, Long-Sheng Lee, Stephen C. Thompson, Chris Madden, and Shih-Ting Lu. (2007) "Evidence for prehistoric coseismic folding along the Tsaotun segment of the Chelungpu fault near Nan-Tou, Taiwan." Journal of Geophysical Research: Solid Earth 112, no. B3.

Takao, M., Tsuchiyama, J., Annaka, T., & Kurita, T. (2013). Application of probabilistic fault displacement hazard analysis in Japan. Journal of Japan Association for Earthquake Engineering, 13(1), 17-36.

Takao, M., Ueta, K., Annaka, T., Kurita, T., Makase, H., Kyoya, T., & Kato, J. (2014). Reliability improvement of probabilistic fault displacement hazard analysis. Japan Association for Earthquake Engineering, 14(2), 16-36.

Takao, M., Annaka, T., and Kurita, T. (2018). Establishment of evaluation formulae for probabilistic fault displacement hazard analysis (PFDHA) in Japan. In, Best Practices in Physics-Based Fault Rupture Models for Seismic Hazard Assessment of Nuclear Installations, IAEA TECDOC CD 1833, 16 p.

Talebian, M., Biggs, J., Bolourchi, M., Copley, A., Ghassemi, A., Ghorashi, M., Hollingsworth, J., Jackson, J., Nissen, E., Oveisi, B., Parsons, B., Priestley, K., and Saiidi, A. (2006).

The Dahuiyeh (Zarand) earthquake of 2005 February 22 in central Iran: reactivation of an intramountain reverse fault, Geophysical Journal International, 164, 137–148.

Terzaghi, K., Theoretical Soil Mechanics, John Wiley and Sons, New York (1943) ISBN 0-471-85305-4.

Thingbaijam, K. K. S., Martin Mai, P., & Goda, K. (2017). New empirical earthquake source-scaling laws. Bulletin of the Seismological Society of America, 107(5), 2225-2246.

Utsu, T. (2002). Chapter 43—Statistical features of seismicity, International Geophysics, 81(A), 719–732.

Valentini, A., Fukushima, Y., Contri, P., Ono, M., Sakai, T., Thompson, S. C., Viallet, E., Annaka, T., Chen, R., Moss, R. E. S., Petersen, M. D., Visini, F., and Youngs, R. R. (2021). Probabilistic Fault Displacement Hazard Assessment (PFDHA) for nuclear installations according to IAEA safety standards. Bulletin of the Seismological Society of America, 111(5), 2661–2672.

Wald, D. J., & Allen, T. I. (2007). Topographic slope as a proxy for seismic site conditions and amplification. Bulletin of the Seismological Society of America, 97(5), 1379-1395.

Walker, R., Bergman, E., Jackson, J., Ghorashi, M., and Talebian, M. (2005). The 22 June 2002 Changureh (Avaj) earthquake in Qazvin province, NW Iran: epicentral re-location, source parameters, surface deformation and geomorphology, Geophysical Journal International, 160, 707–720.

Wells, D. L., & Coppersmith, K. J. (1994). New empirical relationships among magnitude, rupture length, rupture width, rupture area, and surface displacement. Bulletin of the seismological Society of America, 84(4), 974-1002.

Wesnousky, S. G. (2008). Displacement and geometrical characteristics of earthquake surface ruptures: Issues and implications for seismic-hazard analysis and the process of earthquake rupture. Bulletin of the Seismological Society of America, 98(4), 1609-1632.

Xu, X., Tong, X., Sandwell, D., Milliner, C., Dolan, J., Hollingsworth, J., Leprince, S., and Ayoub, F. (2016). Refining the shallow slip deficit, Geophysical Journal International, 204, 1867–1886.

Yang, H., Quigley, M., and King, T. (2021). Surface slip distributions and geometric complexity of intraplate reverse-faulting earthquakes, Geological Society of America Bulletin, 133(9-10), 1909–1929.

Yang, X., Li, W., and Zhen, Q. (2015). Calculation of reverse-fault-related parameters using topographic profiles and fault bedding, Geodesy and Geodynamics, 6(2), 106–112.

Yeats, R., Sieh, K., and Allen, C. (1997). The Geology of Earthquakes, Oxford University Press, New York, 576 p.

Youngs, R.R., Arabasz, W.J., Anderson, R.E., Ramelli, A.R., Ake, J.P., Slemmons, D.B., McCalpin, J.P., Doser, D.I., Fridrich, C.J., Swan III, F.H. and Rogers, A.M. (2003). A methodology for probabilistic fault displacement hazard analysis (PFDHA). Earthquake Spectra, 19(1), pp.191-219.

Appendix A

The following Appendix contains example Matlab code for fitting distributions to the D/MD data. A similar process was used for fitting distributions to the D/AD data. This requires the Statistics and Machine Learning Toolbox.

```
%Performing stats on D/MD data        3/17/21

%load DMD-XL_VS_P.mat  this is the D/MD values for principal vertical slip

clf;

%Concatenating arrays vertically using [A;B]

x_L=all(:,2);
D_MD=all(:,1);

%x_L=[Bohol91(:,2);ChiChi20(:,2);ChiChi65(:,2);ChiChi66(:,2);Kashmir71(:,2);N
agano68(:,2);Nagano69(:,2);Nagano70(:,2);Wenchuan44(:,2);Wenchuan45(:,2);Wenc
huan46(:,2);Wenchuan50(:,2);Wenchuan51(:,2)];
%D_MD=[Bohol91(:,1);ChiChi20(:,1);ChiChi65(:,1);ChiChi66(:,1);Kashmir71(:,1);
Nagano68(:,1);Nagano69(:,1);Nagano70(:,1);Wenchuan44(:,1);Wenchuan45(:,1);Wen
chuan46(:,1);Wenchuan50(:,1);Wenchuan51(:,1)];
%x_L_new=[Kaikora32(:,2);Kaikora33(:,2);Kaikora34(:,2);Kaikora73(:,2);SanFern
ando2(:,2);SanFernando86(:,2);Kern122(:,2);Petermann120(:,2);ElAsnam134(:,2);
ElAsnam135(:,2);Cadoux136(:,2);Calingiri136(:,2);MarryatCreek136(:,2);Meckeri
ng136(:,2);Pukatja136(:,2);TennantCreek1136(:,2);Rikuu86(:,2);Mikawa86(:,2);I
wateinland86(:,2);ChonKemin152(:,2)]

figure(1)
semilogy(x_L,D_MD,'o')
grid
xlabel('x/L','Fontsize',14)
ylabel('D/MD','Fontsize',14)

%figure(2)
%histogram(x_L)
%xlabel('x/L','Fontsize',14)
%ylabel('Frequency','Fontsize',14)

figure(2)
histogram(D_MD)
xlabel('D/MD','Fontsize',14)
ylabel('Frequency','Fontsize',14)

%%%%%%%%%%%%%%%%%
%Anderson Darling test
% exponential (Gamma which is a subset of exponential) distribution
% p value less than 0.05 or 5% indicates high chance the distribution fits

[h,p,adstat,cv]=adtest(D_MD,'Distribution','exp');

%[h,p,adstat,cv]=adtest(x_L,'Distribution','Weibull');
```

```
%[h,p,adstat,cv]=adtest(x_L,'Distribution','normal');
%[h,p,adstat,cv]=adtest(x_L,'Distribution','lognormal');

%%%%%%%%%%%%%%%%%%%%%%%%
%Fitting Distributions

%force all inputs to be column vectors
D_MD = D_MD(:);

%prepare figure
figure(3)
hold on;
LegHandles = []; LegText = {};


%plot data originally in dataset "x_L data"
[CdfF,CdfX] = ecdf(D_MD,'Function','cdf');  % compute empirical cdf
BinInfo.rule = 1;
[~,BinEdge] = internal.stats.histbins(D_MD,[],[],BinInfo,CdfF,CdfX);
[BinHeight,BinCenter] = ecdfhist(CdfF,CdfX,'edges',BinEdge);
hLine = bar(BinCenter,BinHeight,'hist');
set(hLine,'FaceColor','none','EdgeColor',[0.333333 0 0.666667],...
    'LineStyle','-', 'LineWidth',1);
xlabel('D/MD','Fontsize',14);
ylabel('Frequency','Fontsize',14)
LegHandles(end+1) = hLine;
LegText{end+1} = 'D/MD data';

%create grid where function will be computed
XLim = get(gca,'XLim');
XLim = XLim + [-1 1] * 0.01 * diff(XLim);
XGrid = linspace(XLim(1),XLim(2),100);

%fit this distribution to get parameter values
pd_all = fitdist(D_MD, 'gamma');
YPlot = pdf(pd_all,XGrid);
hLine = plot(XGrid,YPlot,'Color',[1 0 0],...
    'LineStyle','-', 'LineWidth',2,...
    'Marker','none', 'MarkerSize',6);
LegHandles(end+1) = hLine;
LegText{end+1} = 'gamma';

%adjust figure
box on;
hold off;

%create legend from accumulated handles and labels
hLegend = legend(LegHandles,LegText,'Orientation', 'vertical', 'FontSize',
14, 'Location', 'northeast');
set(hLegend,'Interpreter','none');

pd_all
```

```
%sorting by x/L bins of 0.05 width

block=[x_L,D_MD];
sorted=sortrows(block);
x_L_sort=sorted(:,1);
D_MD_sort=sorted(:,2);

l1=sum(x_L_sort<=0.0499);
bin1=D_MD_sort(1:l1);

l2=sum(x_L_sort>=0.05 & x_L_sort<=0.0999);
bin2=D_MD_sort(l1+1:l1+l2);

l3=sum(x_L_sort>=0.10 & x_L_sort<=0.1499);
bin3=D_MD_sort(l1+l2+1:l1+l2+l3);

l4=sum(x_L_sort>=0.15 & x_L_sort<=0.1999);
bin4=D_MD_sort(l1+l2+l3+1:l1+l2+l3+l4);

l5=sum(x_L_sort>=0.20 & x_L_sort<=0.2499);
bin5=D_MD_sort(l1+l2+l3+l4+1:l1+l2+l3+l4+l5);

l6=sum(x_L_sort>=0.25 & x_L_sort<=0.2999);
bin6=D_MD_sort(l1+l2+l3+l4+l5+1:l1+l2+l3+l4+l5+l6);

l7=sum(x_L_sort>=0.30 & x_L_sort<=0.3499);
bin7=D_MD_sort(l1+l2+l3+l4+l5+l6+1:l1+l2+l3+l4+l5+l6+l7);

l8=sum(x_L_sort>=0.35 & x_L_sort<=0.3999);
bin8=D_MD_sort(l1+l2+l3+l4+l5+l6+l7+1:l1+l2+l3+l4+l5+l6+l7+l8);

l9=sum(x_L_sort>=0.40 & x_L_sort<=0.4499);
bin9=D_MD_sort(l1+l2+l3+l4+l5+l6+l7+l8+1:l1+l2+l3+l4+l5+l6+l7+l8+l9);

l10=sum(x_L_sort>=0.45 & x_L_sort<=0.50);
bin10=D_MD_sort(l1+l2+l3+l4+l5+l6+l7+l8+l9+1:l1+l2+l3+l4+l5+l6+l7+l8+l9+l10);


%gamma fit by bin

pd_1 = fitdist(bin1, 'gamma')
pd_2 = fitdist(bin2, 'gamma')
pd_3 = fitdist(bin3, 'gamma')
pd_4 = fitdist(bin4, 'gamma')
pd_5 = fitdist(bin5, 'gamma')
pd_6 = fitdist(bin6, 'gamma')
pd_7 = fitdist(bin7, 'gamma')
pd_8 = fitdist(bin8, 'gamma')
pd_9 = fitdist(bin9, 'gamma')
pd_10 = fitdist(bin10, 'gamma')
```

Appendix B

The following Appendix contains the 500m x 500m gridded events from the FDHI database for determining the probability of nonzero distributed displacements. Notes:

1) Red lines are principal faults and blue lines are distributed faults.
2) Green circles indicate distributed ruptures on hanging wall and magenta crosses indicate distributed ruptures on footwall.
3) Sometimes it is difficult to determine HW or FW if an event has complex principal faults. For example, the Kaikoura earthquake.
4) An event may have no distributed rupture. For example, the Marryat Creek earthquake.

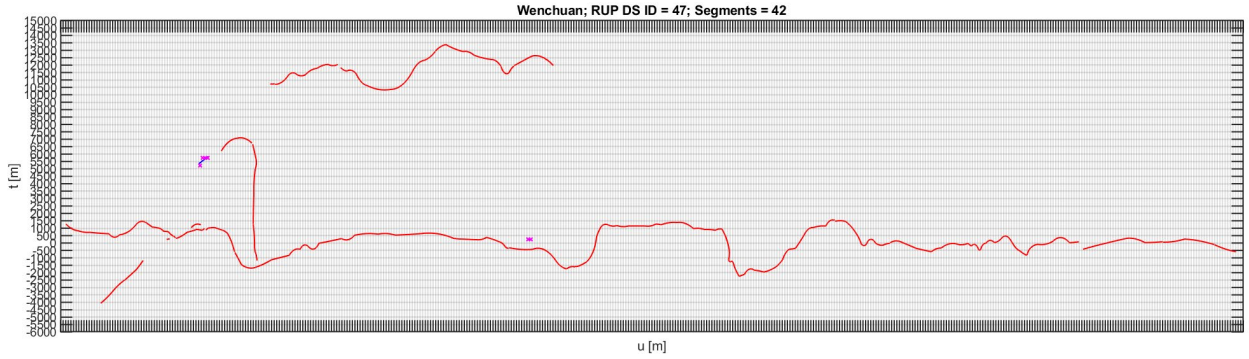

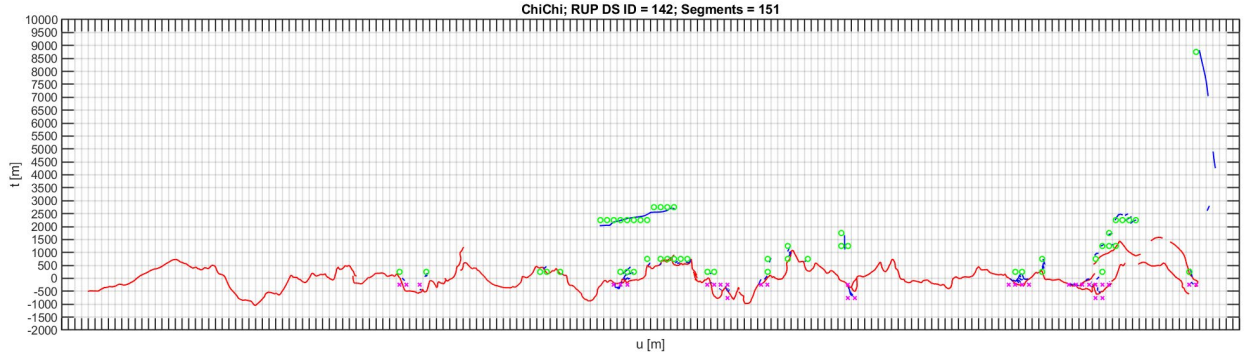

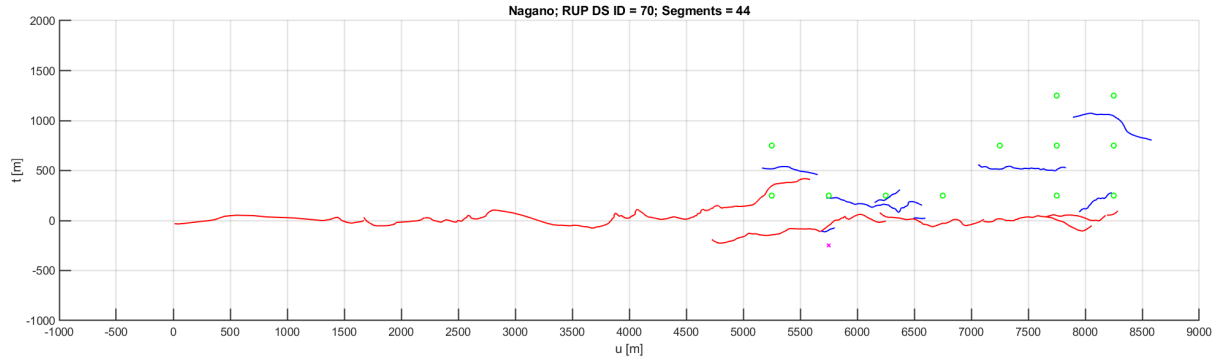
Nagano; RUP DS ID = 70; Segments = 44
t [m]
u [m]

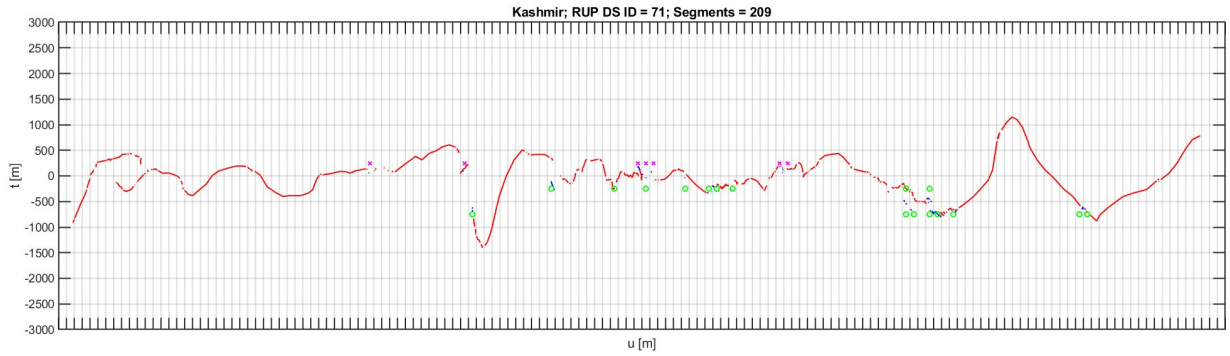
Kashmir; RUP DS ID = 71; Segments = 209
t [m]
u [m]

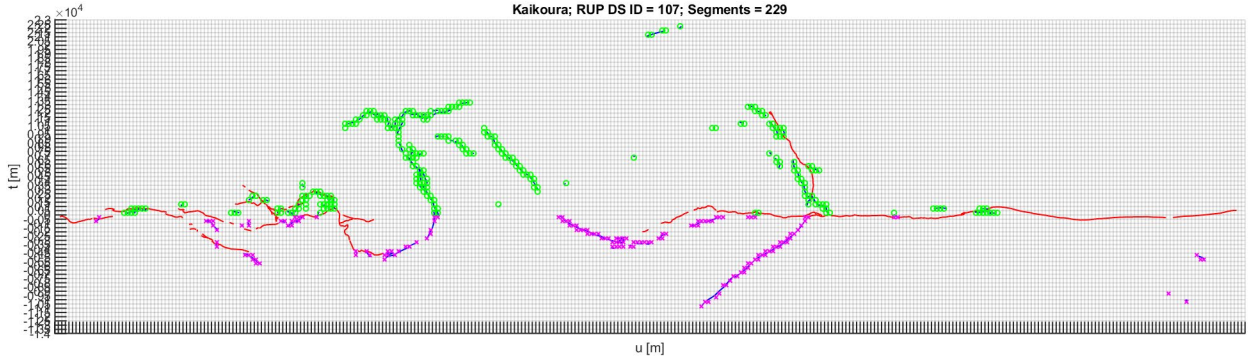
Kaikoura; RUP DS ID = 107; Segments = 229
t [m]
u [m]

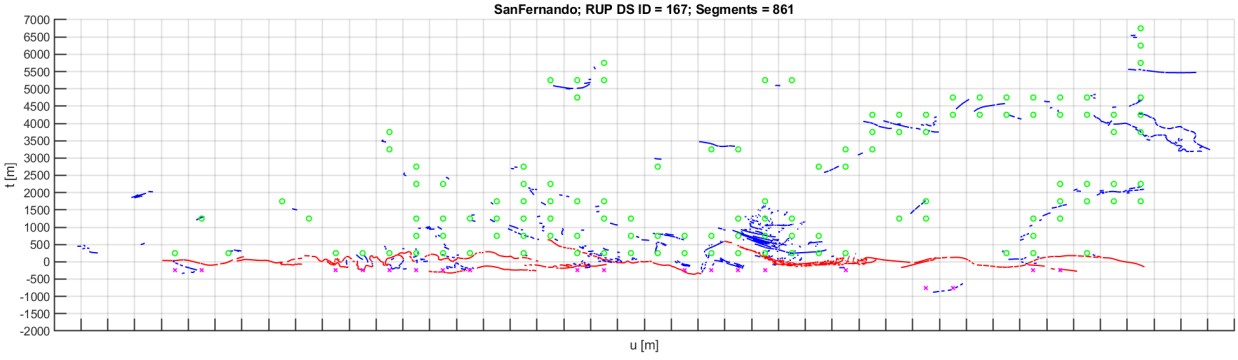
SanFernando; RUP DS ID = 167; Segments = 861
t [m]
u [m]

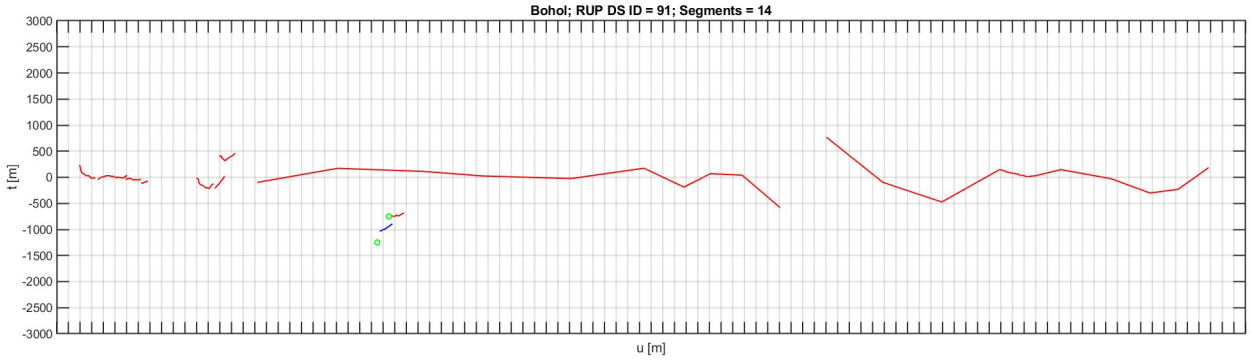
Bohol; RUP DS ID = 91; Segments = 14
t [m]
u [m]

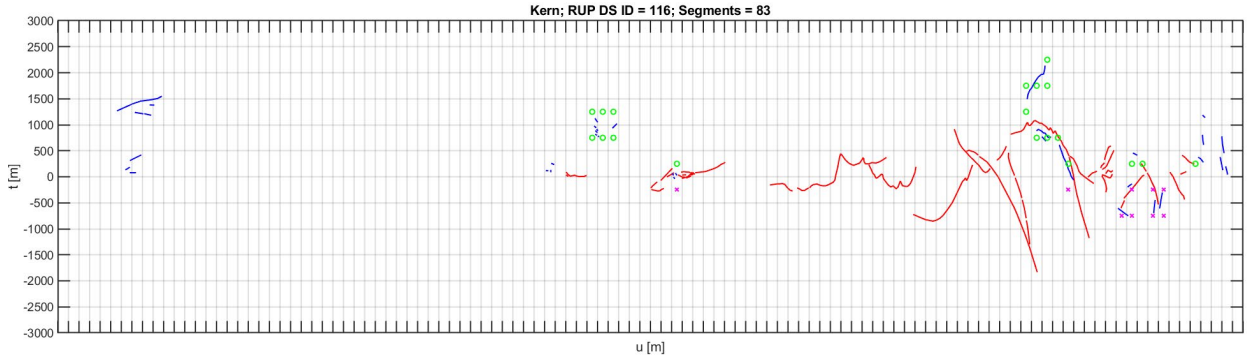
Kern; RUP DS ID = 116; Segments = 83
t [m]
u [m]

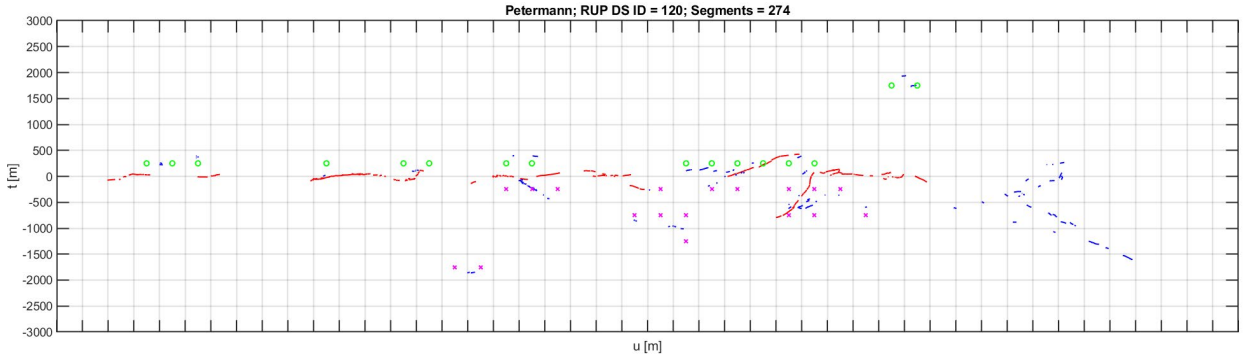
Petermann; RUP DS ID = 120; Segments = 274
t [m]
u [m]

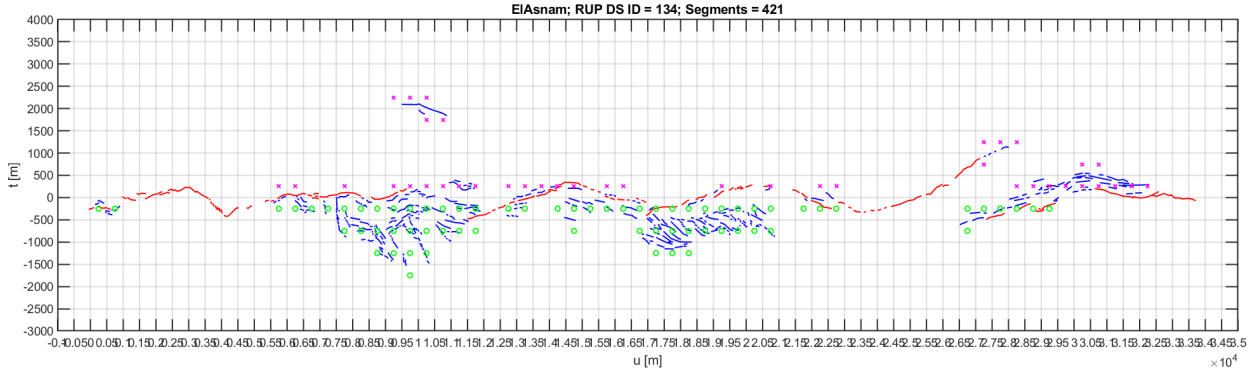
ElAsnam; RUP DS ID = 134; Segments = 421
t [m]
u [m]
×10^4

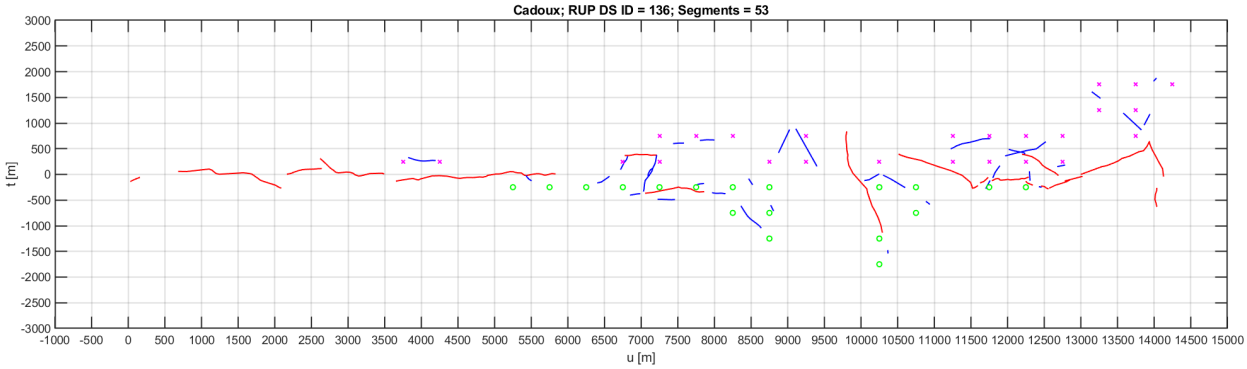
Cadoux; RUP DS ID = 136; Segments = 53
t [m]
u [m]

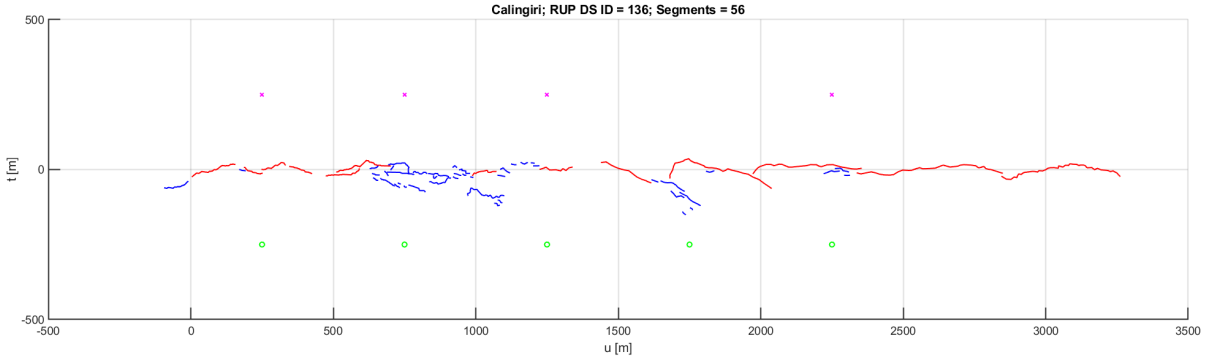
Calingiri; RUP DS ID = 136; Segments = 56
t [m]
u [m]

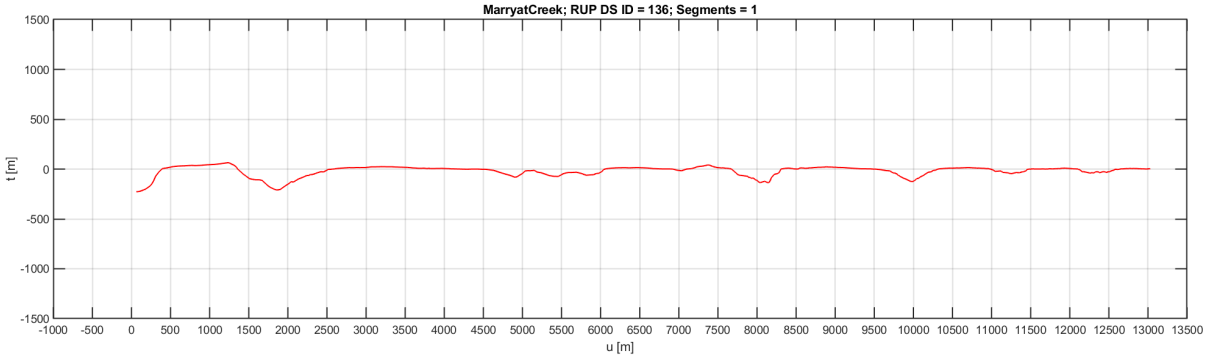
MarryatCreek; RUP DS ID = 136; Segments = 1
t [m]
u [m]

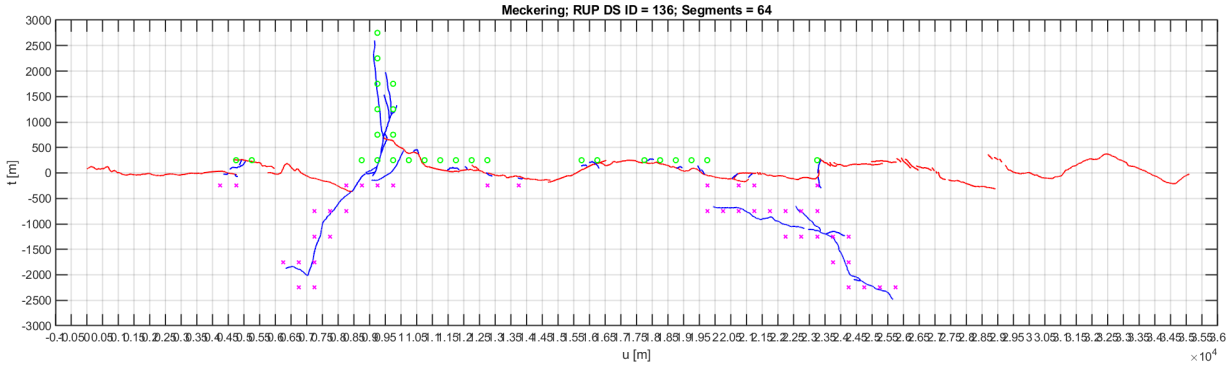
Meckering; RUP DS ID = 136; Segments = 64
t [m]
u [m]

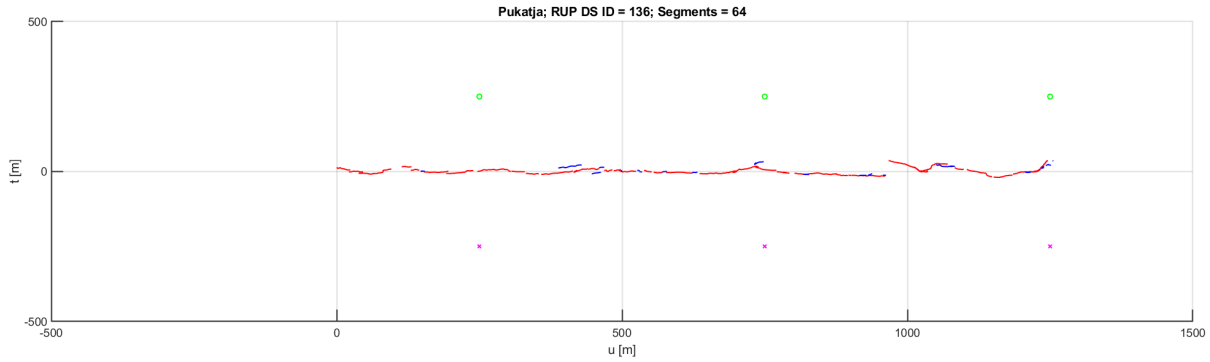
Pukatja; RUP DS ID = 136; Segments = 64
t [m]
u [m]

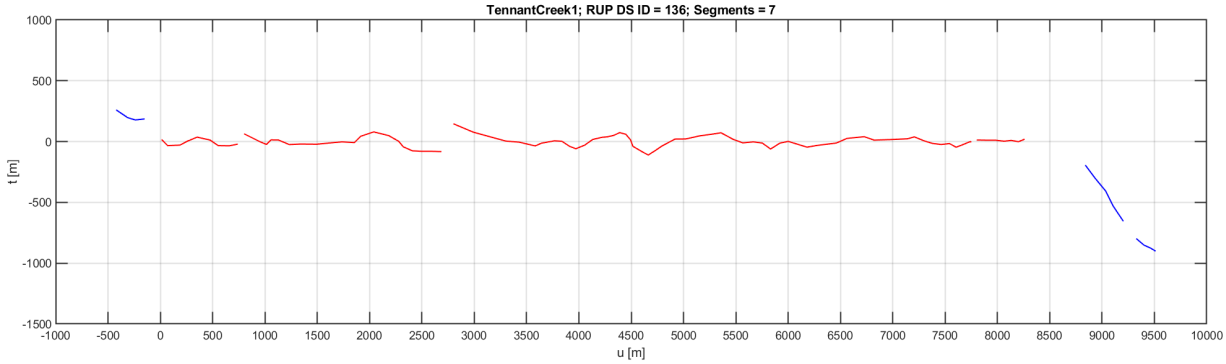
TennantCreek1; RUP DS ID = 136; Segments = 7
t [m]
u [m]

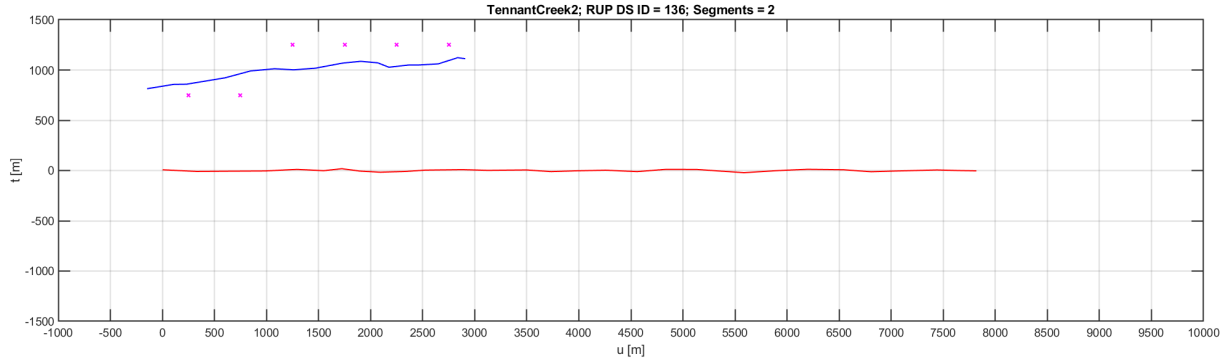
TennantCreek2; RUP DS ID = 136; Segments = 2
t [m]
u [m]

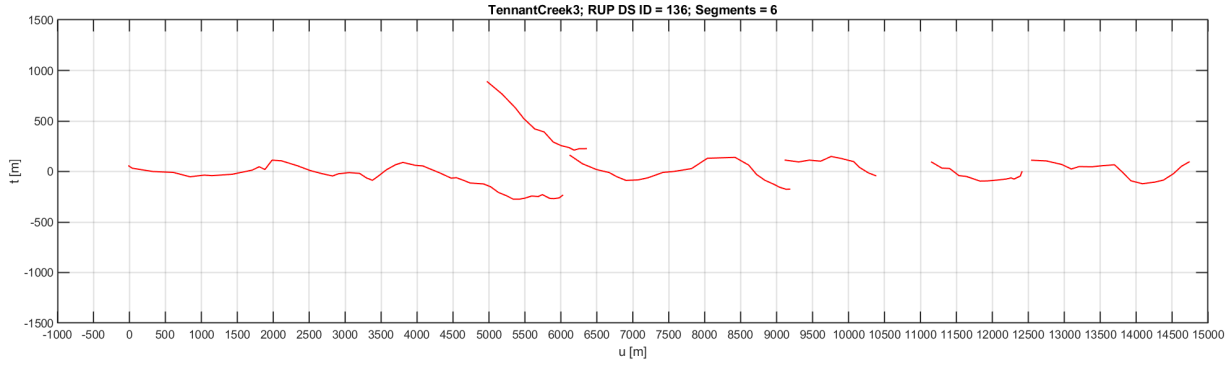
TennantCreek3; RUP DS ID = 136; Segments = 6
t [m]
u [m]

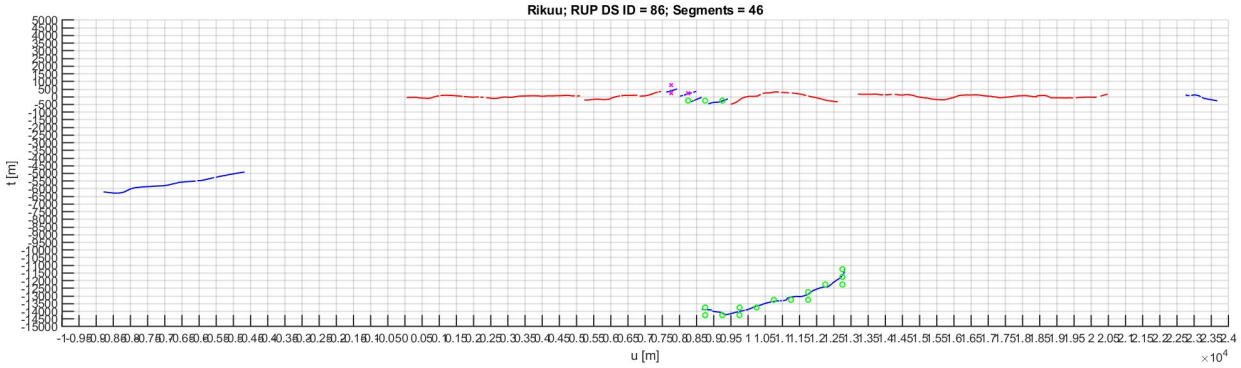
Rikuu; RUP DS ID = 86; Segments = 46
t [m]
u [m]
×10^4

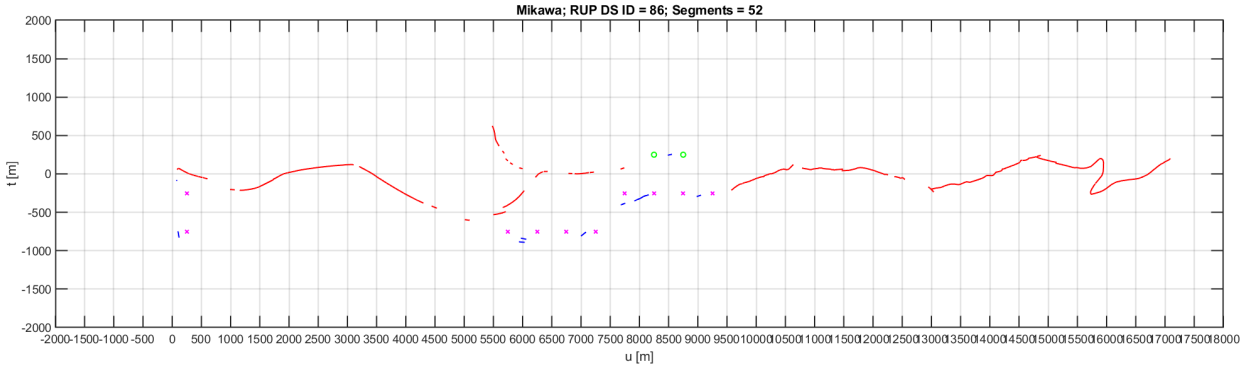
Mikawa; RUP DS ID = 86; Segments = 52
t [m]
u [m]

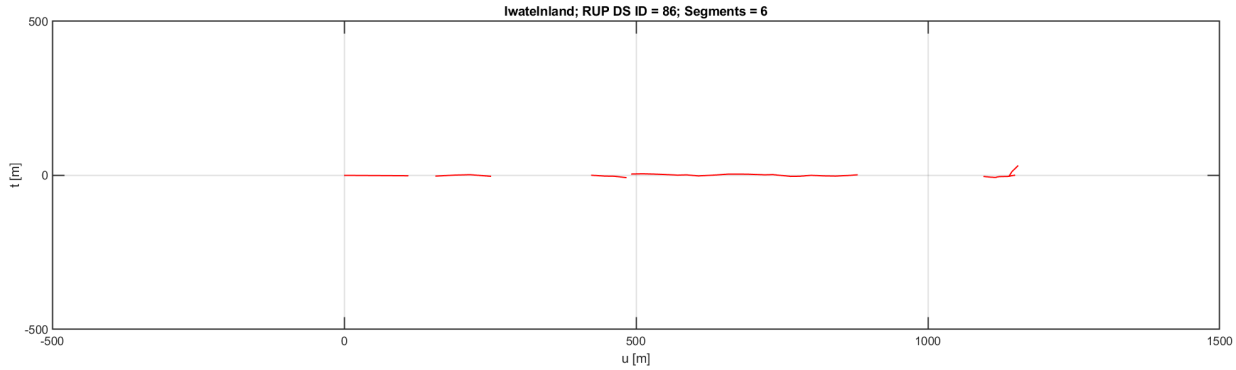
IwateInland; RUP DS ID = 86; Segments = 6
t [m]
u [m]

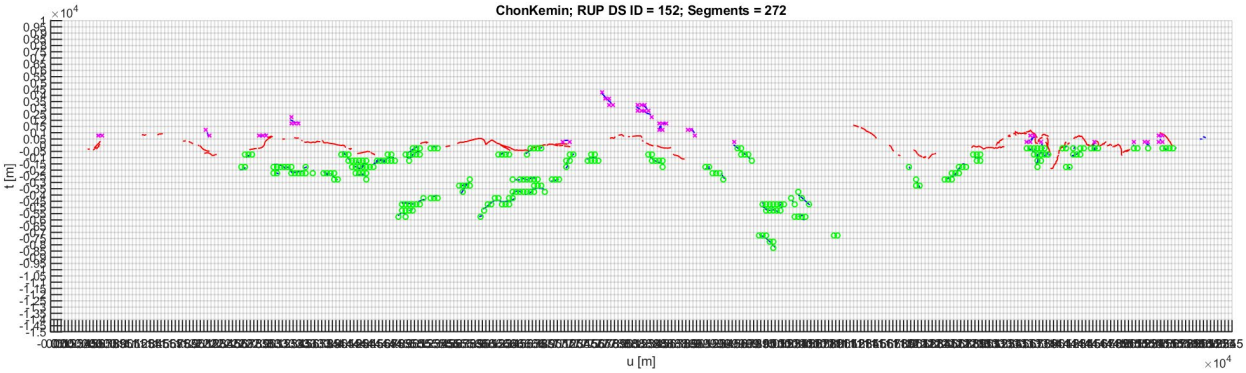
ChonKemin; RUP DS ID = 152; Segments = 272
×10^4
t [m]
u [m]
×10^4

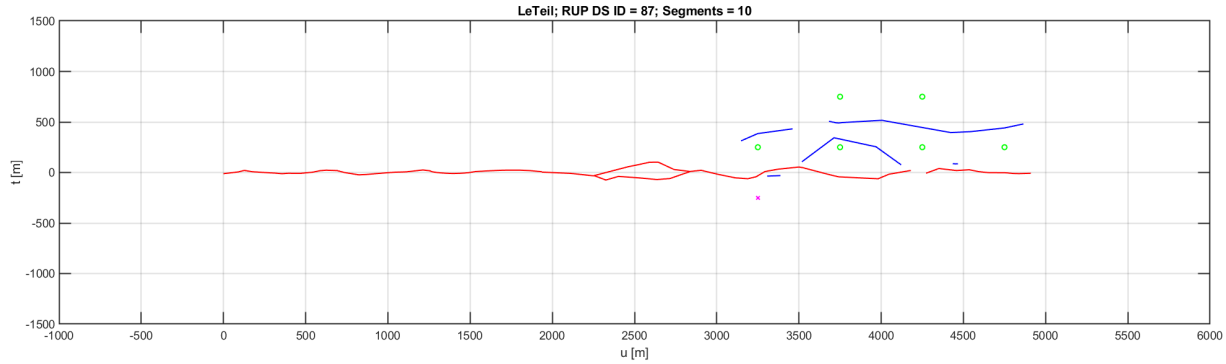
LeTeil; RUP DS ID = 87; Segments = 10
t [m]
u [m]

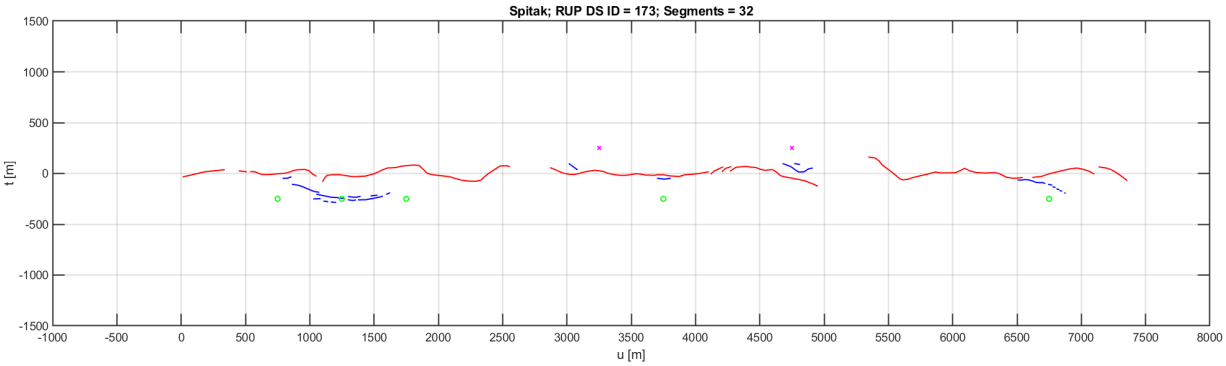
Spitak; RUP DS ID = 173; Segments = 32
t [m]
u [m]

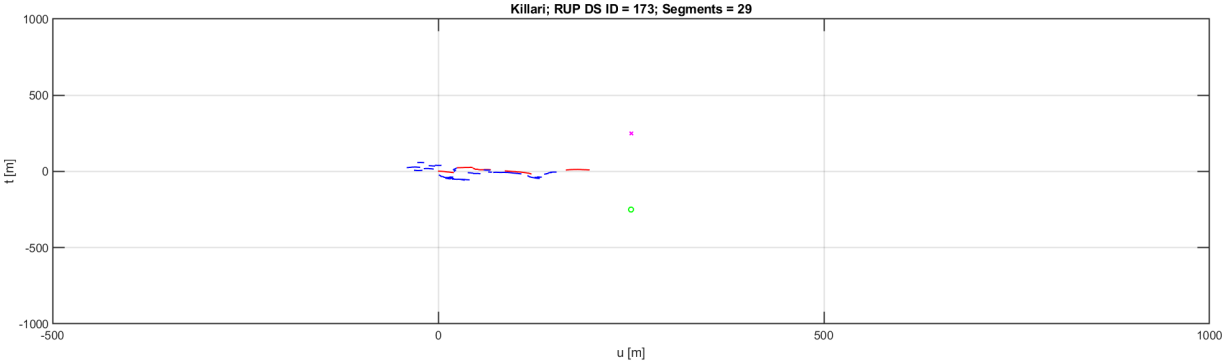
Killari; RUP DS ID = 173; Segments = 29
t [m]
u [m]

Appendix C

The following appendix contains the PFDHA code for calculating hazard curves for average displacement (AD), maximum displacement (MD), and distributed displacement (d). The code is all written in MatLab and requires the Statistics and Machine Learning Toolbox.

Average Displacement (AD)

```
% Probabilistic Fault Displacement Hazard Analysis (PFDHA)
% Moss et al procedure for Average Displacement
% Last updated 12/18/23

clear all; close all; clc;

tic
disp(' ');
disp('computing.....please wait');

%b-value for the regional seismotectonics
b_value = 0.8;

%shear modulus in dyne/cm^2
shear_modulus = 3.75*10^11;

%magnitude range for fault
min_mag = 5.0;
max_mag = 7.0;

%Length/Width in km of fault
length = 44;
width =  14;

area = length*(1000*100)*width*(1000*100); %in cm^2

%shear wave velocity of the near surface material
vs30=700;

%location of interest along fault
%this has been descritized into 50 increments so a normalized bin range of
%0 to 0.1 equates to xL_min=1 and xL_max=10, for a bin range of 0.4 to 0.5
%equates to xL_min=41 and xL_max=50...
xL_min=21;
xL_max=30;
```

```
%slip rate in cm/year back calculated from IAEA rate (eq_yr) that was given
%in research request and needs to be entered below
%eq_yr=1*10^-3;

%Mo_eq=10^((3/2)*(max_mag+10.7)); %back calculating the seismic moment
%slip_rate = (Mo_eq * eq_yr) / (shear_modulus * area); %cm/yr

slip_rate=0.05; %cm/year

%The Truncated Exponential model is used to account for the variability in
%earthquake magnitudes
mag = 1 : 1 : 251;

%magnitude range for this particular problem (0.01 bins)
beta = log(10)*b_value;

%number of simulations
sim=10000;

%probability density function for truncated exponential
f_m = beta * exp(-beta * (5+(2/250) * (mag - 1) - min_mag)) / (1-exp(-beta * (max_mag-min_mag)));

dm = 0.008;
dr = 0.01;

denom = 0;

for s = 1 : 1 : 250

denom = ( f_m(s) * 10^(1.5 * (5+(2/250) * (s - 1)) + 16.05) + f_m(s + 1) * 10^(1.5 * (5+(2/250) * (s)) +
16.05) )* dm/2 + denom;

end

N_m_min = shear_modulus*area*slip_rate / denom;


%The probability of displacement can be expressed as a function of two
%probabilities   P(D>d|M,r) = P(Slip|M,r)*P(D>d|M,r,Slip)

%The first term is the probability that fault displacement will occur given
%that an earthquake has occurred P(Slip|M,r) is modeled using the following
%function per Youngs et al. equation 4:
%P(Slip|M,r)= exp(f(x)) / (1+ exp(f(x)) where f(x)=a+bM from regression
%Youngs et al found that for all events world wide they analyzed the coefficients
%were a = -12.51 and b = 2.053
%prn = exp(a + b * (5+(2/250) * (mag-1)));
%prd = 1 + exp(a + b * (5+(2/250) * (mag-1)));
```

```
%pr_slip = prn ./ prd ;

%The logistic regression results specific to reverse events from Moss & Ross
%2011 BSSA are in the form of the logistic function:
%P(Slip|M,r)= 1/(1+exp(f(x)) where f(x) is the same as above.

%a=7.3;
%b=-1.03;
%pr_slip = 1./ (1 + exp(a + b * (5+(2/250) * (mag-1))));

%The logistic regression results were improved upon in Moss et al 2013 and
%an additional variable was added, VS30 of the projection of the
%rupture plane from depth.  The logistic equation is the same but the
%fuction now includes VS30 as a predictor: P(Slip|M,r,VS30)=1/(1+exp(-z))
%where z=-13.9745+2.1395*M for VS30>600m/s "stiff" materials
%      z=-6.2548+0.8308*M  for VS30<600m/s "soft" materials

if vs30>600
pr_slip = 1./(1 + exp(-(-13.9745 + 2.1395 * (5+(2/250) * (mag-1)))));
else
pr_slip = 1./(1 + exp(-(-6.2548 + 0.8308 * (5+(2/250) * (mag-1)))));
end


%The second term in the probability of displacement defines the conditional
%distribution of the amount of fault displacement given that slip has
%occurred.  This term is analogous to an attenuation relationship and is
%constructed using empirical data.  We want a distribution that captures
%the variability of fault displacement at the site with respect to the
%entire rupture.

%We are choosing to proceed here via Monte Carlo integration, the output of
%which will be inserted into the double integral over m and r to obtain the
%final probabilities.

%There are two terms here, the probability of D/MD or D/AD at any location
%and the probability of MD or AD.  An empirical fit cumulative gamma
%distribution maps the P(D/AD) for a given x/L ratio, which is convolved
%with the P(AD) or P(MD) to arrive at the conditional probability of D.

%We now solve for the rupture displacement where the variable is treated as
%lognormally distributed.

%m will go from 1 to 251, therefore the magnitude itself will range from
%5-7 based on the scaling relation specified below.  r will vary from 1 to
%51 and therefore vary x/L from 0 to 0.5, based on scaling relation specified
%below.
```

```
nu = zeros(28, 2);


probDd = zeros(51, 251, 28);


for m = 1 : 1 : 251 %this gives the mag bins from 5-7


   for r = 1 : 1 : 51 %this gives the x/L bins from 0 to 0.5 with
                      %the range for r=1:1:51 with the start value,
                      %increment, and end value

      %this part creates a monte carlo for a given value of m and x

      %A is the Prob(AD|M) from linear regression (compared to Wells and
      %Coppersmith regression) 0.148 * 2.302 is the standard deviation


      %B is the Prob(D/AD|M,r) from statistical fitting of gamma

      A = trlnrnd(mu((5+(2/250) * (m - 1))) , 0.148*2.302, sim);

      B = gamrnd(a_gam(0.5*(r - 1)/50), b_gam(0.5*(r - 1)/50), 1, sim);


      %This next line takes a product of the random variables A and B
      %stated above.  It is computed by simply multiplying element n of A
      %by element n of B to form combine(n).  This provides the product
      %of P(AD)*P(D/AD)

      combine = A.*B;


      %here a histogram is created from the data after the product of
      %random variables has occurred, with 1000 bins as the default.

      [n, Dbin] = hist(combine, 1000);

      cdf = zeros(1000,1);

      %CDF is created here by summing up bin weight from the left and
      %normalizing by total number of data points.

      cdf(1) = n(1);


      for u = 2:1:1000
```

```
    cdf(u) = n(u) + cdf(u-1);

end

invcdf = 1 - cdf/cdf(1000);


%This is now the inv_CDF for a given value of x and m, but we need
%to pull a specific value from it at d.  This wil be done by a
%difference algorithm to grab the right value. The sensitivity is
%set to 0.01

%d is just a dummy index

d = 1;


%Here we set the range for the values of displacement we want.
%Each value of D will yield a new rate of events exceeding D, so
%the output of this PFDHA will yield nu(D).

v = 0.01;


D = 0.01;


while D <= 10

    nu(d, 1) = D;

    %1000 is the last index in the CDF array.  therefore the next
    %loop goes up until 1000.  It looks at every element of the
    %Dbin array and subtracts that value from the value of D
    %specified above.  If the difference is less than the
    %sensitivity of 0.01, it pulls that value out of the array and
    %sticks it in our new discrete inverted CDF for D > D.

    for i = 1 : 1 : 1000

        AA = D - Dbin(i);

            if abs(AA) < 0.01

                probDd(r, m, d) = invcdf(i, 1);
                break
```

```
        end

      % This clause in the for loop executes if the difference
      % algorithm has failed.  In other words, if no value of D
      % is found to satisfy the sensitivity algorithm it
      % Calls a spline based interpolation function--but first
      % checks to see if D is larger than the bounds of Dbin.
      % If so it forces the probability to be zero, otherwise it
      % interpolates.

        if i == 1000

          if D > max(Dbin)

            probDd(r, m, d) = 0;

          else

            probDd(r, m, d) = interp1(Dbin, invcdf, D, 'spline');

          end

        end

    end


    %incrementing the dummy index

d = d + 1;
D = D + v;


    if D <= 0.9 && D > 0.09


      v=0.1;


    end


    if D > 0.9
```

```
            v=1;

        end

    end

  end

end

    %probDd now is a full Matrix.  Since we have complete arrays for
    %all three probability terms in the PFDHA integral, we now proceed to
    %calculate the rate of events per year which exceed a given value of D.

    %initializing nu to 0 before sum.

    %250 blocks here instead of 251 since there are 251 points and 250
    %actual rectangular volumes to integrate over.


%dd here is set to a maximum of 10 different values of D to compute nu for
%if number of D values specified above is less than 10, the remainder will
%show up as nu = 0 in the terminal.


%dd is a dummy index for a specific place in the prob(D>d) array.  it will
%go from 1 to 10 and each index corresponds to the probability for a given
%value of D from above.  So if D above went from 0.01 : 0.01 : 0.1, dd = 1
%would be D = 0.01, dd = 2 is D = 0.02, and so forth.


for dd = 1 : 1 : 28

    disp('.')

    %initializing nu as zero before sum starts
    rate = 0;

    for mm = 1 : 1 : 250 % magnitude range discretized into 205 increments
```

```
        for rr = xL_min : 1 : xL_max % x/L range discretized into 50 increments with
                                     % with full range of 1:1:50

            %here averaging over 4 square distanced datapoints and
            %discretely computing the integral (sum)

            rate = N_m_min*((f_m(mm) * probDd(rr, mm, dd) * pr_slip(mm) + f_m(mm) * probDd(rr+1, mm, dd)
* pr_slip(mm) + f_m(mm+1) * probDd(rr+1, mm+1, dd) * pr_slip(mm+1) + f_m(mm+1) * probDd(rr, mm+1,
dd) * pr_slip(mm+1))/4) * dm * dr + rate;


        end


    end

    nu(dd, 2) = rate;
    rate;

end


loglog(nu(:,1), nu(:,2))
xlabel('Displacment (m)')
ylabel('Annual Probability of Exceedance')
axis('tight');
set(gca,'FontSize',16,'FontWeight','bold')
grid on;
toc
```

```
function a_gamout = a_gam(xL)

a_gamout = 4.2797*xL + 1.6216;

end

%this is the a term in the gamma distribution fit to D/AD data
```

```
function b_gamout = b_gam(xL)

b_gamout = -0.5003*xL + 0.5133;

end
```

```
%this is the b term in the gamma distribution fit to the D/AD data

-----------------------------------------------------------------------------------------------------------

function muout = mu(mag)
a_AD = -2.87;
b_AD = 0.416;
muout = log(10^(a_AD + b_AD*mag));
end

%this is the a and b linear regression terms for P(AD|M,r)
%for all data in Mea21 the equation is log10(AD)=0.39871*Mw-2.75606
%for FDHI data only the equation becomes log10(AD)=0.4395*Mw-3.0396
%Note: there is virtually no difference in these equations

%for complete rupture in Mea22          log10(AD)=0.416*Mw-2.87

-----------------------------------------------------------------------------------------------------------

function truncout = trlnrnd(mu, sigma, n)
%monte carlo sampling for a truncated lognormal distribution.  zmax is the
%maximum value where truncation occurs, here it is specified as AD = 15m.
%n random numbers between 0 and zmax are generated and thrown into the
%Inverted CDF for a truncated lognormal distribution, then pass them back.

z = unifrnd(0, 1, 1, n);

%truncout = exp(sqrt(2*sigma*sigma)*erfinv(2*z*(logncdf(log(15), mu, sigma)) - 1) + mu);

epsilon_max=5;

cdf_min=logncdf(exp(mu-epsilon_max*sigma),mu,sigma);

cdf_max=logncdf(exp(mu+epsilon_max*sigma),mu,sigma);

truncout=exp(sigma*sqrt(2)*erfinv(2*(z-0.5)*(cdf_max-cdf_min))+mu);

end

-----------------------------------------------------------------------------------------------------------

-----------------------------------------------------------------------------------------------------------
```

Maximum Displacement (MD)

```
% Probabilistic Fault Displacement Hazard Analysis (PFDHA)
% Moss et al procedure for Maximum Displacement
% Last updated 12/18/23

clear all; close all; clc;

tic
disp(' ');
disp('computing.....please wait');

%b-value for the regional seismotectonics
b_value = 0.8;

%shear modulus in dyne/cm^2
shear_modulus = 3.75*10^11;

%magnitude range for fault
min_mag = 5.0;
max_mag = 7.5;

%Length/Width in km of fault
length = 100;
width =  15;

area = length*(1000*100)*width*(1000*100); %in cm^2

%shear wave velocity of the near surface material
vs30=700;

%location of interest along fault
%this has been descritized into 50 increments so a normalized bin range of
%0 to 0.1 equates to xL_min=1 and xL_max=10, for a bin range of 0.4 to 0.5
%equates to xL_min=41 and xL_max=50...
xL_min=41;
xL_max=50;

%slip rate in cm/year back calculated from IAEA rate (eq_yr) that was given
%in research request and needs to be entered below
%eq_yr=1*10^-3;

%Mo_eq=10^((3/2)*(max_mag+10.7)); %back calculating the seismic moment
```

```
%slip_rate = (Mo_eq * eq_yr) / (shear_modulus * area); %cm/yr
slip_rate= 0.5; %cm/yr

%The Truncated Exponential model is used to account for the variability in
%earthquake magnitudes
mag = 1 : 1 : 251;

%magnitude range for this particular problem (0.01 bins)
beta = log(10)*b_value;

%number of simulations
sim=10000;

%probability density function for truncated exponential
f_m = beta * exp(-beta * (5+(2/250) * (mag - 1) - min_mag)) / (1-exp(-beta * (max_mag-min_mag)));

dm = 0.008;
dr = 0.01;

denom = 0;

for s = 1 : 1 : 250

denom = ( f_m(s) * 10^(1.5 * (5+(2/250) * (s - 1)) + 16.05) + f_m(s + 1) * 10^(1.5 * (5+(2/250) * (s)) +
16.05) )* dm/2 + denom;

end

N_m_min = shear_modulus*area*slip_rate / denom;


%The probability of displacement can be expressed as a function of two
%probabilities   P(D>d|M,r) = P(Slip|M,r)*P(D>d|M,r,Slip)

%The first term is the probability that fault displacement will occur given
%that an earthquake has occurred P(Slip|M,r) is modeled using the following
%function per Youngs et al. equation 4:
%P(Slip|M,r)= exp(f(x)) / (1+ exp(f(x)) where f(x)=a+bM from regression
%Youngs et al found that for all events world wide they analyzed the coefficients
%were a = -12.51 and b = 2.053
%prn = exp(a + b * (5+(2/250) * (mag-1)));
%prd = 1 + exp(a + b * (5+(2/250) * (mag-1)));
%pr_slip = prn ./ prd ;

%The logistic regression results specific to reverse events from Moss & Ross
%2011 BSSA are in the form of the logistic function:
%P(Slip|M,r)= 1/(1+exp(f(x)) where f(x) is the same as above.
```

```
%a=7.3;
%b=-1.03;
%pr_slip = 1./ (1 + exp(a + b * (5+(2/250) * (mag-1))));

%The logistic regression results were improved upon in Moss et al 2013 and
%an additional variable was added, VS30 of the projection of the
%rupture plane from depth.  The logistic equation is the same but the
%fuction now includes VS30 as a predictor: P(Slip|M,r,VS30)=1/(1+exp(-z))
%where z=-13.9745+2.1395*M for VS30>600m/s "stiff" materials
%      z=-6.2548+0.8308*M  for VS30<600m/s "soft" materials

if vs30>600
pr_slip = 1./(1 + exp(-(-13.9745 + 2.1395 * (5+(2/250) * (mag-1)))));
else
pr_slip = 1./(1 + exp(-(-6.2548 + 0.8308 * (5+(2/250) * (mag-1)))));
end


%The second term in the probability of displacement defines the conditional
%distribution of the amount of fault displacement given that slip has
%occurred.  This term is analogous to an attenuation relationship and is
%constructed using empirical data.  We want a distribution that captures
%the variability of fault displacement at the site with respect to the
%entire rupture.

%We are choosing to proceed here via Monte Carlo integration, the output of
%which will be inserted into the double integral over m and r to obtain the
%final probabilities.

%There are two terms here, the probability of D/MD or D/AD at any location
%and the probability of MD or AD.  An empirical fit cumulative gamma
%distribution maps the P(D/AD) for a given x/L ratio, which is convolved
%with the P(AD) or P(MD) to arrive at the conditional probability of D.

%We now solve for the rupture displacement where the variable is treated as
%lognormally distributed.

%m will go from 1 to 251, therefore the magnitude itself will range from
%5-7 based on the scaling relation specified below.  r will vary from 1 to
%51 and therefore vary x/L from 0 to 0.5, based on scaling relation specified
%below.

nu = zeros(28, 2);


probDd = zeros(51, 251, 28);
```

```
for m = 1 : 1 : 251 %this gives the mag bins from 5-7

   %disp('.')

   for r = 1 : 1 : 51 %this gives the x/L bins from 0 to 0.5 with
                      %the range for r=1:1:51 with the start value,
                      %increment, and end value


      %this part creates a monte carlo for a given value of m and x

      %A is the Prob(MD|M) from linear regression (compared to Wells and
      %Coppersmith regression) 0.133 * 2.302 is the standard deviation

      %B is the Prob(D/MD|M,r) from statistical fitting of gamma or
      %weibull distributions

      A = trlnrnd(mu((5+(2/250) * (m - 1))) , 0.133*2.302, sim);

      B = gamrnd(a_gam(0.5*(r - 1)/50), b_gam(0.5*(r - 1)/50), 1, sim);

      B(B>=1)=1; %truncating the gamma distribution

      %This next line takes a product of the random variables A and B
      %stated above.  It is computed by simply multiplying element n of A
      %by element n of B to form combine(n).  This provides the product
      %of P(MD)*P(D/MD)

      combine = A.*B;


      %here a histogram is created from the data after the product of
      %random variables has occurred, with 1000 bins as the default.

      [n, Dbin] = hist(combine, 1000);

      cdf = zeros(1000,1);

      %CDF is created here by summing up bin weight from the left and
      %normalizing by total number of data points.

      cdf(1) = n(1);


      for u = 2:1:1000

         cdf(u) = n(u) + cdf(u-1);
```

```
end

invcdf = 1 - cdf/cdf(1000);


%This is now the inv_CDF for a given value of x and m, but we need
%to pull a specific value from it at d.  This wil be done by a
%difference algorithm to grab the right value. The sensitivity is
%set to 0.01

%d is just a dummy index

d = 1;


%Here we set the range for the values of displacement we want.
%Each value of D will yield a new rate of events exceeding D, so
%the output of this PFDHA will yield nu(D).

v = 0.01;


D = 0.01;


while D <= 10

   nu(d, 1) = D;

   %1000 is the last index in the CDF array.  therefore the next
   %loop goes up until 1000.  It looks at every element of the
   %Dbin array and subtracts that value from the value of D
   %specified above.  If the difference is less than the
   %sensitivity of 0.01, it pulls that value out of the array and
   %sticks it in our new discrete inverted CDF for D > D.

   for i = 1 : 1 : 1000

      AA = D - Dbin(i);

         if abs(AA) < 0.01

            probDd(r, m, d) = invcdf(i, 1);
            break

         end
```

```
        % This clause in the for loop executes if the difference
        % algorithm has failed.  In other words, if no value of D
        % is found to satisfy the sensitivity algorithm it
        % Calls a spline based interpolation function--but first
        % checks to see if D is larger than the bounds of Dbin.
        % If so it forces the probability to be zero, otherwise it
        % interpolates.

          if i == 1000

            if D > max(Dbin)

               probDd(r, m, d) = 0;

            else

               probDd(r, m, d) = interp1(Dbin, invcdf, D, 'spline');

            end

          end

    end


    %incrementing the dummy index

d = d + 1;
D = D + v;


    if D <= 0.9 && D > 0.09


       v=0.1;


    end



    if D > 0.9


       v=1;
```

```
        end


    end

  end


end


  %probDd now is a full Matrix.  Since we have complete arrays for
  %all three probability terms in the PFDHA integral, we now proceed to
  %calculate the rate of events per year which exceed a given value of D.

  %initializing nu to 0 before sum.

  %250 blocks here instead of 251 since there are 251 points and 250
  %actual rectangular volumes to integrate over.


%dd here is set to a maximum of 10 different values of D to compute nu for
%if number of D values specified above is less than 10, the remainder will
%show up as nu = 0 in the terminal.


%dd is a dummy index for a specific place in the prob(D>d) array.  it will
%go from 1 to 10 and each index corresponds to the probability for a given
%value of D from above.  So if D above went from 0.01 : 0.01 : 0.1, dd = 1
%would be D = 0.01, dd = 2 is D = 0.02, and so forth.


for dd = 1 : 1 : 28

  disp('.')

  %initializing nu as zero before sum starts
  rate = 0;

  for mm = 1 : 1 : 250 % magnitude range discretized into 205 increments


    for rr = xL_min : 1 : xL_max % x/L range discretized into 50 increments with
                          % with full range of 1:1:50
```

```
        %here averaging over 4 square distanced datapoints and
        %discretely computing the integral (sum)

        rate = N_m_min*((f_m(mm) * probDd(rr, mm, dd) * pr_slip(mm) + f_m(mm) * probDd(rr+1, mm, dd)
* pr_slip(mm) + f_m(mm+1) * probDd(rr+1, mm+1, dd) * pr_slip(mm+1) + f_m(mm+1) * probDd(rr, mm+1,
dd) * pr_slip(mm+1))/4) * dm * dr + rate;


      end


   end

   nu(dd, 2) = rate;
   rate;

end


loglog(nu(:,1), nu(:,2))
xlabel('Displacment (m)')
ylabel('Annual Probability of Exceedance')
axis('tight');
set(gca,'FontSize',16,'FontWeight','bold')
grid on;
toc
```

```
function a_gamout = a_gam(xL)

a_gamout = 1.4244*xL + 1.856;

end

%this is the a term in the gamma distribution fit to D/MD data
```

```
function b_gamout = b_gam(xL)

b_gamout = -0.0832*xL +0.1994;

end

%this is the b term in the gamma distribution fit to the D/MD data
```

```
function muout = mu(mag)
a_MD = -2.5;
b_MD = 0.415;
sigma_mu = 0.148;  %add sigmas for non-median values
muout = log(10^(a_MD + b_MD*mag + sigma_mu));
end

%this is the a and b linear regression terms for P(MD|M,r)
%for all data in Mea22 the equation is  log10(MD)=0.40126*Mw-2.59939
%for FDHI data only in Mea22 it becomes log10(MD)=0.48150*Mw-2.9305
%for complete rupture in Mea22 it becomes log10(MD)=0.415*Mw-2.50
%for non-median values log10(MD)=0.415*Mw-2.5+(#sigmas*0.148)
```

```
function truncout = trlnrnd(mu, sigma, n)

%monte carlo sampling for a truncated lognormal distribution.  zmax is the
%maximum value where truncation occurs, here it is specified as MD = 15m.
%n random numbers between 0 and zmax are generated and thrown into the
%Inverted CDF for a truncated lognormal distribution, then pass them back.

z = unifrnd(0, 1, 1, n);

%truncout = exp(sqrt(2*sigma*sigma)*erfinv(2*z*(logncdf(log(15), mu, sigma)) - 1) + mu);

epsilon_max=5;  %based on DBA's corrections 9/14/23

cdf_min=logncdf(exp(mu-epsilon_max*sigma),mu,sigma);

cdf_max=logncdf(exp(mu+epsilon_max*sigma),mu,sigma);

truncout=exp(sigma*sqrt(2)*erfinv(2*(z-0.5)*(cdf_max-cdf_min))+mu);


end
```

Distributed Displacement (d)

```
% Probabilistic Fault Displacement Hazard Analysis (PFDHA)
% Moss et al for distributed or off-fault displacement
% Last revised 12/18/23

clear all; close all; clc;

tic
disp(' ');
disp('computing.....please wait');

%b-value for the regional seismotectonics
b_value = 0.8;

%shear modulus in dyne/cm^2
shear_modulus = 3.75*10^11;

%magnitude range for fault
min_mag = 5.0;
max_mag = 7.5;

%Length/Width in km of fault
length = 100;
width =  15;

area = length*(1000*100)*width*(1000*100); %in cm^2

%shear wave velocity of the near surface material
%stiff>600m/s soft<600m/s
vs30=700;

%location of interest along fault
%this has been descritized into 50 increments so a normalized bin range of
%0 to 0.1 equates to xL_min=1 and xL_max=10, for a bin range of 0.4 to 0.5
%equates to xL_min=41 and xL_max=50...
xL_min=41;
xL_max=50;

%r_dist is the distance from fault strike in meters
%wall is the flag for hanging wall wall=1 or foot wall wall=0
%complex is the flag for simple fault (0) or complex multi-fault system (1)
```

```
%mbc is the flag for magnitude bin center mbc=7.5, or 6.5, or 5.5
r_dist=3000; %meters
wall=1;
complex=0;
mbc=7.5;

%slip rate in cm/year back calculated from IAEA rate (eq_yr) that was given
%in research request and needs to be entered below
%eq_yr=1*10^-3;

%Mo_eq=10^((3/2)*(max_mag+10.7)); %back calculating the seismic moment
%slip_rate = (Mo_eq * eq_yr) / (shear_modulus * area); %cm/yr
slip_rate= 0.5; %cm/yr

%The Truncated Exponential model is used to account for the variability in
%earthquake magnitudes
mag = 1 : 1 : 251;

%magnitude range for this particular problem (0.01 bins)
beta = log(10)*b_value;

%number of simulations
sim=10000;

%probability density function for truncated exponential
f_m = beta * exp(-beta * (5+(2/250) * (mag - 1) - min_mag)) / (1-exp(-beta * (max_mag-min_mag)));

dm = 0.008;
dr = 0.01;

denom = 0;

for s = 1 : 1 : 250

denom = ( f_m(s) * 10^(1.5 * (5+(2/250) * (s - 1)) + 16.05) + f_m(s + 1) * 10^(1.5 * (5+(2/250) * (s)) +
16.05) )* dm/2 + denom;

end

N_m_min = shear_modulus*area*slip_rate / denom;


%The probability of displacement can be expressed as a function of two
%probabilities   P(D>d|M,r) = P(Slip|M,r)*P(D>d|M,r,Slip)

%The first term is the probability that fault displacement will occur given
%that an earthquake has occurred P(Slip|M,r) is modeled using the following
%function per Youngs et al. equation 4:
```

```
%P(Slip|M,r)= exp(f(x)) / (1+ exp(f(x)) where f(x)=a+bM from regression
%Youngs et al found that for all events world wide they analyzed the coefficients
%were a = -12.51 and b = 2.053
%prn = exp(a + b * (5+(2/250) * (mag-1)));
%prd = 1 + exp(a + b * (5+(2/250) * (mag-1)));
%pr_slip = prn ./ prd ;

%The logistic regression results specific to reverse events from Moss & Ross
%2011 BSSA are in the form of the logistic function:
%P(Slip|M,r)= 1/(1+exp(f(x)) where f(x) is the same as above.

%a=7.3;
%b=-1.03;
%pr_slip = 1./ (1 + exp(a + b * (5+(2/250) * (mag-1))));

%The logistic regression results were improved upon in Moss et al 2013 and
%an additional variable was added, VS30 of the projection of the
%rupture plane from depth.  The logistic equation is the same but the
%fuction now includes VS30 as a predictor: P(Slip|M,r,VS30)=1/(1+exp(-z))
%where z=-13.9745+2.1395*M for VS30>600m/s "stiff" materials
%      z=-6.2548+0.8308*M  for VS30<600m/s "soft" materials

if vs30>600
pr_slip = 1./(1 + exp(-(-13.9745 + 2.1395 * (5+(2/250) * (mag-1)))));
else
pr_slip = 1./(1 + exp(-(-6.2548 + 0.8308 * (5+(2/250) * (mag-1)))));
end


%The second term in the probability of displacement defines the conditional
%distribution of the amount of fault displacement given that slip has
%occurred.  This term is analogous to an attenuation relationship and is
%constructed using empirical data.  We want a distribution that captures
%the variability of fault displacement at the site with respect to the
%entire rupture.

%We are choosing to proceed here via Monte Carlo integration, the output of
%which will be inserted into the double integral over m and r to obtain the
%final probabilities.

%There are two terms here, the probability of D/MD or D/AD at any location
%and the probability of MD or AD.  An empirical fit cumulative gamma
%distribution maps the P(D/AD) for a given x/L ratio, which is convolved
%with the P(AD) or P(MD) to arrive at the conditional probability of D.

%We now solve for the rupture displacement where the variable is treated as
%lognormally distributed.
```

```
%m will go from 1 to 251, therefore the magnitude itself will range from
%5-7 based on the scaling relation specified below.  r will vary from 1 to
%51 and therefore vary x/L from 0 to 0.5, based on scaling relation specified
%below.

nu = zeros(28, 2);


probDd = zeros(51, 251, 28);


for m = 1 : 1 : 251 %this gives the mag bins from 5-7

   %disp('.')

   for r = 1 : 1 : 51 %this gives the x/L bins from 0 to 0.5 with
                %the range for r=1:1:51 with the start value,
                %increment, and end value


      %this part creates a monte carlo for a given value of m and x

      %A is the Prob(MD|M) from linear regression (compared to Wells and
      %Coppersmith regression) 0.133 * 2.302 is the standard deviation

      %B is the Prob(D/MD|M,r) from statistical fitting of gamma or
      %weibull distributions

      A = trlnrnd(mu((5+(2/250) * (m - 1))) , 0.133*2.302, sim);

      B = gamrnd(a_gam(0.5*(r - 1)/50), b_gam(0.5*(r - 1)/50), 1, sim);

           B(B>=1)=1; %truncating the gamma distribution

      %This next line takes a product of the random variables A and B
      %stated above.  It is computed by simply multiplying element n of A
      %by element n of B to form combine(n).  This provides the product
      %of P(MD)*P(D/MD)

      combine = A.*B;


      %here a histogram is created from the data after the product of
      %random variables has occurred, with 1000 bins as the default.

      [n, Dbin] = hist(combine, 1000);

      cdf = zeros(1000,1);
```

```
%CDF is created here by summing up bin weight from the left and
%normalizing by total number of data points.

cdf(1) = n(1);


for u = 2:1:1000

   cdf(u) = n(u) + cdf(u-1);

end

invcdf = 1 - cdf/cdf(1000);


%This is now the inv_CDF for a given value of x and m, but we need
%to pull a specific value from it at d.  This wil be done by a
%difference algorithm to grab the right value. The sensitivity is
%set to 0.01

%d is just a dummy index

d = 1;


%Here we set the range for the values of displacement we want.
%Each value of D will yield a new rate of events exceeding D, so
%the output of this PFDHA will yield nu(D).

v = 0.01;


D = 0.01;


while D <= 10

   nu(d, 1) = D;

   %1000 is the last index in the CDF array.  therefore the next
   %loop goes up until 1000.  It looks at every element of the
   %Dbin array and subtracts that value from the value of D
   %specified above.  If the difference is less than the
   %sensitivity of 0.01, it pulls that value out of the array and
   %sticks it in our new discrete inverted CDF for D > D.

   for i = 1 : 1 : 1000
```

```
        AA = D - Dbin(i);

          if abs(AA) < 0.01

             probDd(r, m, d) = invcdf(i, 1);
             break

          end


        % This clause in the for loop executes if the difference
        % algorithm has failed.  In other words, if no value of D
        % is found to satisfy the sensitivity algorithm it
        % Calls a spline based interpolation function--but first
        % checks to see if D is larger than the bounds of Dbin.
        % If so it forces the probability to be zero, otherwise it
        % interpolates.


          if i == 1000


             if D > max(Dbin)

                probDd(r, m, d) = 0;

             else

                probDd(r, m, d) = interp1(Dbin, invcdf, D, 'spline');

             end

          end

    end



    %incrementing the dummy index

d = d + 1;
D = D + v;


    if D <= 0.9 && D > 0.09
```

```
            v=0.1;

        end

        if D > 0.9

            v=1;

        end

    end

end

end

    %probDd now is a full Matrix.  Since we have complete arrays for
    %all three probability terms in the PFDHA integral, we now proceed to
    %calculate the rate of events per year which exceed a given value of D.

    %initializing nu to 0 before sum.

    %250 blocks here instead of 251 since there are 251 points and 250
    %actual rectangular volumes to integrate over.


%dd here is set to a maximum of 10 different values of D to compute nu for
%if number of D values specified above is less than 10, the remainder will
%show up as nu = 0 in the terminal.


%dd is a dummy index for a specific place in the prob(D>d) array.  it will
%go from 1 to 10 and each index corresponds to the probability for a given
%value of D from above.  So if D above went from 0.01 : 0.01 : 0.1, dd = 1
%would be D = 0.01, dd = 2 is D = 0.02, and so forth.


for dd = 1 : 1 : 28
```

```
   disp('.')

   %initializing nu as zero before sum starts
   rate = 0;

   for mm = 1 : 1 : 250 % magnitude range discretized into 205 increments


      for rr = xL_min : 1 : xL_max % x/L range discretized into 50 increments with
                                   % with full range of 1:1:50

         %here averaging over 4 square distanced datapoints and
         %discretely computing the integral (sum)

         rate = N_m_min*((f_m(mm) * probDd(rr, mm, dd) * pr_slip(mm) + f_m(mm) * probDd(rr+1, mm, dd)
* pr_slip(mm) + f_m(mm+1) * probDd(rr+1, mm+1, dd) * pr_slip(mm+1) + f_m(mm+1) * probDd(rr, mm+1,
dd) * pr_slip(mm+1))/4) * dm * dr + rate;


      end


   end

   nu(dd, 2) = rate;
   rate;

end

%adjustment of hazard curve from MD to d which includes:
%1) the probability of occurrence term P(d>0),
%2) probability of exceedence term P(d>do), and
%3) the d/MD term for scaling

%note: wall=1 is hanging wall and wall=0 is foot wall


if wall==1 %hanging wall

  %prob nonzero for hanging wall at 85th percentile
   pd0HW = exp(-2.2 * r_dist/1000 + 0.5 );
   if pd0HW > 1.0
      pd0HW = 1.0;
   end

   if mbc==7.5
      if complex==1
```

```
          %p_r_dist=(1-((110.4*exp(-0.000032*r_dist)-107.3*exp(-0.0014*r_dist)))/100)*0.06; %hanging
wall CDF where the 0.06 is the probabilty of distributed as a function of x/L 100 m bins
          p_r_dist=(1-(0.6998*exp(2.75*10^-5*r_dist)-0.6931*exp(-0.001219*r_dist)))*pd0HW; %complex=1
       else
          r_dist_max=min(r_dist,3500); %this caps the distribution at the upper limit of the observed data
          p_r_dist=(1-(0.8298*exp(5.682*10^-5*r_dist_max)-0.8346*exp(-0.001735*r_dist_max)))*pd0HW;
%complex=0
       end

   elseif mbc==6.5
       if complex==1
          p_r_dist=(1-(0.8858*exp(6.203*10^-6*r_dist)-0.8957*exp(-0.001959*r_dist)))*pd0HW;
%complex=1
       else
          r_dist_max=min(r_dist,3500);
          p_r_dist=(1-(1.166*exp(-4.699*10^-5*r_dist_max)-1.1730*exp(-0.001539*r_dist_max)))*pd0HW;
%complex=0
       end

   elseif mbc==5.5
          r_dist_max=min(r_dist,120);
          p_r_dist=(1-(98.45*exp(0.00228*r_dist_max)-98.53*exp(-0.01417*r_dist_max)))*pd0HW;
%complex=0
   end

   %distance corresponding to exponential or random displacements
   if complex==0
      d_MD_ratio=0.43*exp(-0.4*r_dist/1000); %HW 85th percentile envelope
      %d_MD_ratio=0.35*exp(-0.091*r_dist/1000); %Youngs et al
   else
      d_MD_ratio=0.43*exp(-0.012*r_dist/1000);%complex faulting
   end

else %wall==0 foot wall

  %prob nonzero for foot wall at 85th percentile
   pd0FW = exp(-2.4 * r_dist/1000 + 0.4 );
   if pd0FW > 1.0
     pd0FW = 1.0;
   end

   if mbc==7.5
       if complex==1
          %p_r_dist=(1-((84.12*exp(0.00006*r_dist)-83.09*exp(-0.0055*r_dist)))/100)*0.02; %foot wall cdf
were the 0.02 is the probabilty of distributed as a function of x/L 100 m bins
          p_r_dist=(1-(0.1959*exp(0.0001091*r_dist)-2.202*10^08*exp(-002554*r_dist)))*pd0FW;
%complex=1
       else
```

```
            r_dist_max=min(r_dist,3500);
            p_r_dist=(1-(1.445*exp(-7.078*10^-5*r_dist_max)-1.454*exp(-0.0006972*r_dist_max)))*pd0FW;
%complex=0
        end

    elseif mbc==6.5
            r_dist_max=min(r_dist,3500);
            p_r_dist=(1-(0.9297*exp(2.515*10^-5*r_dist)-0.9233*exp(-0.01828*r_dist)))*pd0FW;  %complex=0

    else
            p_r_dist=0;
    end

    %distance corresponding to exponential or random displacements
        d_MD_ratio=0.68*exp(-0.13*r_dist/1000); %FW 85th percentile envelope
        %d_MD_ratio=0.16*exp(-0.137*r_dist/1000); %Youngs et al
end


%nu(:,1)=nu(:,1)* d_MD_ratio
%nu(:,2)=n(:,2)* p_wrz;
d_off_fault=nu(:,1)*d_MD_ratio %adjusting MD by the d/MD ratio for off-fault location
d_rate=nu(:,2)*p_r_dist %adjusting the probability for off-fault location


%loglog(nu(:,1), nu(:,2))
loglog(d_off_fault,d_rate)
xlabel('Displacement (m)')
ylabel('Annual Probability of Exceedence')
axis('tight');
set(gca,'FontSize',16,'FontWeight','bold')
grid on;
toc
```

```
function a_gamout = a_gam(xL)

a_gamout = 1.4244*xL + 1.856;

end

%this is the a term in the gamma distribution fit to D/MD data
```

```
function b_gamout = b_gam(xL)
```

```
b_gamout = -0.0832*xL +0.1994;

end

%this is the b term in the gamma distribution fit to the D/MD data
```

```
function muout = mu(mag)
a_MD = -2.5;
b_MD = 0.415;
sigma_mu = 0.148;
muout = log(10^(a_MD + b_MD*mag + sigma_mu));
end

%this is the a and b linear regression terms for P(MD|M,r)
%for all data in Mea22 the equation is  log10(MD)=0.40126*Mw-2.59939
%for FDHI data only in Mea22 it becomes log10(MD)=0.48150*Mw-2.9305

%for complete rupture in Mea22 it becomes log10(MD)=0.415*Mw-2.50
%for uncertainty it becomes log10(MD)=0.415*Mw-2.15+(#sigma*0.148)
```

```
function truncout = trlnrnd(mu, sigma, n)
%monte carlo sampling for a truncated lognormal distribution.  zmax is the
%maximum value where truncation occurs, here it is specified as MD = 15m.
%n random numbers between 0 and zmax are generated and thrown into the
%Inverted CDF for a truncated lognormal distribution, then pass them back.

z = unifrnd(0, 1, 1, n);

%truncout = exp(sqrt(2*sigma*sigma)*erfinv(2*z*(logncdf(log(15), mu, sigma)) - 1) + mu);

epsilon_max=5;

cdf_min=logncdf(exp(mu-epsilon_max*sigma),mu,sigma);

cdf_max=logncdf(exp(mu+epsilon_max*sigma),mu,sigma);

truncout=exp(sigma*sqrt(2)*erfinv(2*(z-0.5)*(cdf_max-cdf_min))+mu);

end
```